

Department of Physics and Astronomy

University of Heidelberg

Master thesis

in Physics

submitted by

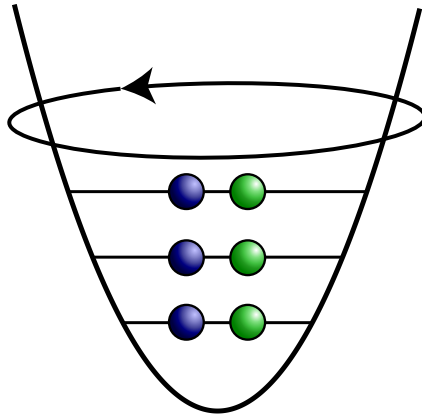
Lukas Palm

born in Frankfurt a. M.

2018



# Exploring fractional quantum hall physics using ultracold fermions in rotating traps



This Master thesis has been carried out by Lukas Palm

at the

Physikalisches Institut Heidelberg

under the supervision of

Prof. Dr. Selim Jochim



**Abstract:**

In this thesis, the possibilities of simulating fractional quantum hall (FQH) physics using an ultracold fermionic quantum gas experiment are explored. The correlated states responsible for the FQH effect are prime examples of topological phases of matter, providing both fascinating physics as well as opportunities for robust quantum devices. Ultracold atoms offer a unique advantage to study the microscopic properties of topological states. The main question of this thesis is how to experimentally realise and probe FQH states with fermions interacting via s-wave scattering. As previous experiments have shown, it is experimentally difficult to reach the strongly correlated regime required for FQH states. Therefore I examined an approach in the few-particle regime utilizing favourable properties of fermions in theoretical and experimental regard. I performed an exact diagonalisation study to identify an experimentally realistic parameter regime and accessible states. Additionally, I built and tested an optical setup for creating rotating optical microtraps. The optical potentials created by an interferometric method can be rotated at high speeds and controlled precisely. The central result of this thesis is that realisation of FQH physics using ultracold fermions is possible in the identified space of parameters, and that a number of interesting states are accessible. Single-particle spin-resolved imaging opens up a new window into correlations of FQH states and the microscopic properties of e.g. the Laughlin states.

**Zusammenfassung:**

In dieser Arbeit werden die Möglichkeiten untersucht, Zustände des fraktionalen Quanten-Hall Effektes (FQH) mit ultrakalten fermionischen Atomen zu erzeugen. Die stark korrelierten Zustände von Materie, welche diesen Effekt hervorrufen, sind grundlegende Beispiele für topologische Ordnung. Sie besitzen viele interessante physikalische Eigenschaften und sind Kandidaten für robuste Quantencomputer. Ultrakalte Atome bieten die einzigartige Möglichkeit, die mikroskopischen Eigenschaften topologischer Zustände zu untersuchen. Die zentrale Fragestellung dieser Arbeit ist daher, wie diese Zustände mittels ultrakalter Fermionen experimentell realisiert und beobachtet werden können. Wie frühere Experimente gezeigt haben, ist es schwierig, das notwendige Regime starker Korrelationen zu erreichen. Daher untersuche ich einen Ansatz im Bereich weniger Teilchen in theoretischer und experimenteller Hinsicht. In einer exakten Diagonalisierung wird ein realistischer Bereich von experimentellen Parametern sowie eine Reihe von möglichen Zuständen identifiziert. Außerdem wurde ein optisches System zur Erzeugung von rotierenden Mikrofallen aufgebaut und getestet. Durch die verwendete interferometrische Methode ist es möglich, optische Potentiale mit hohen Geschwindigkeiten und unter präziser Kontrolle zu rotieren. Die Ergebnisse dieser Arbeit zeigen, dass Zustände des FQH Effekt mit fermionischen kalten Atomen mit realistischen Parametern zugänglich sind. Dabei kann eine Abbildungsmethode, die einzelne Atome spinaufgelöst detektieren kann, neue Einsichten in die Korrelationen und mikroskopische Eigenschaften von FQH Zuständen wie z.B. dem Laughlin Zustand ermöglichen.



# Contents

<b>1</b>	<b>Introduction</b>	<b>9</b>
1.1	Outline . . . . .	12
<b>2</b>	<b>Theory of the quantum Hall effect</b>	<b>13</b>
2.1	The Integer Quantum Hall Effect . . . . .	13
2.2	The Fractional Quantum Hall Effect . . . . .	17
2.3	Anyons . . . . .	20
<b>3</b>	<b>Numerical study of a spinful fermion system</b>	<b>23</b>
3.1	Artificial gauge fields from rotating traps . . . . .	23
3.2	Review of the bosonic case . . . . .	29
3.2.1	Spectrum of states . . . . .	31
3.2.2	Observables . . . . .	34
3.3	Spinful ultracold fermion systems . . . . .	38
3.3.1	Exact diagonalisation results . . . . .	39
3.3.2	Methods of detection . . . . .	51
3.3.3	Correlation functions . . . . .	51
<b>4</b>	<b>Experimental Background</b>	<b>57</b>
4.1	Scattering properties . . . . .	57
4.2	Preparation of an ultracold Fermi Gas . . . . .	59
4.3	Single Particle Imaging Method . . . . .	62
4.4	2D Confinement . . . . .	63
<b>5</b>	<b>Experimental realization of a rotating optical trap</b>	<b>65</b>
5.1	Spatial Light Modulation . . . . .	66
5.1.1	Short revision of Fourier optics . . . . .	67
5.1.2	SLM characterization . . . . .	71
5.1.3	Analytic beam shaping . . . . .	73
5.1.4	Algorithm for arbitrary amplitude and phase . . . . .	75
5.2	Optical aberration correction . . . . .	78
5.3	Measurements . . . . .	85
5.3.1	Arbitrary light fields . . . . .	85
5.3.2	Single Beam Amplitude and Phase . . . . .	89
5.3.3	Two Beams . . . . .	91

5.4	Estimation of realistic experimental parameters . . . . .	98
<b>6</b>	<b>Conclusion</b>	<b>103</b>
6.1	Theory . . . . .	103
6.2	Experiment . . . . .	104
6.3	Outlook . . . . .	105
	<b>Appendices</b>	<b>113</b>
<b>A</b>	<b>Exact diagonalisation algorithm details</b>	<b>113</b>
<b>B</b>	<b>Extended figures</b>	<b>117</b>
B.1	Spectra for higher particle numbers . . . . .	117
B.2	Imbalanced spin components . . . . .	118
B.3	Energy Gap for higher particle numbers . . . . .	120
B.4	Density and two-body correlation functions . . . . .	121

# Chapter 1

## Introduction

When electrons are confined to two spatial dimensions and placed in a strong magnetic field at low temperatures, they produce a strongly correlated quantum liquid. This gives rise to a number of phenomena summarized as the quantum Hall effect (QHE). Originally, the QHE was discovered in semiconductor samples that were cooled to low temperatures and subjected to a strong perpendicular magnetic field. The Hall conductance  $\sigma$ , defined as the ratio of the driving current to the resulting hall voltage, was found to take quantized values, opposed to the classical effect. In the first discovery by Klaus von Klitzing, the Hall conductance showed only integer multiples of the so-called von Klitzing constant. This effect can be understood through the theory of Landau levels, the quantized orbitals of cyclotron motion of electrons in a perpendicular magnetic field. A few years later, additional plateaus of the Hall conductivity were observed [TSG82] at lower temperatures and higher magnetic fields, that did not correspond to integer, but fractional multiples of the quantization constant. This measurement is shown in Figure 1.1 and plateaus of the hall resistance  $R_H$  can be observed at specific magnetic fields strengths. The filling fraction  $\nu$  is directly related to the magnetic field as it is defined as  $\nu = p/q$  the ratio of the number of electrons ( $p$ ) to magnetic flux quanta  $q$ . A number of integer as well as fractional filling fractions could be observed in Figure 1.1. The existence of these fractional values requires a theory involving electron interactions, whereas the integer effect could be explained on a single particle level. This was first achieved by Robert Laughlin [Lau83], who described the fractional quantum Hall states as an incompressible electron liquid and received a Nobel price for this work together with the experimentalists Host Strömer and Daniel Tsui [TSG82] in 1998. However, Laughlins theory only applied to filling fractions  $\nu = 1/m$  (with  $m$  an odd integer) and was based on a specific trial wavefunction. Therefore, the discovery of the fractional quantum Hall effect stimulated a multitude of theoretical work to explain the microscopic origin of the different fractions. A great advanced was achieved through the theory of composite fermions [Jai89]. It's central idea is that electrons can capture magnetic flux quanta and the corresponding vortices in order to form quasi-particles minimizing their interaction energy. Consequently these composite fermions experience a reduced effective magnetic field. By this mechanism, a whole



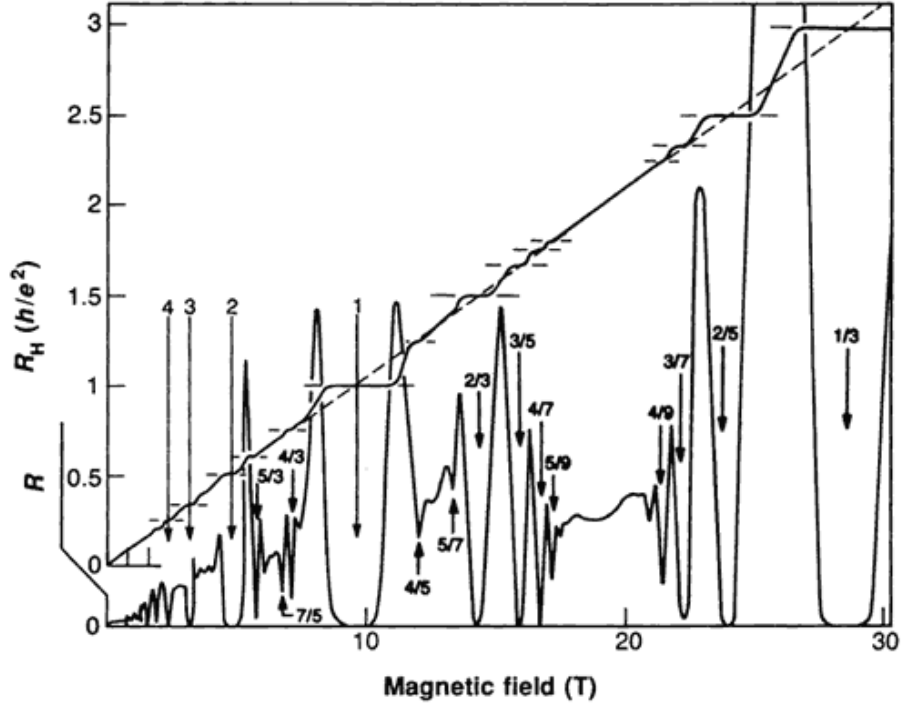


**Figure 1.1:** Original measurement of the fractional quantum hall effect by [TSG82]. Upper curve: the hall resistance  $R_H$  perpendicular to the driving current shows plateaus at certain magnetic fields that correspond to filling fractions  $\nu$  indicated by the arrows. Lower curve: the longitudinal resistance  $R$  vanishes at these fractions.

sequence of states with filling fractions

$$\nu = \frac{\nu^*}{2p\nu^* \pm 1} \quad (1.1)$$

in terms of the composite filling factor  $\nu^*$  could be explained. However, the exact mechanism of the experimentally observed  $\nu = 5/2$  state still remains an open question until today.

What makes the QHE so special is the precise quantisation of the Hall conductance into multiples of the fundamental constant  $e^2/h = 1/(25\,812.807\,572\,\Omega)$  (von Klitzing constant). This value is independent of any geometrical details of the sample or imperfections of the material, making it suited as a standard of resistance in metrology. The phases of matter present in the FQHE can only be described through non-local, so-called topological order. This is in contrast to the Landau theory of e.g. BCS superconductivity, where the different phases are classified via a local order parameter and their related symmetries. States described by topological order only depend on the global properties of the system and are therefore

---

insensitive to local disorder and defects. The energy gap above the ground-state of FQHE systems arises through strong correlations induced by the Coulomb interaction among electrons. In this case macroscopic properties like the Hall conductance can be related to a topological invariant called the Chern number. Also a number of excited states exist that contain quasi-particles and -holes displaying unusual properties such as fractional charge and exchange statistics. They are called anyons because they neither obey fermionic or bosonic properties.

A large number of experiments has been performed since the original discovery [TSG82] revealing an increasing variety of FQHE states. However, most experiments in semiconductor hetero-structures are limited to the study of bulk properties like conductance. Realising such states in a cold atoms experiment would open up access to the underlying microscopic properties through imaging or even manipulation at the single particle level. Previous attempts to performed such an experiment were made in the past by [Sch+04], [Zwi+05] and [GSC10]. In [Sch+04] a BEC of  $^{87}\text{Rb}$  atoms was stirred in a rotating magnetic trap to high rotational rates. Although this expected to be the proper procedure for creation of QH states, only an Abrikosov lattice of ordered vortices could be observed. This is due to the large number of atoms resulting in a filling fraction  $\nu \geq 500$  for which only the mean-field QH regime is accessible. Only at fillings  $\nu < 10$  the vortex lattice is expected to melt due to quantum fluctuations and transform into the quantum liquid of the FQHE. These low filling fractions were not accessible in the experiment because further reduction in atom number would have corrupted the imaging quality. A similar experiment was performed in [Zwi+05] where a quantum gas of  $^6\text{Li}$  was stirred using blue-detuned rotating beams. A similar lattice of vortices was observed both on the BEC and BCS side of the Feshbach resonance. Analogous to the previous experiment only a precursor of QH states could be observed because of the large atom number. The main challenge in such experiments is to reach the strongly correlated regime of low filling fractions. These fractions require transfer of a large amount of angular momentum exceeding the particle number into the sample, which is experimentally challenging especially for a large number of atoms. A different approach to FQH states employing ultracold atoms is therefore to work in the few-particle regime. There, the necessary small filling fractions can be already obtained at moderate total angular momenta. This route was pioneered in [GSC10] using ultracold bosons in an optical lattice with rotating sites. A mean number of atoms on the order of 10 enabled access to filling fractions  $\nu \leq 1$  required for FQHE states. However, verification of the prepared states was aggravated by a fluctuating atom number between lattice sites and an indirect observation through photo-association loss.

Here, I present a new approach to FQH states building on state-of-the-art experimental techniques for ultracold atoms. Our experiment using  $^6\text{Li}$  (see [Ser11]) constitutes a highly specialized platform for creating few-body states in the FQH regime: By utilising a single optical microtrap, a small atom number can be prepared deterministically at high speeds of rotation, yielding the desired filling fraction



$\nu \leq 1$ . With a recently developed single-particle imaging scheme [Ber+18], individual atoms can be detected in time of flight, enabling access to momentum correlation functions of deterministically prepared FQH states. Such an approach opens up a completely new view on FQHE physics. Instead of characterizing the system using bulk properties like conductivity, it will become possible to directly study the states microscopic properties. For example, a measurement of correlation functions as proposed in this thesis can confirm microscopically the picture of the Laughlin wavefunction. The real space image of a strongly correlated quantum fluid as drawn by Laughlin in his Nobel lecture [Lau] might thus become accessible.

In addition to providing new observables, FQH states using ultracold atoms also offer a new experimental scenario: Contrary to condensed matter systems, where the electron are spin-polarized because of the large Zeeman shift from the magnetic field, we can realize multi-component FQH systems through spinful ultracold atoms. This internal degree of freedom can lead to an increased number of interesting states. For example Skyrmions are predicted for both Bosons [LK90] and Fermions [Son+93].

## 1.1 Outline

In this thesis, I evaluated the possibilities to explore FQHE physics in a fermionic ultracold quantum gas experiment. For this purpose, I performed experimentally realistic regime of parameters must be identified. Because only little theoretical work on spinful fermions and none for the specific system at hand exists, a theoretical exact diagonalisation study was performed Chapter 3. In order to realise the states identified in the experiment, I planned and built an optical setup for creation of artificial gauge fields in Chapter 5.

First, the theory of Landau levels underlying all quantum Hall phenomena is revisited in Chapter 2. There, the necessary description in second quantisation is derived and the characteristic FQHE wavefunctions are presented. In Chapter 3 I present an exact diagonalisation performed using a numerical code developed during the course of this thesis. Initially, some known results for the case of bosons [PPC04],[Vie08] are reproduced in Section 3.2 to introduce the main concepts and serve as a benchmark for the numerical code. After that, new results for a two-component fermion system are presented in Section 3.3. A sequence of ground-states is identified and the corresponding necessary experimental parameters are computed. At last, signatures of these states in a detection through imaging are discussed Section 3.3.2.

As a second part, I present an experimental route to realisation of FQHE states. In Chapter 4 the existing experimental apparatus and techniques for preparation and imaging of a small ultracold atomic sample is briefly described. Subsequently, a rotating optical trap for the creation of artificial magnetic fields is set up in Chapter 5 and a number of required techniques is described. Finally, I asses parameters feasible for an experimental realisation in Section 5.4.

# Chapter 2

## Theory of the quantum Hall effect

On order to understand the fractional quantum hall effect, which arises through interactions between electrons, we first have to look at the single particle picture. The derivations in this chapter closely follow [Ton16].

### 2.1 The Integer Quantum Hall Effect

The Integer Quantum Hall Effect can be understood in terms of the electron motion in a two dimensional system subject to a strong magnetic field. Therefore we look at the Hamiltonian of a free particle in a vector potential

$$\mathcal{H} = \frac{1}{2m} (\mathbf{p} + e\mathbf{A})^2 = \frac{1}{2m} \pi^2 \quad (2.1)$$

with the kinetic momentum  $\pi = \mathbf{p} + e\mathbf{A}$ . The canonical commutation relations are

$$[x_i, p_j] = i\hbar\delta_{ij}, \quad [x_i, x_j] = 0 = [p_i, p_j] \quad (2.2)$$

It is important to note that two kinetic momenta do not commute:

$$[\pi_x, \pi_y] = -ie\hbar B \quad (2.3)$$

To solve the Hamiltonian Equation (2.1) we introduce ladder operators similar to the quantum harmonic oscillator by

$$a = \frac{1}{\sqrt{2e\hbar B}} (\pi_x - i\pi_y) \quad \text{and} \quad a^\dagger = \frac{1}{\sqrt{2e\hbar B}} (\pi_x + i\pi_y) \quad (2.4)$$

which obey the commutation relation  $[a, a^\dagger] = 1$ . If we write the Hamiltonian in terms of these operators, we obtain the same form as in the harmonic oscillator case:

$$\mathcal{H} = \frac{1}{2m} \pi^2 = \hbar\omega_B \left( a^\dagger a + \frac{1}{2} \right) \quad (2.5)$$

with the cyclotron frequency  $\omega_B$ . The Hilbert space of this Hamiltonian is a Fock space containing states  $|n\rangle$  with an energy of

$$E_n = \hbar\omega_B \left( n + \frac{1}{2} \right). \quad (2.6)$$



These energy levels are called Landau levels and will be of particular importance later. There are several possible choices for the vector potentials gauge describing the same magnetic field  $\mathbf{B} = \nabla \times \mathbf{A} = B\mathbf{e}_z$ . The symmetric gauge reflects rotational invariance

$$\mathbf{A} = (A_x, A_y) = \frac{B}{2}(-y, x), \quad (2.7)$$

while two other (called Landau gauge) preserve the translational invariance of the system

$$\mathbf{A} = B(-y, 0), \quad \mathbf{A} = B(0, x). \quad (2.8)$$

Even when the magnetic field  $\mathbf{B}$  is invariant under rotation and translation in the plane, the choice of  $\mathbf{A}$  is not. Choosing the symmetric gauge breaks translation invariance in the x- and y-direction, but it preserves the rotational symmetry and the angular momentum is a good quantum number.

To see the degeneracy of the Landau levels, we have to introduce a different momentum operator  $\tilde{\pi} = \mathbf{p} - e\mathbf{A}$  similar to the kinetic momentum, but with a minus sign. It fulfils the commutation relation

$$[\tilde{\pi}_x, \tilde{\pi}_y] = ie\hbar B \quad (2.9)$$

This momentum is not gauge invariant and depends on the specific gauge chosen, as we see from its commutators with the kinetic momentum:

$$[\pi_x, \tilde{\pi}_x] = 2ie\hbar \frac{\partial A_x}{\partial x}, \quad [\pi_y, \tilde{\pi}_y] = 2ie\hbar \frac{\partial A_y}{\partial y} \quad (2.10)$$

$$[\pi_x, \tilde{\pi}_y] = [\pi_y, \tilde{\pi}_x] = ie\hbar \left( \frac{\partial A_x}{\partial y} + \frac{\partial A_y}{\partial x} \right) \quad (2.11)$$

As we can see, all of these commutators only vanish if we choose the symmetric gauge. Then,  $\tilde{\pi}$  commutes with the Hamiltonian and we can diagonalize them simultaneously, resulting in a new quantum number. We will later identify this quantity as the angular momentum, supporting our previous argument on rotational symmetry. So far, the calculation of the energy spectrum was independent of a specific gauge. But for the reasons given above, we will continue the remaining calculations in the symmetric gauge, as this is also the natural choice for a rotating system. After fixing the gauge we have  $[\pi_i, \tilde{\pi}_j] = 0$  and can define two new ladder operators

$$b = \frac{1}{\sqrt{2e\hbar B}} (\tilde{\pi}_x + i\tilde{\pi}_y) \quad \text{and} \quad b^\dagger = \frac{1}{\sqrt{2e\hbar B}} (\tilde{\pi}_x - i\tilde{\pi}_y) \quad (2.12)$$

which also obey the canonical commutation relation  $[b, b^\dagger] = 1$ . The general Hilbert space is then constructed from the vacuum  $|0, 0\rangle$  as

$$|n, m\rangle = \frac{(a^\dagger)^n (b^\dagger)^m}{\sqrt{n!m!}} |0, 0\rangle \quad (2.13)$$

where  $n$  is a label for the Landau level and  $L = m - n$  denotes the total angular momentum. In the lowest Landau level (LLL),  $L$  and  $m$  coincide. The energy spectrum of this Hamiltonian and the different ladder operators actions are shown in Figure 2.1. To construct the real-space wave-functions, we express the creation

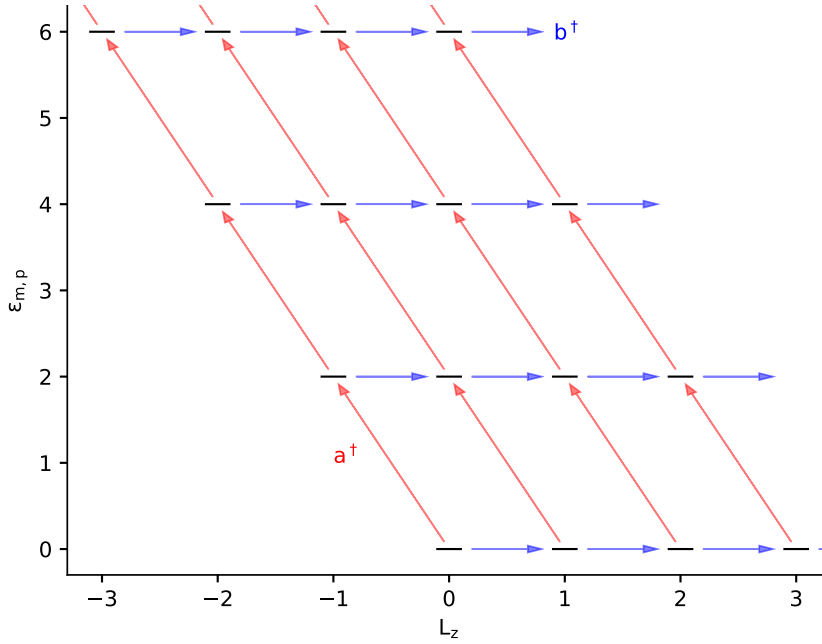


**Figure 2.1:** Landau levels (energy eigenstates of the Hamiltonian Equation (2.1)) as a function of angular momentum  $L_z$ . The arrows indicate the action of the creation operators  $a^\dagger$  (blue, increase Landau level) and  $b^\dagger$  (red, increase angular momentum).

and annihilation operators in terms of a complex coordinate  $z$ , because this fits the description of a plane.

$$a = \frac{1}{\sqrt{2e\hbar B}} (p_x - ip_y + e(A_x - iA_y)) \quad (2.14)$$

$$= \frac{1}{\sqrt{2e\hbar B}} \left( -i\hbar \left( \frac{\partial}{\partial x} - i \frac{\partial}{\partial y} \right) + \frac{eB}{2} (-y - ix) \right) \quad (2.15)$$

$$= -i\sqrt{2} \left( l_B \bar{\partial} + \frac{z}{4l_B} \right) \quad (2.16)$$

Where we introduced the complex coordinate and derivatives

$$z = x - iy \text{ and } \bar{z} = x + iy \quad (2.17)$$

$$\partial = \frac{\partial}{\partial z} = \frac{1}{2} \left( \frac{\partial}{\partial x} + i \frac{\partial}{\partial y} \right) \text{ and } \bar{\partial} = \frac{\partial}{\partial \bar{z}} = \frac{1}{2} \left( \frac{\partial}{\partial x} - i \frac{\partial}{\partial y} \right) \quad (2.18)$$



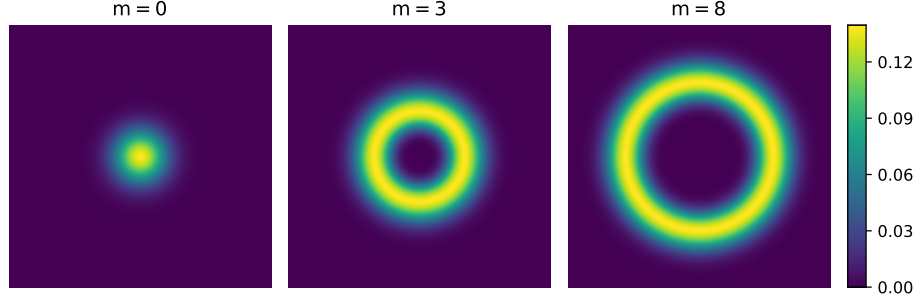


**Figure 2.2:** Spatial density  $n_m(x, y)$  of the lowest Landau level states  $\psi_{LLL,m}$  for different angular momenta  $m$ .

which fulfil  $\partial z = \bar{\partial} \bar{z} = 1$  and  $\partial \bar{z} = \bar{\partial} z = 0$  and where we introduced the magnetic length  $l_B = \sqrt{\frac{\hbar}{eB}}$  that sets the length scale of the state. To construct the *lowest Landau level* (LLL)  $n = 0$ , we make use of the property  $a |n = 0, m\rangle = 0$  and solve the resulting differential equation to obtain

$$\psi_{LLL}(z, \bar{z}) = f(z)e^{-|z|^2/4l_B^2} \quad (2.19)$$

where  $f$  is an arbitrary function. To fix this, we employ that the ground state of the LLL  $|0, m\rangle$  is also annihilated by  $b |0, m = 0\rangle = 0$  giving

$$\psi_{LLL,m=0}(z, \bar{z}) \propto e^{-|z|^2/4l_B^2} \quad (2.20)$$

up to normalization. The excited states in the LLL can then be obtained by acting with  $b^\dagger$ , yielding

$$\psi_{LLL,m}(z, \bar{z}) \propto \left(\frac{z}{l_B}\right)^m e^{-|z|^2/4l_B^2}. \quad (2.21)$$

The function  $f$  is then a monomial in  $z$ , making the state  $\psi_{LLL,m}$  an eigenstate of the angular momentum operator

$$L_z = i\hbar \left( x \frac{\partial}{\partial y} - y \frac{\partial}{\partial x} \right) = \hbar (z\partial - \bar{z}\bar{\partial}) \quad (2.22)$$

$$L_z \psi_{LLL,m} = \hbar m \psi_{LLL,m} \quad (2.23)$$

with eigenvalue  $\hbar m$ . The real-space density of these wave-functions, which is shown in Figure 2.2, looks like a ring around the origin with radius  $r = \sqrt{2ml_B^2}$  for an angular momentum  $m$ . In the same way, one could also construct the wave-functions of higher Landau levels by acting with  $a^\dagger$ , but the subsequent discussion will only focus on the LLL. As we can see from Equation (2.6) and also Figure 2.1, the energy of a state only depends on the Landau level index  $n$ , but not  $m$ . This means that

the ground state (and every Landau level) is highly degenerate. We can estimate the number of states  $\mathcal{N}$  in a disk shaped region of area  $A = \pi R^2$  as

$$\mathcal{N} = \frac{R^2}{2l_B^2} = \frac{A}{2\pi l_B^2} = \frac{eBA}{2\pi\hbar} = \frac{BA}{\Phi_0}, \text{ with } \Phi_0 = \frac{2\pi\hbar}{e}, \quad (2.24)$$

where  $\Phi_0$  is the flux quantum. In the presence of an electric field from a voltage applied to the sample, the Hall conductivity can be calculated [Ton16] as

$$\rho_{xy} = \frac{2\pi\hbar}{e^2} \frac{1}{\nu}, \quad B = \frac{n}{\nu} \Phi_0 \quad (2.25)$$

where  $B$  is the magnetic field at which plateaus of  $\rho_{xy}$  occur and  $n$  denotes the electron density. In semiconductor systems, a number of additional effects come into play. The finite size of the sample gives rise to chiral edge modes, whose direction of motion is fixed for each edge. Furthermore, no reason was given so far on why the plateaus in conductivity (see Figure 1.1) extend around the exact magnetic fields given in Equation (2.25). This effect is a result of disorder caused by impurities in the sample, that give rise to localised states. Both of these effects are not significant for a cold atoms system, which is why they are not described in detail here.

## 2.2 The Fractional Quantum Hall Effect

Like the integer quantum hall effect, the fractional effect was also discovered in an experiment and was not predicted by any theory. Its signature are the additional plateaus observable in the Hall resistance in Figure 1.1 at fractional values of the filling fraction  $\nu$ . There are several series of this fraction such as  $\frac{1}{3}, \frac{2}{5}, \frac{3}{7}, \dots$  and  $\frac{2}{3}, \frac{3}{5}, \frac{4}{7}, \dots$  where the denominator is usually an odd number, with the two exceptions  $\frac{5}{2}$  and  $\frac{7}{2}$ . The filling fraction  $\nu = \frac{N}{\mathcal{N}}$  is defined as the ratio between the number of electrons  $N$  and available states in the Landau level  $\mathcal{N}$ . If we only partially fill one Landau level with  $N = \nu\mathcal{N}$  electrons, there are  $\binom{\mathcal{N}}{\nu\mathcal{N}}$  possibilities to populate the ground state. This is a very large number, and therefore the ground state is highly degenerate. However, the electrons experience a Coulomb interaction

$$V_{Coulomb} = \frac{e^2}{4\pi\epsilon_0|\mathbf{r}_i - \mathbf{r}_j|} \quad (2.26)$$

that should lift this degeneracy. Computing the ground state including the interaction is unfortunately not feasible analytically, and also a numerical solution is only tractable for a small number of particles (as we will see in Chapter 3). This is why Laughlin resorted to an educated guess of the ground state wave function considering the following three arguments: The guess has the form of a Jastrow product

$$\Psi(z_1, \dots, z_N) = \prod_{i < j}^N f(z_i - z_j) \exp\left\{-\frac{1}{4} \sum_{l=1}^N |z_l|^2\right\}. \quad (2.27)$$



To minimize this trial function with respect to the Hamiltonian, additional constraints are considered: The many-body wave function can only be assembled from single-body wave functions from the lowest Landau level if consider a state with  $\nu < 1$ . This implies that  $f$  must be a polynomial in  $z$ . According to the Pauli exclusion principle, the full wave-function must be antisymmetric, therefore  $f(z)$  must be odd. Because the state is rotationally symmetric, the angular momentum must be conserved. This requires  $\prod_{i<j} f(z_i - z_j)$  to be a homogeneous polynomial of degree  $M$ , which is the total angular momentum. All constraints are only fulfilled if  $f$  has the form  $f(z) = z^m$  with  $m$  an odd integer. The resulting wave function is the celebrated Laughlin state for filling fractions  $\nu = 1/m$ .

$$\Psi(z_1, \dots, z_N) = \prod_{i<j}^N (z_i - z_j)^m \exp \left\{ -\frac{1}{4} \sum_{l=1}^N |z_l|^2 \right\}. \quad (2.28)$$

This wavefunction contains two competing terms. The exponential factor locates the particles close to centre of the system, while the product introduces a number of zeros into the wavefunction. When two electrons come together, the term  $z_i - z_j$  vanishes as the electrons interact repulsively. In the following we will omit the exponential factor for ease of notation, as it never changes.

To see that this state has the right filling fraction, we only look at terms in the product contacting the coordinate of a specific particle, say  $z_1$ :

$$\prod_{i<j}^N (z_i - z_j)^m \propto \prod_{j>1}^N (z_1 - z_j)^m \quad (2.29)$$

As there are  $N - 1$  of these terms, the highest power of  $z_1$  is  $m(N - 1)$ , which corresponds to the highest angular momentum for this particle. The state is therefore located on a radius of  $R \approx \sqrt{2mN}l_B$  as we saw in Figure 2.2, and the full wave function occupies an area of  $A \approx 2\pi mNl_B^2$ . Correspondingly, the number of states can be calculated according to Equation (2.24) as  $\mathcal{N} = A/2\pi l_B^2 \approx mN$  yielding the desired filling fraction of  $\nu = 1/m$ . To check the validity of the Laughlin wavefunction, we look at the wavefunction for  $m = 1$  that should coincide with a filled Landau level from the non-interacting theory of the integer effect. To construct a many-body wavefunction of  $N$  electrons, we write down the Slater determinant

$$\psi(x_i) = \begin{vmatrix} \psi_1(x_1) & \psi_1(x_2) & \dots & \psi_1(x_N) \\ \psi_2(x_1) & \psi_2(x_2) & \dots & \psi_2(x_N) \\ \vdots & & & \vdots \\ \psi_N(x_1) & \psi_N(x_2) & \dots & \psi_N(x_N) \end{vmatrix}, \quad (2.30)$$

which is antisymmetric over all particles to fulfil the fermionic exchange statistic. For the single particle wavefunctions  $\psi_i(x_j)$  we insert the lowest Landau level states

$\psi_m(z) \propto z^m$  obtained in Equation (2.21). The resulting Slater determinant yields a state of the form

$$\psi(x_i) = \begin{vmatrix} z_1^0 & z_2^0 & \dots & z_N^0 \\ z_1^1 & z_2^1 & \dots & z_N^1 \\ \vdots & \vdots & \ddots & \vdots \\ z_1^{N-1} & z_2^{N-1} & \dots & z_N^{N-1} \end{vmatrix} = \prod_{i < j}^N (z_i - z_j) \quad (2.31)$$

that indeed coincides with the Laughlin wavefunction for  $m = 1$ . This form is called a *Vandermonde* determinant and it will be of importance later on as a minimal wavefunction ensuring fermionic statistic.

Despite being a trial wave function, Laughlins wavefunction shows very good overlap with the exact ones obtained by numerical diagonalisation. As computing the ground state is difficult numerically, this could only be verified for a small number of particles. Although it may not be the exact ground state for the Coulomb interaction, one can construct a Hamiltonian whose ground state is given by the Laughlin wavefunction. This can be done in terms of the *Haldane pseudo-potentials*  $v_m$  given by

$$v_m = \frac{\langle M, m | V | M, m \rangle}{\langle M, m | M, m \rangle}. \quad (2.32)$$

These specify the strength of interaction for a certain value of relative angular momentum  $m$  of two particles. In the Coulomb interaction, many of these potentials contribute as the interactions has long range. However, as we are focussing our discussion on cold atom systems later on, where only s-wave interactions (ie.  $m = 0$ ) play a role. Therefore the pseudo potentials are not discussed in detail here. Instead we want to take a look at the excitations of the  $\nu = 1/m$  groundstate, as these posses are number of interesting properties.

We can excite a quasi-hole at position  $\eta$  in the system by writing

$$\psi_{hole}(z_i; \eta) = \prod_{i=1}^N (z_i - \eta) \prod_{j < k}^N (z_j - z_k)^m \quad (2.33)$$

By introducing a factor  $(z_i - \eta)$ , the electronic density vanishes at the position  $\eta$  describing a hole in the fluid. This quasi-hole has a very surprising property, it carries a charge  $e^* = e/m$  that is a fraction of the underlying electron charge  $-e$ . To see this, we can make a simple hand-waving argument first. We can introduce  $m$  quasi-holes at the same position  $\eta$  by writing

$$\psi_{mholes}(z_i; \eta) = \prod_{i=1}^N (z_i - \eta)^m \prod_{j < k}^N (z_j - z_k)^m. \quad (2.34)$$

The wavefunction then looks like the one we would obtain with an additional electron  $z_{N+1} \propto \eta$  at the holes position. However  $\eta$  is not a variable of the system, but an



external parameter describing one missing electron. Therefore  $m$  holes behave like one deficit electron, so one hole acts like a  $m$ -th of one electron with charge  $e/m$ . When there are quasi-holes, there also should be quasi-particles, however it is not immediately clear how to write them down. By introducing a quasi-hole into the wavefunction, the power of  $z_i$  and thereby the angular momentum is increased. To have a quasi-particle, the electron density should be increased, wherefore the angular momentum has to be decreased. However we cannot simply divide the wavefunction by  $(z_i - \eta)$ , as this would lead to singularities. But because the Laughlin wavefunction is a polynomial in  $z_i$ , the derivative with respect to  $z_i$  decreases the power of  $z_i$  by one and therefore reduce the angular momentum.

$$\psi_{particle}(z_i; \eta) = \prod_{i=1}^N \left( 2 \frac{\partial}{\partial z_i} - \bar{\eta} \right) \prod_{j < k}^N (z_j - z_k)^m \quad (2.35)$$

## 2.3 Anyons

Since the discovery of topological states in the context of quantum Hall physics, a lot of interest in these novel phases of matter and additional ones e.g. topological insulators [HK10] has developed. Beyond that certain excitations of FQH states can



**Figure 2.3:** Worldlines from anti-clockwise and clockwise braiding of two particles cannot be smoothly connected.

posses excitations with particular properties. When we write down the wavefunction for two identical particles  $\psi(x_1, x_2)$ , the probability  $|\psi(x_1, x_2)|^2 = |\psi(x_2, x_1)|^2$  must be unchanged if we exchange them. Therefore the wavefunction can only differ by a phase

$$\psi(x_1, x_2) = e^{i\pi\alpha} \psi(x_2, x_1) \quad (2.36)$$

After exchanging the particles a second time, we have returned to the original configuration.

$$\psi(x_1, x_2) = e^{i2\pi\alpha} \psi(x_1, x_2) \quad \Rightarrow \quad e^{i2\pi\alpha} = 1 \quad (2.37)$$

This condition leads us to the familiar two kinds of particles, bosons ( $\alpha = 0$ ) and fermions ( $\alpha = 1$ ). However, this argument is only valid in three spatial dimensions. There, the particles worldlines can always be smoothly deformed to the case where the particles were not moved at all. This led to the condition  $e^{i2\pi\alpha} = 1$  because the

state before and after the rotation is the same. Though in two spatial dimensions, this is no longer true. The worldlines tangle up and it is not possible to untangle them without cutting one of the lines. This indicates that the direction of winding, as shown in Section 2.3, results in a different topology of the worldlines. This means that after two rotations, the particles may have a memory of the path in space-time resulting in an arbitrary phase  $\alpha$ . That gives rise to *anyon* statistics, where particles can have  $\alpha \neq \{0, 1\}$  and also the direction of exchange matters. When multiple particles are being braided, a further distinction into Abelian and non-Abelian anyons has to be made, where this name is relating to the underlying group structure. Non-Abelian anyons are of special interest because they can provide a platform for topological quantum computing as discovered in [KL09].





# Chapter 3

## Numerical study of a spinful fermion system

A large body of theoretical work on quantum Hall physics exists, both in terms of analytical and CFT calculations (see [Han+16] for a review) as well as numerical studies [MDD02], [RJ04]. However, these mostly focus on the spin-polarized case. Therefore new calculations have to be performed to examine a system of ultracold spinful fermions, where s-wave scattering limits interactions to occur between the different components. To be as close to an actual experiment as possible, all calculations are performed in the disk geometry. This is contrary to a lot of the literature, where a spherical geometry first introduced in [Hal83a] with a magnetic monopole at the centre is assumed. An exact diagonalisation of the system mentioned is accessible because only small atom numbers are considered. It is also helpful to have such a code at hand as an experimentalist in order to assess different parameters or effects of imperfections. The theoretical framework for a numerical calculation is therefore derived in the following.

Before starting the derivation for rotating traps, it is worth noting that a variety of different methods for creating artificial gauge fields exist. An overview is presented in [GBZ16] and in the following some of them are briefly described for comparison.

### 3.1 Artificial gauge fields from rotating traps

Because ultracold atoms are neutral, they do not experience a Lorentz force in a magnetic field that is required for the formation of Landau levels. Therefore one has to resort to an artificial or synthetic magnetic field that mimics the force on a charged particle. There exist multiple strategies to engineer such an artificial gauge field, a few of which will be discussed in the following.

**Laser imprinted phase** When an atom, trapped in an optical lattice, hops around a closed path in the lattice, external lasers can generate a phase change that is reminiscent of the flux of a magnetic field [ZBN16].



**Floquet engineering** In [Flä+16], the authors employ a hexagonal optical lattice which is shaken circularly. This leads to dressed energy bands described in terms of Floquet theory. The lattice acceleration breaks time-reversal symmetry and leads to complex hopping amplitudes between sites. The authors obtain a measurement of the band topology in terms of the Berry curvature and the Chern number, which is a topological invariant.

**Superlattice** The authors of [Loh+18] present an experimental realisation of the 4D integer Quantum Hall Effect. In previous work [Loh+16] the authors already demonstrated the 2D case by utilizing a topological charge pump [Tho83]. For this, the relative phase of an optical superlattice is modulated in time giving rise to an artificial dimension in terms of Fourier components of the drive. This dynamical version of the QHE allows them to study transport properties of the system like quantisation of the bulk response to integer values.

Both of these examples are beautiful demonstrations of realising topological states, however all this is done in terms of band structure, so only in the single particle regime without interactions. When interactions among the particles are included, this could open up new richness of highly correlated states like the FQHE Laughlin wavefunction.

## Single particle picture

An atom trapped in a rotating harmonic potential is formally equivalent to an electron in two dimensions placed in a magnetic field for high frequencies of rotation. To see this, we look at the Hamiltonian of an axially symmetric harmonic trap rotating around the  $z$  axis containing  $N$  ultracold atoms. We assume the trap frequency in  $z$  direction  $\omega_z$  to be sufficiently high, such that any excitations along  $z$  are frozen out ( $\mu, T \ll \omega_z$ ). Then the gas is confined to quasi 2D. In the rotating frame  $\mathbf{\Omega} = \Omega \mathbf{e}_z$  the Hamiltonian neglecting interactions reads

$$\mathcal{H} = \sum_{i=1}^N \left[ \frac{\mathbf{p}_i^2}{2m} + \frac{1}{2} m \omega^2 \mathbf{r}_i^2 - \Omega L_{z,i} \right] \quad (3.1)$$

with  $\omega$  the trap frequency in the x-y plane ( $\omega \ll \omega_z$ ),  $\Omega$  the speed of rotation and  $L_{z,i}$  denotes the angular momentum of particle  $i$  along  $z$ . This Hamiltonian can be rewritten into a canonical form

$$\mathcal{H} = \sum_{i=1}^N \left[ \frac{1}{2m} (\mathbf{p}_i - m\omega \mathbf{e}_z \times \mathbf{r}_i)^2 + (\omega - \Omega) L_{z,i} \right] \quad (3.2)$$

or equivalently

$$\mathcal{H} = \sum_{i=1}^N \left[ \frac{1}{2m} (\mathbf{p}_i - m\mathbf{\Omega} \times \mathbf{r}_i)^2 + \frac{1}{2} m (\omega^2 - \Omega^2) \mathbf{r}_i^2 \right] \quad (3.3)$$

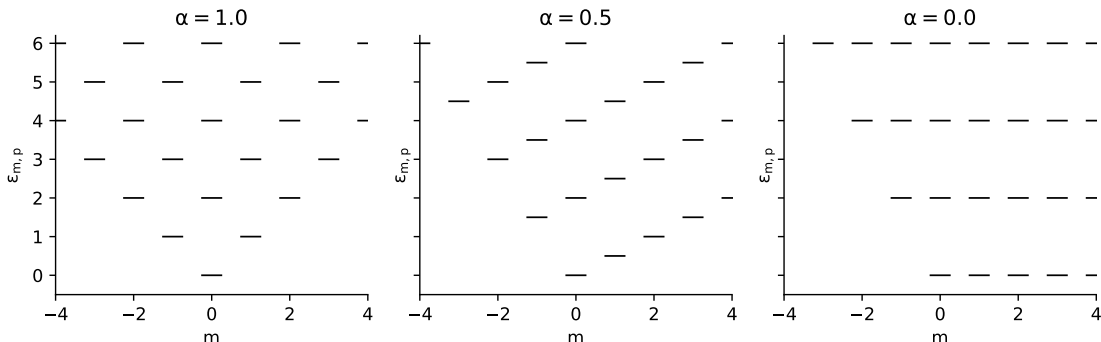


**Figure 3.1:** Landau level structure for different speeds of rotation  $\alpha = (1 - \Omega/\omega)$ . The left panel  $\alpha = 1$  corresponds to no rotation while for the right panel  $\alpha = 0$  frequency of rotation matches the trap frequency.

We can compare the first term of  $\mathcal{H}$  with the usual form of the Landau Hamiltonian Equation (2.1)  $(\mathbf{p} + e\mathbf{A})^2$  and interpret the rotation as vector potential  $\mathbf{A} = m\Omega \times \mathbf{r}$ . It therefore appears like a magnetic field  $\mathbf{B} = \nabla \times \mathbf{A} = 2m\Omega \mathbf{e}_z$  along the z-axis. As we can see, in the de-confinement limit  $\Omega \rightarrow \omega$ , the Hamiltonian is the one of free particles in a homogeneous magnetic field. In the following we work in non-dimensional units by expressing all energy scales in units of  $\hbar\omega$  and lengths in units of the harmonic oscillator length  $\sqrt{\hbar/m\omega}$ . In a second quantized form, this Hamiltonian can be rewritten analogous to the derivation in Section 2.1 as

$$\mathcal{H} = (2a^\dagger a + 1) + \alpha (b^\dagger b - a^\dagger a), \quad \alpha = \left(1 - \frac{\Omega}{\omega}\right) \quad (3.4)$$

in terms of creation and inhalation operators  $a, b$  and the confinement strength  $\alpha$ . When the trap is not rotating, we have  $\alpha = 1$  and for  $\alpha \rightarrow 0$  we approach the de confinement limit  $\Omega = \omega$  where the trapping potential is cancelled by the centrifugal force. The states of this systems  $|n_a, n_b\rangle$  are described by two occupation numbers  $n_a, n_b$  of the modes. Their level structure can be seen in Section 3.1 for different values of the confinement strength  $\alpha$ . Without rotation ( $\alpha = 1.0$ ), the levels resemble the shape of an inverted tree. When we start rotating the system the levels tilt to the right until the former diagonals form flat bands of levels. In this limit  $\alpha \rightarrow 0$  it is beneficial to define a new quantum number  $l = n_b - n_a$  that represents the angular momentum of the state and their energy is given by  $\epsilon_{n_a, l} = 2n_a + \alpha l$ . In the case  $\alpha = 0$ , the quantum number  $n_a$  labels the different Landau levels that are separated by an energy gap of 2. Inside these manifolds the energy does not depend on  $l$  and they are highly degenerate. When dealing with filling fractions  $\nu < 1$  only the lowest Landau level (LLL)  $n_a = 0$  is occupied. Therefore usually all calculations are cut down to the LLL subspace to reduce the size of the Hilbert space. In this



way we end up with the same Hamiltonian as in Section 2.1 with the eigenstates  $\psi_m \propto z^m e^{-|z|^2/4l_B}$ .

## Interactions

So far, this discussion was restricted to the single-particle physics, but to deal with the many-body problem, interactions between the atoms must be taken into account. For ultracold atoms, this interaction is usually restricted to s-wave scattering (see Section 4.1 for more details). The phase shift of the scattered wavefunction can be modelled by a contact interaction represented by a delta potential

$$\mathcal{H}_{int} = \eta \sum_{i < j} \delta^{(2)}(z_i - z_j) \quad (3.5)$$

where the interaction strength  $\eta = \sqrt{8\pi}a_s/l_z$  can be expressed through the 3D s-wave scattering length  $a_s$  and the harmonic oscillator length  $l_z = \sqrt{\hbar/m\omega_z}$  in z-direction. This parameter is particularly important, because the two competing energy scales of interaction and confinement determine the required speed of rotation to reach the Laughlin state. In a ultracold atoms experiment, the scattering length can be tuned via a Feshbach resonance and the axial trapping frequency  $\omega_z$  can be set via the optical potential in this direction. Therefore  $\eta$  can be tuned over a wide range, but it is constrained by some conditions discussed later on.

## Many-body description

To perform exact diagonalisation for a system of few bosonic or fermionic atoms, we first have to choose a computational basis. As the quantum number for the single particle wavefunction is given by the angular momentum  $m$ , we use an occupation number basis for the different angular momentum modes. This is also called Fock-Darwin basis and can be written as

$$|n_0, n_1, n_2, \dots\rangle = |n_{m=0}\rangle \otimes |n_{m=1}\rangle \otimes |n_{m=2}\rangle \otimes \dots = \quad (3.6)$$

$$|n_{m=0}, n_{m=1}, n_{m=2}, \dots\rangle = \sum_m \left(a_m^\dagger\right)^{n_m} |vac\rangle \quad (3.7)$$

with  $a_m \in \{b_m, c_m\}$  for bosons or spin polarized fermions. The corresponding Hilbert space is a product of Fock spaces for each angular momentum mode  $m$ . It is infinite-dimensional, because some particle could occupy an arbitrary high orbital  $m$ . To make the dimensionality tractable for numerical computations, a cut-off is introduced in two ways. The local dimension of the Fock space for one mode is restricted to particle numbers  $n_i < N$  for bosons, and for fermions the dimension naturally is 2 because of the Pauli exclusion principle (for one spin component). In addition, the number of angular momentum modes is limited to  $m < M$  orbitals by choosing

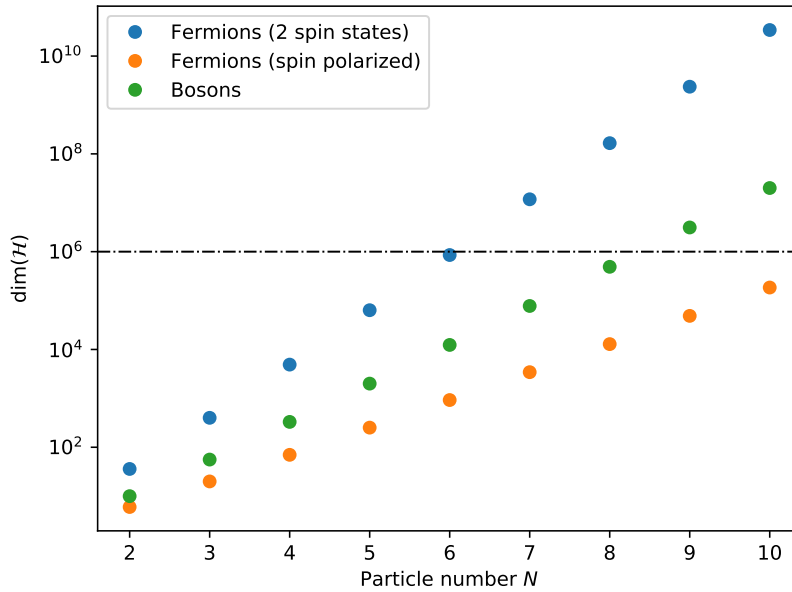


**Figure 3.2:** Size of the Hilbert space  $\dim(\mathcal{H})$  for bosons, spin polarized fermions and spinful fermions as a function of particle number  $N$  for an angular momentum cut-off  $M = 2N$ .

an appropriate cut-off  $M$ . In this way the otherwise infinite dimension of the single particle Hilbertspace is restricted. When the cut-off is chosen right, this doesn't influence the low energy states like the Laughlin state and its excitations, as orbitals with higher  $m$  are only occupied to a negligible amount. For spinful fermions, an additional spin degree of freedom has to be incorporated

$$|n_0, n_1, n_2, \dots\rangle_{\uparrow} \otimes |n_0, n_1, n_2, \dots\rangle_{\downarrow} = \sum_{m,\sigma} (c_{m,\sigma}^{\dagger})^{n_{m,\sigma}} |vac\rangle \quad (3.8)$$

The resulting dimensionality of the Hilbert space can be calculated (see Chapter A) for fermions as  $\dim(\mathcal{H}) = \binom{M}{N}$  and  $\dim(\mathcal{H}) = \binom{M}{N}^2$  for spinful fermions respectively. In the case of bosons one must take care of the indistinguishability of multiple occupations giving  $\dim(\mathcal{H}) = \binom{M+N-1}{N}$ . The resulting size of the Hilbert space, that corresponds to the number of basis states, is depicted in Figure 3.2. As expected, the size grows exponentially with particle number wherefore only few particles can be considered for an exact diagonalisation.

The many-body Hamiltonian Equation (3.1) including the interaction Equation (3.5) can be expressed in second quantisation as

$$\mathcal{H} = \mathcal{H}_0 + \mathcal{H}_{int} = \sum_{m,\sigma} \alpha(m+1) a_{m,\sigma}^{\dagger} a_{m,\sigma} + \sum_{\sigma,\sigma'} \sum_{\{m\}} V_{\{m\}}^{(\sigma,\sigma')} a_{m_1,\sigma}^{\dagger} a_{m_2,\sigma'}^{\dagger} a_{m_3,\sigma'} a_{m_4,\sigma} \quad (3.9)$$



with  $a_m \in \{b_m, c_m\}$  respectively. The first term  $\mathcal{H}_0$ , representing the confinement, coincides with the systems total angular momentum operator  $L = \sum_j L_{z,j} = \mathcal{H}_0$ . For bosons, only one spin component is considered and the index  $\sigma$  can be dropped. The interaction matrix element  $V_{\{m\}}^{(\sigma,\sigma')}$  can be computed from the single particle wavefunctions

$$V_{\{m\}}^{(\sigma,\sigma')} = \langle m_{1,\sigma}, m_{2,\sigma'} | \mathcal{H}_{int} | m_{3,\sigma'} m_{4,\sigma} \rangle \quad (3.10)$$

$$= \frac{\eta}{2} \int dz \psi_{m_1}^*(z) \psi_{m_2}^*(z) \psi_{m_3}(z) \psi_{m_4}(z) \quad (3.11)$$

$$= \frac{\eta}{8\pi l_B} \frac{(m_1 + m_2)! \delta_{m_1+m_2-m_3-m_4}}{2^{m_1+m_2} \sqrt{m_1! m_2! m_3! m_4!}} \quad (3.12)$$

The delta function in Equation (3.12) ensures that the conservation of angular momentum  $L_z$ , as the sum of incoming angular momenta equals the outgoing one. In terms of the many-body state in the Fock-Darwin basis  $|n_0, n_1, n_2, \dots, n_M\rangle$ , this interaction can be visualized in the following way:

$$V_{\{4,4,2,6\}}^{(\sigma,\sigma')} = \left| \begin{array}{c} \text{---} \bullet \text{---} \bullet \text{---} \bullet \text{---} \text{---} \\ \quad \quad \quad \curvearrowright \quad \quad \quad \curvearrowleft \\ \quad \quad \quad \bullet \bullet \quad \quad \quad \bullet \end{array} \right\rangle + h.c. \quad (3.13)$$

Grey dots denote all angular momentum orbitals occupied by a number of bosons (blue balls). Of course the reversed process contributes equally to the interaction. It is also worth noting that the interaction does not depend on the particles spin, as both components experience the same magnetic field strength  $B = 2m\Omega$ . This is due to its artificial nature and different from a real magnetic field, where the spin components could experience a Zeeman shift because of the different magnetic momenta. Such a shift could be still included into the calculations as

$$\mathcal{H}_{Zeeman} = \frac{\beta}{2} \sum_{\sigma \in \{-,+\}} \sum_m \sigma(m+1) a_{m,\sigma}^\dagger a_{m,\sigma}. \quad (3.14)$$

Because the trap is rotationally symmetric about the z-axis, no angular momentum is transferred to the atomic cloud when rotating the trap. To achieve this, a small perturbation must be introduced into the optical potential that rotates in the laboratory frame. In its most general form, such a stirring potential has the form

$$\mathcal{H}_p = \epsilon \left( z^m e^{im\Omega t} + (z^*)^m e^{-im\Omega t} \right). \quad (3.15)$$

Physically, this term corresponds to a rotating trap isotropy that enables transfer of angular momentum into the atomic sample. In the rotating frame with frequency  $\Omega$  it can be expressed in second quantized form

$$\mathcal{H}_p = \epsilon \left( \sum_l v_{l,m} a_{l+m}^\dagger a_l + h.c. \right) \quad \text{with} \quad v_{l,m} = 2^{-m/2} \frac{(l+m)!}{\sqrt{l!(l+m)!}}. \quad (3.16)$$

In the simplest case  $m = 2$  this corresponds to a quadrupole deformation  $\mathcal{H}_p \propto x^2 - y^2$  of the trap. In this case the Hamiltonian reads

$$\mathcal{H}_p = \epsilon \left( \sum_l \sqrt{(l+2)(l+1)} a_{l+2}^\dagger a_l + h.c. \right) \quad (3.17)$$

and only angular momentum orbitals with a difference of two are coupled.



Higher order perturbations are also possible to either couple angular momentum states with an odd difference or accelerate the transfer into high angular momentum states.

## 3.2 Review of the bosonic case

There is a large variety of proposals and studies on simulating fractional quantum Hall physics using ultracold bosons [PPC04],[Vie08],[Fet09],[GSC10]. This section reviews some key findings from the bosonic case and draws from the text [PPC04]. Additionally, the bosonic case also serves as a benchmark for the numerical algorithms developed for this thesis (see Appendix Chapter A). In order to derive the many-particle energy spectrum, the Hamiltonian Equation (3.9) is diagonalized for a for a number of different values of the rotational frequency  $\Omega$ , interaction strength  $\eta$  and perturbation strength  $\epsilon$ . The qualitative influence of the corresponding Hamiltonian terms is shown in Figure 3.3. When only including the kinetic term is included (left panel), the energy of the states only depends on the rotational frequency  $\alpha$  relative to the trapping frequency. The eigenstates in this case are the Landau levels from the integer (non-interacting) quantum hall effect. This is exactly the same behaviour one can observe in Section 3.1 where the lowest Landau level gets tilted with decreasing  $\alpha$  until all levels become degenerate for  $\alpha \rightarrow 0$ . When interactions between the particles are included (central panel) in Section 3.1, the picture changes substantially. Crossings among the energy levels emerge, and the ground state undergoes a sequence of states for increasing speed of rotation. These states possess a higher angular momentum  $L$  in order to minimize the interaction energy among particles occupying the same angular momentum orbitals. As the crossings between the different states are not avoided, the system would simply stay in the trivial Gaussian ground state  $L = 0$  when increasing the frequency of rotation  $\Omega$ . This is due to the rotational symmetry of the system, conserving the angular momentum  $L$ . So in order to reach higher angular momentum states adiabatically, this symmetry has to be broken by a perturbation like the quadrupole trap deformation Equation (3.17). As it is shown in Section 3.1 (right panel), this deformation leads to avoided crossings. The resulting energy gap of to the first excited state enables preparation of



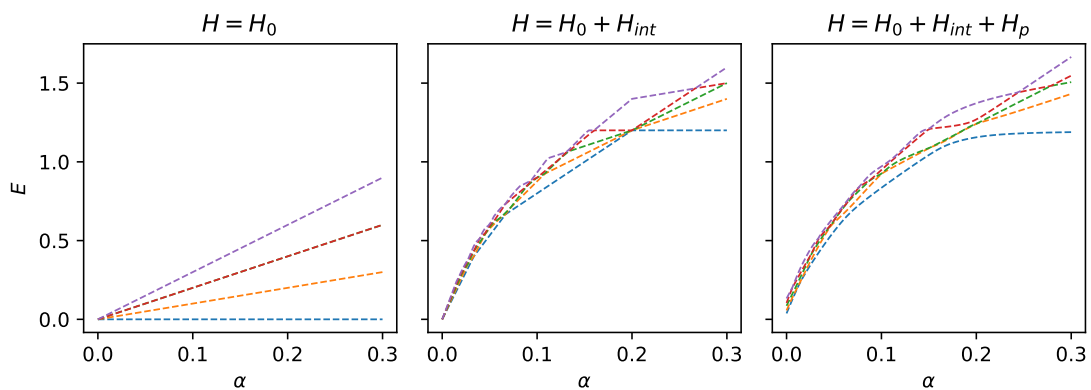


**Figure 3.3:** Eigenenergies of the model Hamiltonian Equation (3.9) as a function of rotation speed  $\alpha$ , including different contributing terms. In (a) only the kinetic term is included, leading to a linear dependence of the states (Landau levels) on the rate of rotation. When repulsive interactions between the particles are included (b), crossings among the levels emerge as non-trivial groundstates can lower the interaction energy. These crossings start to get avoided when we include (c) an anharmonic perturbation Equation (3.17) into the Hamiltonian. Only the lowest energies are shown for clarity and the parameters are set to  $N = 4$ ,  $\eta = 0.1$  and  $\epsilon = 0.02$ .

higher angular momentum states if the rate of rotation is increased slow enough to remain adiabatically. Each crossing of the ground state energy indicates a transition into a new distinct phase.

### 3.2.1 Spectrum of states

The different ground states of the Hamiltonian form a sequence with angular momentum  $L$  increasing by  $N$  in each step. This sequence is depicted in Figure 3.4 along with the low energy spectrum of a system of  $N = 4$  bosons. Another way

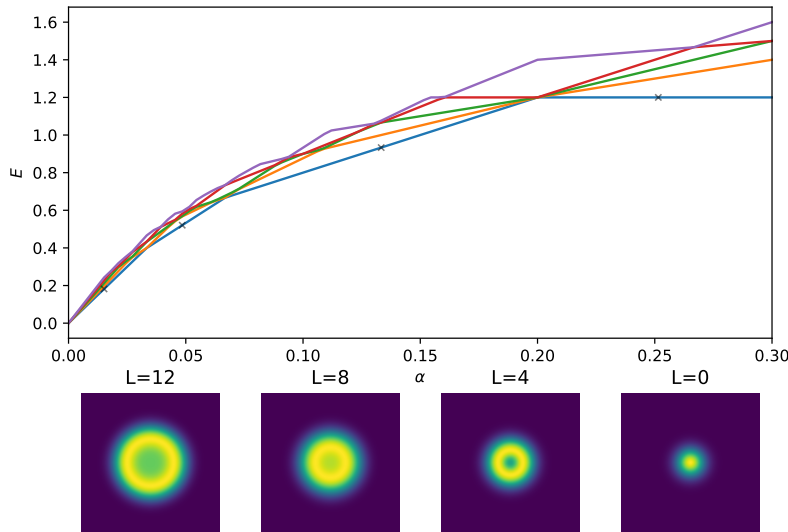


**Figure 3.4:** The low-energy spectrum of the model Hamiltonian Equation (3.9) for four particles shows crossings as the nature of the ground-state changes. For this sequence of states, the single particle density Equation (3.23) is shown at the locations indicated with black crosses. These states can be identified as the Gaussian ( $L = 0$ ), Pfaffian ( $L = 4$ ), Quasi-Hole ( $L = 8$ ) and Laughlin ( $L = 12$ ) state. The interaction strength was set to  $\eta = 0.1$ .

to look at the spectrum is in terms of the so called *Yrast spectrum*, shown in Figure 3.5. Here the interaction energy (eigenvalue of the interaction Hamiltonian in Equation (3.9)) of the lowest lying states is depicted as a function of angular momentum. The dashed black line denotes the *Yrast line*, which connects the lowest energy states for increasing angular momentum. Some important properties of the system can be read of from this spectrum. When the system has no angular momentum



$L = 0$ , all bosons occupy the lowest angular momentum mode  $m = 0$  which leads to a large interaction energy. As the angular momentum is increased, the particles can occupy higher modes  $m$  leading to a spread of the wavefunction in the plane that decreases interactions. For a total angular momentum of  $L = N(N - 1)$  (and higher), the interaction energy of the ground state vanishes as this is the Laughlin state Equation (2.28). This can be seen from the following arguments. The bosonic Laughlin state is of the form

$$\Psi_L(z_1, \dots, z_N) \propto \prod_{i < j}^N (z_i - z_j)^2. \quad (3.18)$$

where the even exponent ensures symmetry under particle exchange. The Jastrow factors  $(z_i - z_j)$  prevent two particles from sitting on top of each other as it goes to zero in that case. Because the s-wave interaction has zero range it is apparent that this state has no interaction energy. As the number of pairs in Equation (3.18) counts  $N(N - 1)/2$ , the total angular momentum, which corresponds to the total power of  $z$ , is given by  $L = N(N - 1)$  as seen in the spectrum. For each state on the Yrast line, there exist a number of states with the same interaction energy but higher  $L$ , corresponding to centre of mass excitations [Vie08] of the original state. Also at zero interaction energy, a number of degenerate states exist with an  $L$  higher than the Laughlin state. Their degeneracy is determined by the number of ways to distribute additional flux quanta onto the  $N$  particles. The two intermediate states at  $L = 4$ , and  $L = 8$  are also worth mentioning, because they possess very interesting properties. The first non-trivial state  $L = 4$  is highly entangled and has a very high overlap with the Pfaffian state

$$\Psi_{Pf}(z_1, \dots, z_N) \propto \prod_{i < j}^N (z_i - z_j) \text{Pf} \left( \frac{1}{z_i - z_j} \right) \quad (3.19)$$

with the Pfaffian symbol defined as

$$\text{Pf} \left( \frac{1}{z_i - z_j} \right) = \mathcal{A} \left[ \frac{1}{z_1 - z_2} \frac{1}{z_3 - z_4} \dots \frac{1}{z_{N-1} - z_N} \right]. \quad (3.20)$$

It contains a factor  $\frac{1}{z_i - z_j}$  for every pair of coordinates where every coordinate is only considered once and is anti-symmetrized over all coordinates. This state possesses excitations with non-Abelian statistics (see Section 2.3) which are interesting for applications in quantum information. The next state in the sequence can be identified as the Laughlin quasi-particle state Equation (2.35) obtained by acting with a derivative on the Laughlin state

$$\Psi_{QP}(z_1, \dots, z_N) = \frac{\partial}{\partial z_1} \dots \frac{\partial}{\partial z_N} \Psi_L. \quad (3.21)$$

This state also features anyon excitations that are abelian and have a statistic of  $\alpha = 1/2$ .

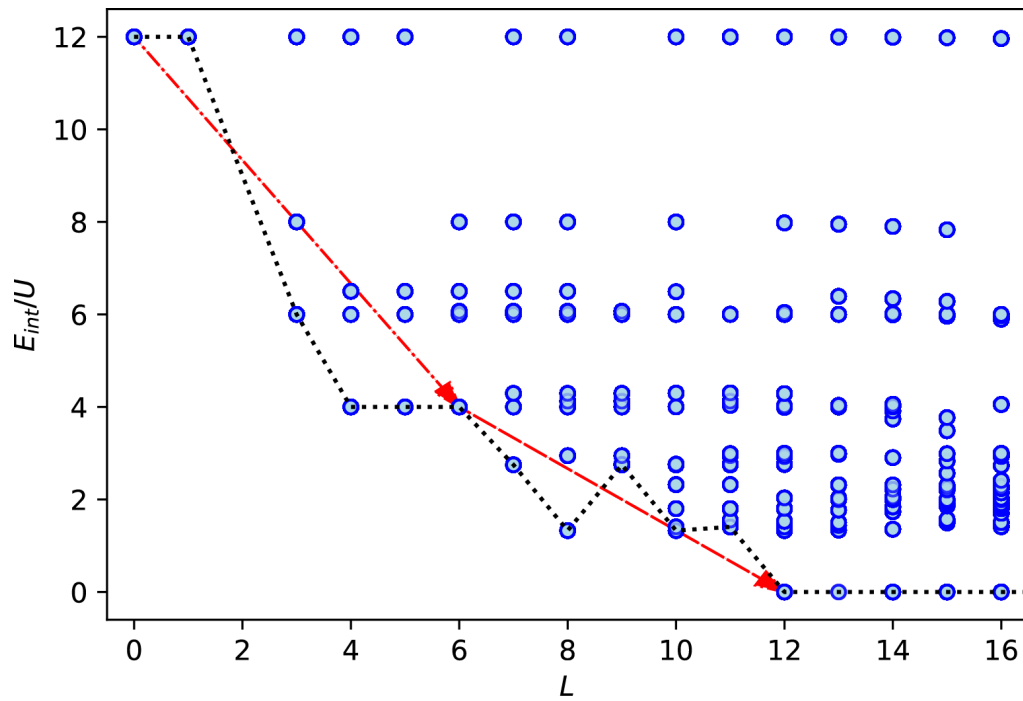


**Figure 3.5:** Interaction energy plotted against the angular momentum quantum number  $L_z$  for the lowest-lying eigenstates. This spectrum reveals the same hierarchy of groundstates as Figure 3.4, visible as the leftmost edge (Yrast line, black dashed). The Laughlin state ( $L = 12$ ) is the first one to have zero interaction energy, and all excitations of it are gapped in energy.



### 3.2.2 Observables

In order to obtain a real space picture of all these states, the one particle density distribution  $n(\mathbf{r})$  is shown for each state of the sequence  $L = 0, 4, 8, 12$ . As the angular momentum increases, the width of the density also broadens from the Gaussian shape state  $L = 0$  to a disk like distribution peaked on a ring. The single particle density operator  $n(\mathbf{r})$  is defined in terms of (bosonic) field operators

$$\Psi^\dagger(\mathbf{r}) = \sum_m a_m^\dagger \phi_m(\mathbf{r}) \quad (3.22)$$

denoting the creation of a particle at position  $\mathbf{r}$ . The sum runs over all angular momentum modes  $m$  and  $\phi_m(\mathbf{r})$  denote the single-particle wavefunctions. The real space density of one specific state  $\Phi$  can be computed in second quantisation as

$$n(\mathbf{r}) = \langle \Phi | \Psi^\dagger(\mathbf{r}) \Psi(\mathbf{r}) | \Phi \rangle \quad (3.23)$$

$$= \sum_{jk} \rho_{jk} \phi_j^*(\mathbf{r}) \phi_k(\mathbf{r}) \quad (3.24)$$

$$\rho_{jk} = \langle \Phi | a_j^\dagger a_k | \Phi \rangle \quad (3.25)$$

in terms of the density matrix  $\rho_{jk}$ . Due to angular momentum conservation, the density is always rationally symmetric, which is also reflected in Figure 3.4. Therefore the two particle correlation function  $g^{(2)}(\mathbf{r}, \mathbf{r}')$  has to be considered to gain further insight into the states structure. It is also considered as a mean of experimental detection, as recent imaging methods enable the extraction of this correlation function. It is defined in the same fashion as Equation (3.23) but for two particles at locations  $\mathbf{r}$  and  $\mathbf{r}'$ :

$$g^{(2)}(\mathbf{r}, \mathbf{r}') = \frac{\langle \Phi | \Psi^\dagger(\mathbf{r}) \Psi^\dagger(\mathbf{r}') \Psi(\mathbf{r}') \Psi(\mathbf{r}) \rangle}{n(\mathbf{r})n(\mathbf{r}')} \quad (3.26)$$

$$\langle \Phi | \Psi^\dagger(\mathbf{r}) \Psi^\dagger(\mathbf{r}') \Psi(\mathbf{r}') \rangle = \sum_{jklm} \rho_{jklm} \phi_j^*(\mathbf{r}) \phi_k^*(\mathbf{r}') \phi_l(\mathbf{r}') \phi_m(\mathbf{r}) \quad (3.27)$$

$$\rho_{jklm} = \langle \Phi | a_j^\dagger a_k^\dagger a_l a_m | \Phi \rangle \quad (3.28)$$

Because of the 2D geometry, is a four dimensional object in general. There are however special cases for the particles coordinate that simplify this dependence. For this it is instructive to expand the wavefunction term of Equation (3.26) in polar coordinates of the plane:

$$\phi_j^*(\mathbf{r}) \phi_k^*(\mathbf{r}') \phi_l(\mathbf{r}') \phi_m(\mathbf{r}) = \frac{r^j r'^k r'^l r^m}{\pi^2 \sqrt{j!k!l!m!}} e^{i(m-j)\phi} e^{i(l-k)\phi'} e^{-r^2} e^{-r'^2} \quad (3.29)$$

If one particle is fixed at the origin  $r' = 0, \phi' = 0$ , the correlation function is rotationally symmetric again, because the conservation of  $L$  implies  $j = m$ . In

this case it is sufficient to plot the radial dependence of Equation (3.26), which is shown in Figure 3.6 (top right). As you can see in the figure, the behaviour is different for the states of the sequence. The Gaussian state  $L = 0$  exhibits a flat correlation over all values of  $r$ , because the probability of finding two particles does not depend on their distance. The value of  $\frac{3}{4}$  deviates from the expected value of 1, because for a small particle number the normalisation  $\frac{N-1}{N}$  cannot be neglected. It is a combinatorial factor for fixing one of  $N$  particles and for the present case with  $N = 4$  it matches the observed value. The states with higher angular momentum  $L = 4, 8$  feature a more complex structure. Furthermore, the Laughlin state  $L = 12$  exhibits a characteristic hole at  $r = 0$  because the factor  $\prod_{i < j}^N (z_i - z_j)^2$  introduces many vortices into the system that suppress the approach of two particles. To break the rotational symmetry of the correlation function, the second particle is fixed at a position  $\mathbf{r}' \neq 0$  away from the origin revealing a more complex structure. This is shown for  $r' = \sqrt{N} = 2, \phi' = 0$  in Figure 3.6 (lower panels) for the sequence of ground states. The distinct shape of the second order correlation function for the Laughlin

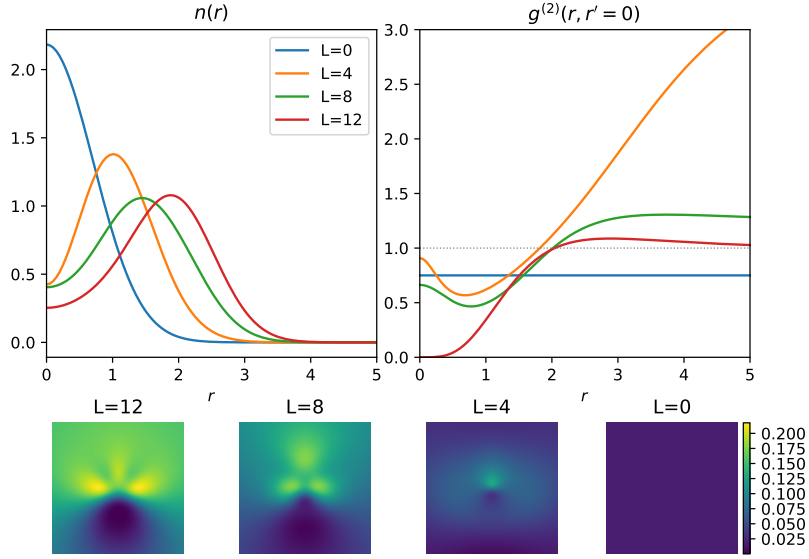


**Figure 3.6:** Single particle density and two particle correlation for four bosons at interaction strength  $\eta = 0.1$  for the sequence of states  $L = 0, 4, 8, 12$ . (a) The single particle density, defined in Equation (3.23). (b) The radial two particle correlation function Equation (3.26) is depicted for the same states as in (a) where the second particle is fixed at the origin. (c)-(f) Two dimensional plot of the correlation function where the second particle is fixed at  $r = \sqrt{4}$  to break angular symmetry.



state makes  $g^{(2)}$  a promising observable for detection of this state. To prepare one of these states in an actual experiment, one has to introduce angular momentum into the system while remaining in the ground state. As it was shown in Figure 3.3, an anharmonic perturbation of the trap is necessary to open up the level crossing and facilitate a transfer into the desired states. Thereby two strategies for preparation are possible. In [PPC04] the authors propose an adiabatic scheme where the external parameters are varied slowly enough to always remain in the ground state (Adiabatic theorem). The parameters in this case are the rotational frequency of the trap  $\Omega$  and the perturbation strength  $\epsilon$ . The relevant quantity, limiting the adiabatic transfers

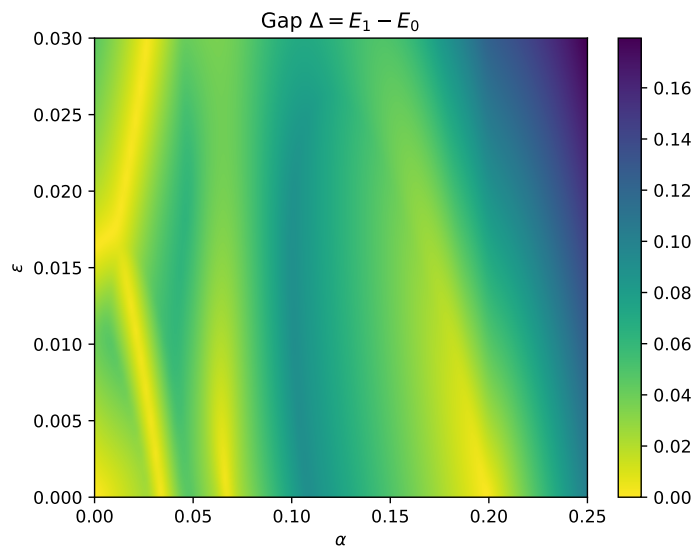


**Figure 3.7:** Energy gap between ground and first excited state for  $N = 4$  bosons as a function of rotational frequency  $\Omega$  and perturbation strength  $\epsilon$ .

speed, is the size of the energy gap  $\Delta$  between ground and first excited state. The size of the gap depends non-trivially on the external parameters, as it is shown in Figure 3.7. Therefore both parameters have to be varied simultaneously to trace out a path in the  $\alpha - \epsilon$  landscape maximizing the gap size and therefore minimizing the total time of the transfer. In Figure 3.7, each transition to the next state in the ground state sequence is indicated by a band of very small values of  $\Delta$  coming from high values of  $\alpha$ . Especially for the last transition  $L = 8 \rightarrow 12$  the gap remains small even for strong perturbations. This makes preparation of the Laughlin state slow and difficult, because the path in parameter space must be followed quite precisely. Because of experimental imperfections the precise shape of the gap might be different and render this route very difficult. Another scheme was proposed in [BHM08] that relies on pulses instead of adiabatic evolution. For this purpose the coefficients  $\epsilon$  and

$\Omega$  in Equation (3.16) are considered time-dependent and gaussian shaped pulses of these parameters are applied. Because the quadrupole deformation Equation (3.17) only couples states with a relative angular momentum of  $m = 2$ , either multiple pulses or higher order deformations have to be considered. In Figure 3.5 this is indicated with the two red arrows first coupling the states  $L = 0$  and  $L = 6$  and subsequently to  $L = 12$ . The authors claim this scheme to be twice as fast compared to the adiabatic case and more robust to experimental imperfections.

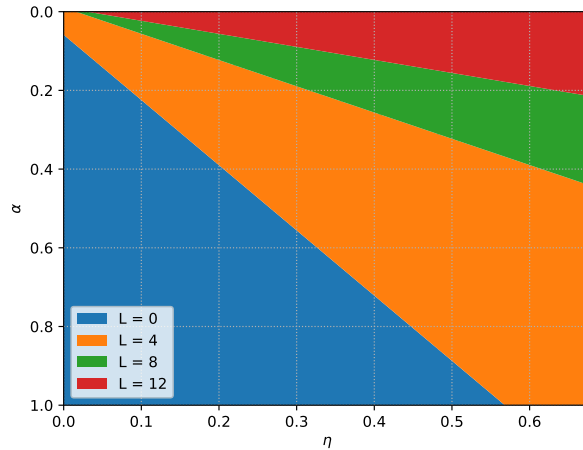


**Figure 3.8:** Critical speed of rotation  $\alpha$  required to reach a ground-state of total angular momentum  $L$  as a function of interaction strength  $\eta$ . An experiment is performed at a particular value of  $\eta$  where the speed of rotation is increased  $\alpha \rightarrow 0$  following a vertical line. For larger interaction strengths all states can be prepared at a lower rotational frequencies  $\alpha$ .



### 3.3 Spinful ultracold fermion systems

Considering the large amount of literature on bosonic quantum Hall states using ultracold atoms, there exists very little work on ultracold fermions in this regard. There are however a number of reasons why ultracold fermions might be a good platform for realizing quantum Hall states that should be discussed in the following. First of all, the quantum Hall effect and its hierarchy of states were discovered in condensed matter systems, where electrons are the relevant constituents. If one wants to investigate this effect and open questions like the nature of the  $5/2$  state, ultracold fermions seem like the obvious choice because of their statistics. A second argument is of more technical nature. As described in Section 3.2, the critical speed of rotation to reach the Laughlin states and its precursors is set by the interactions strength. In a cold atoms experiment, this is given in terms of the s-wave scattering length, which can be tuned using a Feshbach resonance. For bosonic particles, the divergence in scattering length near such a Feshbach resonance is usually accompanied by strong three-body losses, making the system unstable. Therefore, the background scattering length away from the resonance is often used in practice, leading to relatively weak interactions. For  $^{87}\text{Rb}$ , for example, the zero-field scattering length on the order of  $\approx 100a_B$  leads to an interaction parameter  $\eta$  (as in Equation (3.5)) of only 0.05 for typical trap parameters. As a consequence, the critical speed of rotation  $\Omega_c$  (and correspondingly  $\alpha_c$ ) is quite high, as observable in Figure 3.4. This presents an experimental challenge, as the frequency of rotation has to almost match the trap frequency. In that case, anharmonic terms of the gaussian beam and other imperfections can lead to heating or simply loss of atoms from the trap. In this regard, fermionic species like  $^6\text{Li}$  offer much higher scattering lengths up to a divergence at the resonance yielding large interactions strengths  $\eta$ . This reduces the necessary critical speeds of rotation  $\Omega_c$  and in turn may reduce some of the problems discussed above that have so far prevented a realisation.

#### Connection to condensed matter systems

However, realisation of quantum Hall states with ultracold fermionic gases has two very distinct properties from the semiconductor structures underlying the original discovery. Unlike the condensed matter systems, where a very strong external magnetic field leads to a spin polarization of the electrons, ultracold gases can feature multiple spin components. This is because the energy shift due to an artificial magnetic field (at least for rotating traps) does not depend on the spin degree of freedom. Therefore, the system can be viewed as a multi layer system in analogy to semiconductor structures featuring multiple layers. In the case of an effective spin  $1/2$  system, like the two lowest hyperfine levels of  $^6\text{Li}$ , this resembles a bilayer system where the inter- and intra-layer interactions are determined by the different spin interactions. The dominating interaction for ultracold atoms is s-wave scatter-

ing, which is explained in more detail in Section 4.1. For identical fermions, this interactions vanishes because of the wavefunctions anti-symmetry and only higher partial wave components would contribute. Therefore equal spin fermions do not interact on an s-wave Feshbach resonance, only these with a different spin. In the bilayer picture, this is equivalent to two integer quantum Hall systems for each spin component with an interaction among the two. This configuration is unusual and unique to the ultracold fermions case, because in a condensed matter bilayer system the inter-layer interaction would be much stronger than the intra-layer one. In order to study these kind of systems, an exact diagonalisation study is performed to identify possible ground states and their properties.

### 3.3.1 Exact diagonalisation results

As in the bosonic calculations in Section 3.2, a occupation number (Fock-Darwin) basis is chosen for each spin component. The resulting state vector is then a tensor product of the two spin states.

$$|n_0, n_1, \dots, n_M\rangle_{\uparrow} |n_0, n_1, \dots, n_M\rangle_{\downarrow} = \sum_m \left(c_{m,\uparrow}^{\dagger}\right)^{n_{m,\uparrow}} \left(c_{m,\downarrow}^{\dagger}\right)^{n_{m,\downarrow}} |vac\rangle \quad (3.30)$$

The fermionic operators  $c_{m,\sigma}$  act on an angular momentum mode  $m$  and spin component  $\sigma \in \{\uparrow, \downarrow\}$  obeying the anti-commutation relations

$$\{c_{m,\sigma}^{\dagger}, c_{n,\sigma'}\} = \delta_{mn}\delta_{\sigma\sigma'}, \quad \{c_{m,\sigma}, c_{n,\sigma'}\} = 0, \quad \{c_{m,\sigma}^{\dagger}, c_{n,\sigma'}^{\dagger}\} = 0. \quad (3.31)$$

This can be pictorially represented as

$$|1, 0, 1, 0, 1, 0, 0, 1\rangle_{\uparrow} |0, 1, 1, 1, 0, 0, 1, 1\rangle_{\downarrow} = \left| \begin{array}{cccccccc} \color{blue}\bullet & & \color{blue}\bullet & & \color{blue}\bullet & & & \color{blue}\bullet \\ \color{green}\bullet & \color{green}\bullet & \color{green}\bullet & & & & \color{green}\bullet & \color{green}\bullet \end{array} \right\rangle$$

because the occupation numbers of each mode  $n_{m,\sigma} = 0, 1$  are restricted by the Pauli exclusion principle. The Hamiltonian describing the confining potential and interactions between particles is the same as in Equation (3.9), because the interaction matrix element  $V_{\{m\}}^{(\sigma,\sigma')}$  in Equation (3.10) does not depend on the spin. However the changed statistics in terms of the anti-commutation relations must be taken into account in constructing the Hamiltonian matrix. Afterwards, the lowest-lying states are computed for different speeds of rotation  $\alpha$ , to obtain the energy spectrum depicted in Figure 3.9 at an interaction strength of  $\eta = 0.5$ . As the states now feature a spin degree of freedom, we have the total spin  $S$  as an additional observable. In second quantisation, the single particle spin operators can be represented as

$$S_i = \frac{1}{2} \sum_{\sigma,\sigma'} c_{\sigma}^{\dagger} \sigma_{\sigma,\sigma'}^i c_{\sigma'} \quad (3.32)$$



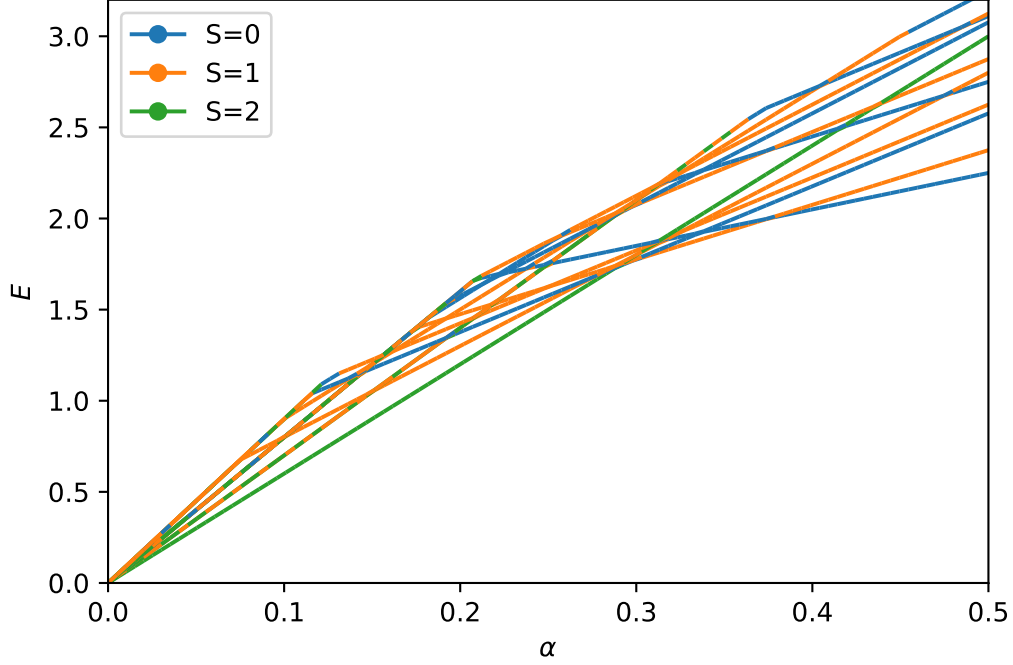


**Figure 3.9:** Low energy spectrum of four particles  $N_{\uparrow} = N_{\downarrow} = 2$  as a function of rotational frequency  $\alpha$ . Total spin of the states is indicated by colour of the lines. The interaction strength was set to  $\eta = 0.25$ .

where  $i = \{x, y, z\}$  and  $\sigma^i$  denote the Pauli matrices. With this, the total spin  $S^2$  of the many-body state can be expressed as

$$S^2 = S_- S_+ + S_z(S_z + 1) \quad (3.33)$$

$$S_- = \sum_{j,\sigma,\sigma'} c_{j,\sigma}^\dagger c_{j,\sigma'} \quad (3.34)$$

$$S_+ = \sum_{j,\sigma,\sigma'} c_{j,\sigma'}^\dagger c_{j,\sigma} \quad (3.35)$$

$$S_z = \frac{1}{2} \sum_j n_{j,\uparrow} - n_{j,\downarrow} = \frac{1}{2}(N_{\uparrow} - N_{\downarrow}) \quad (3.36)$$

in terms of the spin raising and lowering operators. This is a convenient form, as for the balanced case  $N_{\uparrow} = N_{\downarrow}$  the projection  $S_z$  of the total spin vanishes. Therefore, only spin states in the  $S_z = 0$  subspace are allowed, that can be calculated from the Clebsch-Gordan coefficients:

particle number	spin states
$N$	$ S, S_z\rangle$
2	$ 0, 0\rangle,  1, 0\rangle,  2, 0\rangle$
3	$ 0, 0\rangle,  1, 0\rangle,  2, 0\rangle,  3, 0\rangle$
4	$ 0, 0\rangle,  1, 0\rangle,  2, 0\rangle,  3, 0\rangle,  4, 0\rangle$

The remaining product of operators in Equation (3.33) is brought into normal ordered form

$$S_- S_+ = \sum_{j,k} c_{j,\sigma}^\dagger c_{j,\sigma'} c_{k,\sigma'}^\dagger c_{k,\sigma} \quad (3.37)$$

$$= \sum_j c_{j,\sigma}^\dagger c_{j,\sigma} + \sum_{j,k} c_{j,\sigma}^\dagger c_{k,\sigma'}^\dagger c_{j,\sigma'} c_{k,\sigma}. \quad (3.38)$$

Because the total spin commutes with the Hamiltonian  $[\mathcal{H}, S^2] = 0$ , the eigenstates of  $\mathcal{H}$  are simultaneous eigenstates of  $S^2$

$$S^2 |\Phi\rangle = S(S+1) |\Phi\rangle. \quad (3.39)$$

From this, the eigenvalue  $S$  is computed, which is encoded as colour in Figure 3.9. As it is shown in the figure for four particles ( $N_\uparrow = N_\downarrow = 2$ ), there exist different manifolds for each value of the total spin  $S = 0, 1, 2$  that cross each other, but do not couple. The variations in total spin along a seemingly straight line, especially for small values of  $\alpha$  are due to a large number of states coming in from larger energies, that are however not plotted for clarity. The ground states goes trough a sequence of total spins  $S = 0, 1, 0, 1, 2$ , however the crossings between the different states will not become avoided when a perturbation of the form Equation (3.16) is introduced. This is due to the fact that there are no spin changing collisions present because they are energetically detuned. In Figure 3.10 the Yrast spectrum of states is shown for the same parameters as in Figure 3.9. In addition to the bosonic picture Figure 3.5, the total spin of each state is encoded by different colours and markers for clarity. As it can be inferred from this picture, also for this unusual configuration of interactions a number of correlated, non-trivial states exists. For example one can again identify a Laughlin like state at  $L = 6$  and  $S = 2$ , as it is the first one to suppress interaction energy. At the next highest  $L$  also a state with  $S = 1$  and zero interaction energy appears, whereas for  $S = 0$  this only happens at  $L = 8$ . To identify the different states and their wavefunction in a first quantised form like the original Laughlin state Equation (2.28), the state vector has to be rewritten as follows. In order to express a state given in the occupation number basis Equation (3.30) in first quantisation, it has to be rewritten in terms of single particle quantum numbers. For only one spin component, this is achieved via the anti symmetrized sum over all particles

$$|n_0, n_1, \dots, n_M\rangle = \mathcal{S}_- |i_0, i_1, \dots, i_N\rangle = \sum_{\{\sigma\}} \text{sgn}(\sigma) |i_{\sigma(0)} i_{\sigma(1)} \dots i_{\sigma(N)}\rangle \quad (3.40)$$



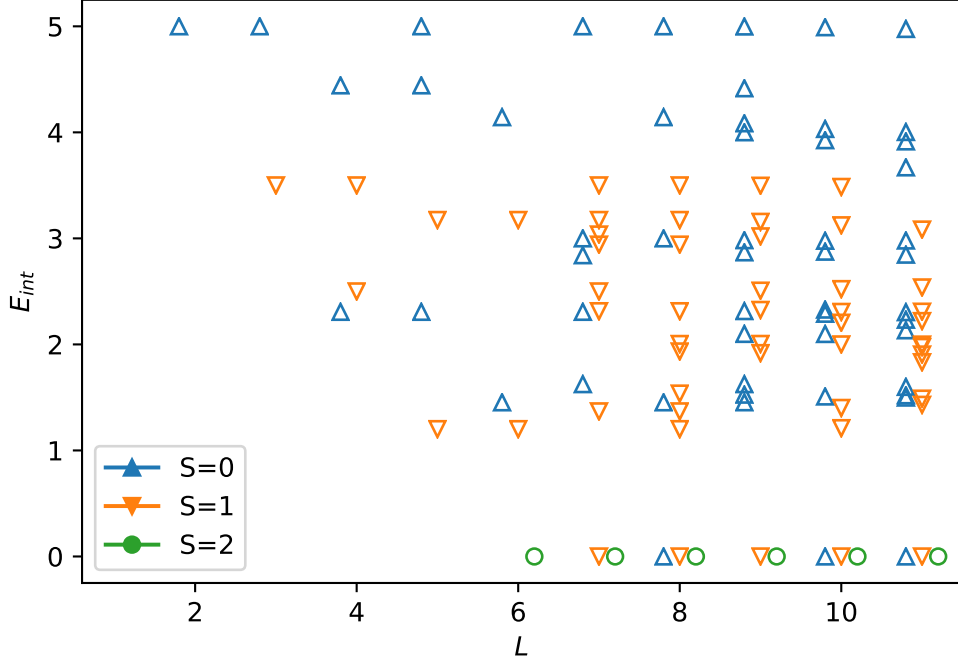


**Figure 3.10: Yrast spectrum for  $N_{\uparrow} = N_{\downarrow} = 2$ .** The interaction energy  $E_{int}$  as a function of total angular momentum  $L$  is shown. For each state the total spin  $S$  is encoded as a different colour and marker. Each spin component is slightly shifted horizontally around the integer values of  $L$  for clarity. The sequence of groundstates can be identified at the leftmost edge (Yrast line).

where  $|i_j\rangle$  denotes the angular momentum orbital  $i$  occupied by particle  $j$ . The single particle orbitals  $|i\rangle$  are directly related to the single particle wavefunctions  $\psi_m(z) \propto z^m$  when neglecting the gaussian envelope factor. As a result, the single particle wavefunction is a polynomial in the particle positions  $z_i$ , where each monomial corresponds to one term in Equation (3.40).

$$\psi_{\{i\}}(z_1, \dots, z_N) = \sum_{\{\sigma\}} \text{sgn}(\sigma) z_0^{i_{\sigma(0)}} z_1^{i_{\sigma(1)}} \dots z_N^{i_{\sigma(N)}} \quad (3.41)$$

Because each state is also an eigenstate of total angular momentum  $L$ , the powers of  $z_i$  add up to  $L$  for all individual monomials. This procedure can be generalized to two spin components, where the coordinates for spin-up particles are denoted as

$z_i$  and spin-down particles as  $x_i$  ( $z$  and  $x$  still are complex coordinates of the plane)

$$\psi_{\{i\}}(\{z\}, \{x\}) = \left( \sum_{\{\sigma\}} \text{sgn}(\sigma) z_0^{i_{\sigma(0)}} z_1^{i_{\sigma(1)}} \dots z_N^{i_{\sigma(N)}} \right) \left( \sum_{\{\tau\}} \text{sgn}(\tau) x_0^{i_{\tau(0)}} x_1^{i_{\tau(1)}} \dots x_N^{i_{\tau(N)}} \right). \quad (3.42)$$

In this way, any general state can be rewritten from the second into first quantised form as

$$|\psi\rangle = \sum_i \xi_i |i\rangle \rightarrow \psi(\{z\}, \{x\}) = \sum_i \xi_i \psi_{\{i\}}(\{z\}, \{x\}) \quad (3.43)$$

with  $|i\rangle$  denoting all basis states and  $\xi_i$  the entries of the numerically obtained eigenstates (see Chapter A for more details). By factorization of the resulting polynomial into vortex-like terms ( $z_i - z_j$ ), more insight into the states can be gained. The procedure described above can also be generalized to a more general theory described in [AR11], where the (anti-)symmetrized monomials of the form Equation (3.41) are related to 'root partitions' of Polynomials. From these partitions and a number of squeezing rules, a variety of complicated FQHE states can be derived through a connection to the theory of Jack polynomials. The authors of [AR11] also consider the case of spin-1/2 particles, however not for the special kind of interaction considered in this thesis. It would be interesting to see whether such a squeezing procedure could be derived and employed in order to identify states for which the numerical procedure described above is not applicable. In the following, the wavefunctions for some of the states in the ground-state sequence, which could be identified, are presented. The wavefunction of the trivial ground-state at lowest  $L$  is given by the Vandermonde determinant

$$\psi_V(\{z\}, \{x\}) = \prod_{i < j}^{N_{\uparrow}} (z_i - z_j) \prod_{k < l}^{N_{\downarrow}} (x_k - x_l) \quad (3.44)$$

that ensures antisymmetry of the wavefunction under exchange of equal spin particles. This state simply describes the two independent Fermi seas of a non-interacting mixture of two spin-components. Therefore it is also a common pre-factor for all wavefunctions of states with higher  $L$ . The total angular momentum of the Vandermonde determinant Equation (3.44) is given by the total power of  $z_i$  and  $x_j$ , which is determined by the number of distinct pairs for each spin component

$$L_V = \frac{N_{\uparrow}(N_{\uparrow} - 1)}{2} + \frac{N_{\downarrow}(N_{\downarrow} - 1)}{2} \stackrel{N_{\uparrow}=N_{\downarrow}=N}{=} N(N - 1). \quad (3.45)$$

Therefore the ground state with lowest angular momentum has a non-vanishing  $L$  compared to the bosonic case. Subsequent states in the sequence of groundstates in Figure 3.9 can be identified by constructing the polynomial wavefunction as outlined in Equation (3.42). However, the number of monomials in the wavefunction grows as  $N_{\uparrow}!N_{\downarrow}!$ , which requires factorization by a computer algebra system. When the



$N = 2$		$N = 3$		$N = 4$	
$L$	$L_R$	$L$	$L_R$	$L$	$L_R$
2	0	6	0	12	0
3	1	7	1	13	1
4	2	8	2	14	2
6	4	10	4	16	4
		15	9	21	9
				28	16

**Table 3.1:** Total angular momenta  $L$  and for the sequence of ground states for different particle numbers  $N_\uparrow = N_\downarrow = N$ .  $L_R$  denotes inter-spin angular momentum where the Vandermonte determinant contribution is subtracted.

spectrum of states like in Figure 3.10 is computed in the balanced case  $N_\uparrow = N_\downarrow = N$  for small particle numbers  $N = 2, 3, 4$ , a sequence of groundstates can be denoted that is shown in Table 3.1. As all higher wavefunctions are of the form  $\psi = \psi_V \tilde{\psi}$ , the total angular momentum  $L = L_V + L_R$  is composed of two contributions. The first one given by the angular momentum  $L_V$  of the Vandermonte determinant Equation (3.44) and the second one determined by the number of vortices introduced between the two spin components  $L_R$ . As it can be seen from Table 3.1, the sequence of  $L_R$  is independent of particle number. The first two wavefunctions in this hierarchy can be written as

$$\tilde{\psi}_{L_R=1}(\{z\}, \{x\}) = \sum_i z_i - \sum_i x_i \quad (3.46)$$

$$\tilde{\psi}_{L_R=2}(\{z\}, \{x\}) = \left( \sum_i z_i - \sum_i x_i \right)^2. \quad (3.47)$$

They represent one and two vortices among centre of mass coordinates of the two spin components, respectively. Also the last state in the sequence can be identified for the particle numbers shown in Table 3.1

$$\tilde{\psi}(\{z\}, \{x\}) = \prod_{i,j}^N (x_i - z_j) \quad (3.48)$$

as vortices between all pairs of different spins. This is a special form of the general Halperin [Hal83b]  $(m, m, n)$  wavefunction

$$\tilde{\psi}_{(m,m,n)}(\{z\}, \{x\}) = \prod_{i < j}^{N_{\uparrow}} (z_i - z_j)^m \prod_{k < l}^{N_{\downarrow}} (x_k - x_l)^m \prod_{i,k}^N (x_i - z_k)^n \quad (3.49)$$

which he considered as a ground state of two spin components interacting via spin-independent coulomb interaction. For fermions, the power  $m$  in the first two determinant-like factors has to be odd. The total angular momentum of this state can be calculated as

$$L_{(m,m,n)} = mN(N-1) + nN^2 \quad (3.50)$$

and it corresponds to a filling fraction  $\nu$  of

$$\nu = \frac{2}{m+n}. \quad (3.51)$$

The groundstate with highest  $L$  in Table 3.1 is given by the  $(1, 1, 1)$  state in this notation leading to a filling fraction of  $\nu = 1$ .

In Figure 3.11 and Figure B.1 the same spectrum of states as in Figure 3.10 is shown for higher particle numbers  $N$ . As expected, a larger number of states arises and higher total spins  $S$  become accessible.

Because the energies belonging to the different spin manifolds cross and do not couple as visible in Figure 3.9, there is no straightforward route to prepare the highly correlated Laughlin-like state  $\Psi_{(1,1,1)}$  starting from the trivial ground state Equation (3.44) when a sample with  $N_{\uparrow} = N_{\downarrow}$  is prepared initially. Nevertheless two possible ways to interesting states exist: (i) While remaining in the same spin manifold a sequence of states with increasing angular momenta  $L$  can be prepared also leading to a vanishing interaction energy only at a larger values of  $L$  when compared to the highest spin state. This can be seen for example in Figure 3.11 where the state  $\Psi_{(S,L)=(0,8)}$  has the same vanishing interaction energy as  $\Psi_{(2,6)}$ . Also intermediate states can possess interesting properties which can be observed from their wavefunctions and correlation functions Figure B.7 and Figure 3.17. (ii) To reach the latter state  $\Psi_{(1,1,1)}$ , the preparation already has to start out from a state with  $S = 2$  and  $S_z = 0$  which is not the ground-state of the non-rotating trap. How this state can be prepared experimentally is still an open question. One possibility would be to make use of singlet-triplet oscillations in a magnetic field gradient as described in [Gre+13]. Afterwards, the rate of rotation is increased until this state becomes the ground-state of the rotating Hamiltonian. As visible in the energy diagram Figure 3.9 the lowest state of the  $S = 2$  manifold experiences no crossings with other states of the same spin making this transfer trivial. In order to pursue first route (i), the way of preparation is the same as in the bosonic case. By adiabatically introducing a rotating trap anisotropy Equation (3.17) an avoided



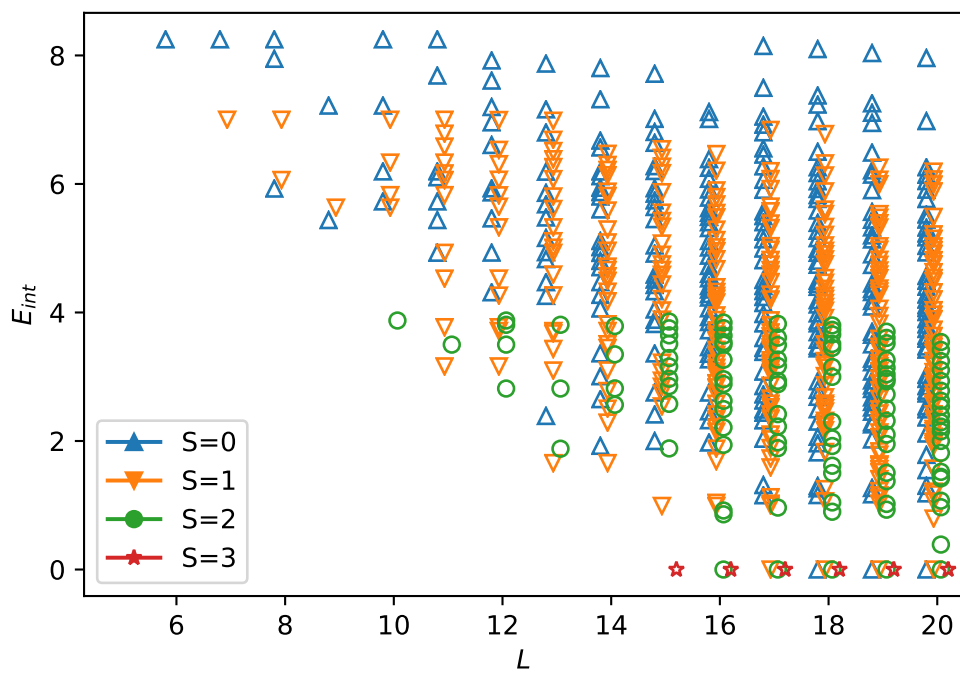
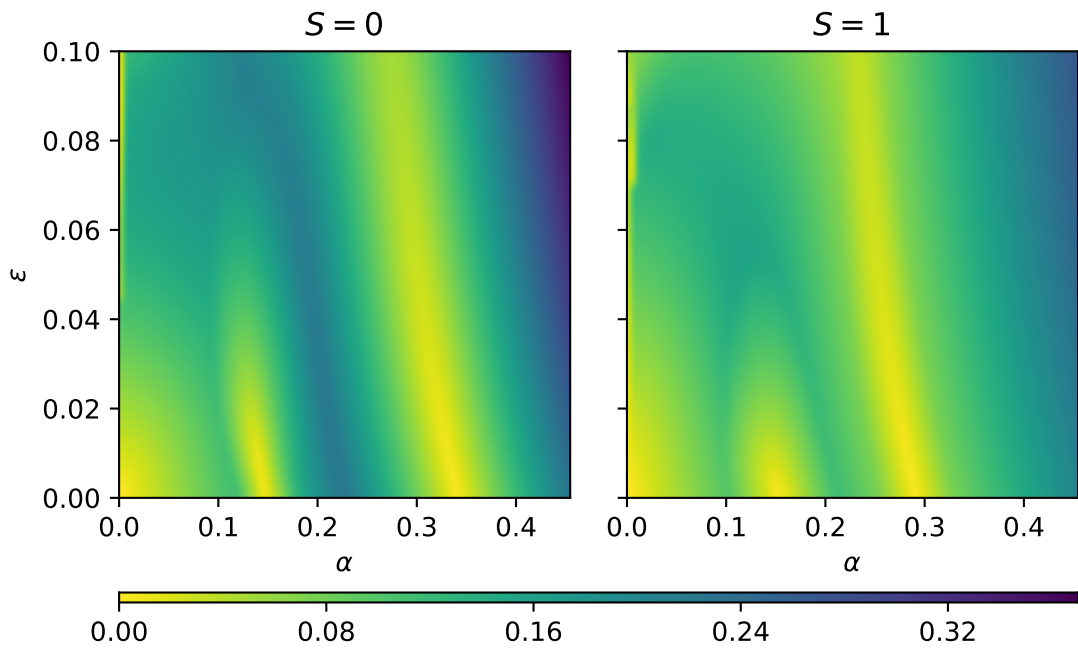


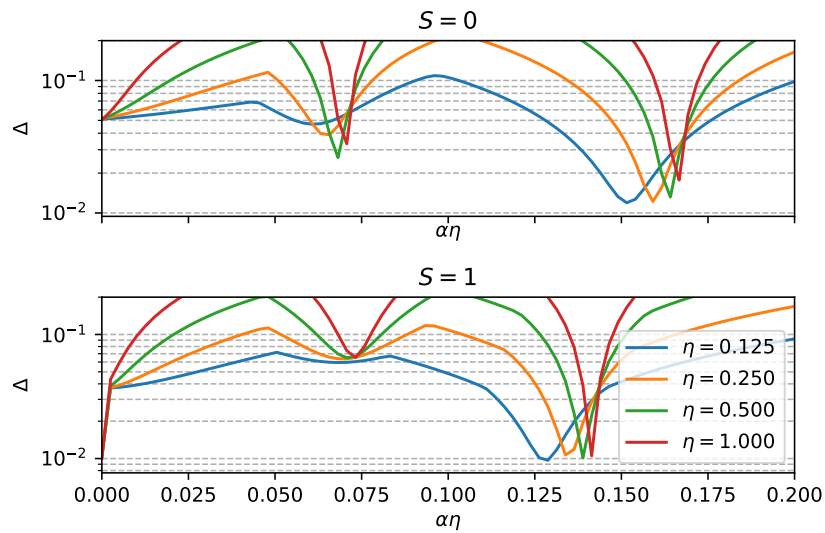
**Figure 3.11: Yrast spectrum for  $N_{\uparrow} = N_{\downarrow} = 3$ .** Interaction energy as a function of total angular momentum  $L$  is displayed analogous to Figure 3.10. The different spin components are shifted horizontally for clarity.

crossing between states with equal spin  $S$  and different angular momentum  $L$  opens up. When this is done sufficiently slow the system follows the instantaneous ground state allowing preparation of a state with increased  $L$ . The speed of this adiabatic transfer is limited by the size of the energy gap  $\Delta = E_1 - E_0$  between the ground- and first excited state. Therefore the gap size for various speeds of rotation  $\alpha$  and perturbation strengths  $\epsilon$  is computed and shown in Figure 3.12. The resulting picture Figure 3.12a looks comparable to the gap calculated for Bosons in Figure 3.7, however larger maximal values for  $\alpha$  and  $\epsilon$  have been chosen in the fermionic case. At each avoided crossing the gap size features a minimum, indicating two crossings in both the  $S = 0$  and  $S = 1$  sector. The last minimum at  $\alpha \rightarrow 0$  is due to the degeneracy at the de-confinement limit also giving rise to some numerical artefacts at the very left edge of the picture. For  $N_\uparrow = N_\downarrow = 2$  the spin sector  $S = 2$  is also present, however it is not shown in the figure as it doesn't feature any level crossings making the gap trivial. In order to take exact readings of the gap size, a one-dimensional cut at an intermediate perturbation strength of  $\epsilon = 0.02$  is depicted in Figure 3.12b. Because the exact gap sizes can be very small, but are of particular importance for an adiabatic preparation, they are shown on a logarithmic scale. Because the locations of the crossings shift approximately linearly towards lower speeds of rotation for increasing interaction strengths  $\eta$ , the x-axis is scaled in a way to remove this dependence. After this only a small trend towards higher  $\alpha$  for increasing interactions  $\eta$  remains visible. For  $S = 1$  the minimal size of the gap does not visibly depend on the strength of interaction, however this is not the case for  $S = 0$ . Here the gap size increases with  $\eta$  for the first crossing (larger value of  $\alpha$ ) but decreases (with the exception of  $\eta = 1$ ) at the second one. However these variations are only on the order of two while  $\eta$  is varied by almost an order of magnitude. This indicates the gap size to be independent of interaction strength to first order. It is worth noting, however, that the size of the first gap (coming from large values of  $\alpha$ ) is smaller than for the second one, contrary to the bosonic case Figure 3.7. The same analysis can be repeated for the case of  $N_\uparrow = N_\downarrow = 2$  atoms which is shown in Figure 3.13 and Figure B.4 for more detail. Here the three lowest spin manifolds show avoided level crossings. Unexpectedly, the gap-size of the first crossing does not increase for larger perturbations  $\epsilon$  for all spins, but rather remains approximately constant. Only the latter crossings show the expected behaviour. This turns out to be unfavourable when mapping out a path of maximal gap size for an adiabatic preparation. As noted before the positions  $\alpha$  at which the systems ground-state changes character depend on the interaction parameter  $\eta$  which is of special importance when preparing those states in a rotating trap. With larger possible values of  $\eta$  interesting states are already accessible at lower speeds of rotation  $\alpha$  reducing the impact of trap imperfections that come into play especially for  $\alpha \rightarrow 0$ . Therefore Figure 3.14 shows the critical speeds of rotation required to reach a state with particular  $L$  as a function of the interaction strength  $\eta$ . For two atoms per spin (a) and a value of  $\eta = 0.25$  the last state of the sequence can already be reached





(a) The gap  $\Delta$  is computed as a function of rotational frequency  $\alpha$  and perturbation strength  $\epsilon$  for an interaction parameter  $\eta = 0.25$ .



(b) Cut of (a) along a line with  $\epsilon = 0.02$  shown on a logarithmic scale for different interactions strengths  $\eta$ .

**Figure 3.12:** Energy gap between ground- and first excited state inside a manifold of spin  $S$  for  $N_{\uparrow} = N_{\downarrow} = 2$  particles. The frequency of rotation  $\alpha$  has been scaled by  $\eta$  in order to collapse the lines of different  $\eta$  onto each other.

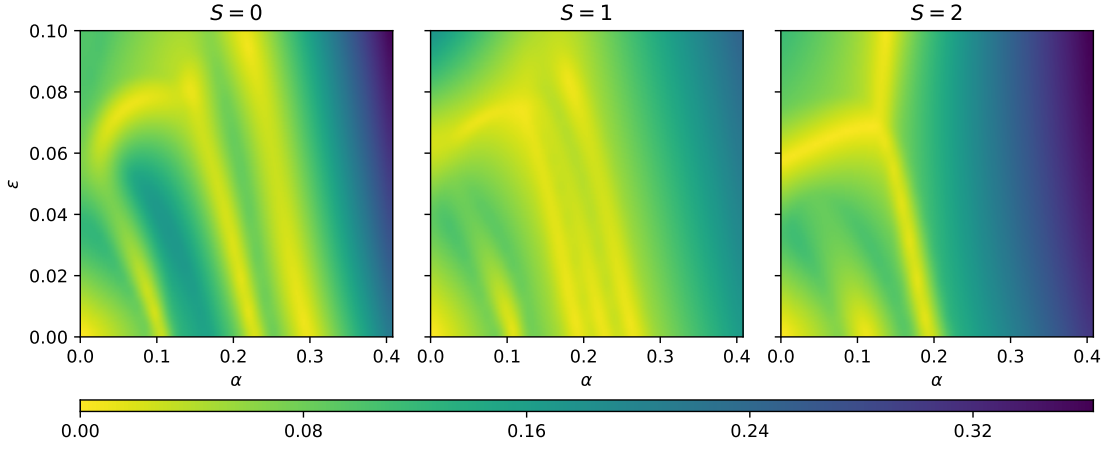
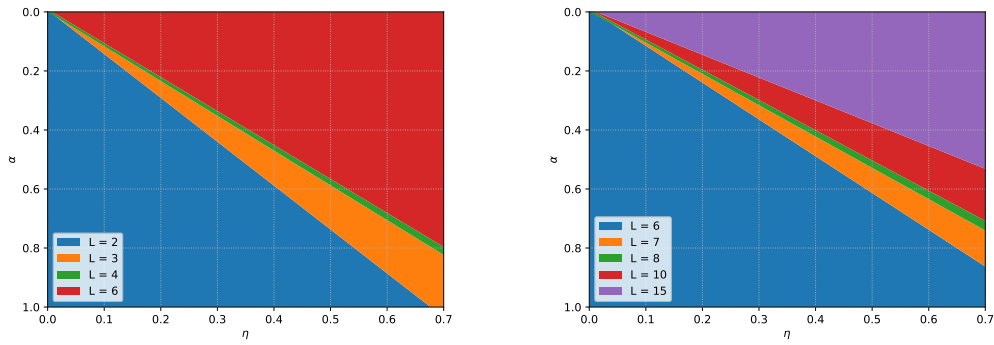


**Figure 3.13:** Energy gap like in Figure 3.12 for  $N_{\uparrow} = N_{\downarrow} = 3$  particles



(a) Two atoms per spin  $N_{\uparrow} = N_{\downarrow} = 2$ . (b) Three atoms per spin  $N_{\uparrow} = N_{\downarrow} = 3$ .

**Figure 3.14:** Critical speed of rotation  $\alpha$  required to reach a ground-state of total angular momentum  $L$  as a function of interaction strength  $\eta$ . An experiment is performed at a particular value of  $\eta$  where the speed of rotation is increased  $\alpha \rightarrow 0$  following a vertical line. For larger interaction strengths all states can be prepared at a lower rotational frequencies  $\alpha$ .



at 70 % of the trap frequency. As the number of atoms is increased, the required critical speeds shift towards larger values as apparent from Figure 3.14b. The values of  $\eta$  shown in the figure are easily attainable using the Feshbach resonance of  ${}^6\text{Li}$  as calculated in Section 5.4. This is an advantage compared to experiments using Bosons [GSC10] where only relatively weak interactions of  $\eta = 0.0054$  could be used.

### 3.3.2 Methods of detection

To reveal all the states discussed above in an actual experiment, the right observables must be used in order to distinguish among them and other states. Because the size of the wavefunction in the trap is on the order of the harmonic oscillator length  $l = \sqrt{\hbar/M\omega}$ , it is very difficult to resolve the density optically. Fortunately, all states in the lowest Landau level remain self similar under a free expansion from the trap. This particular property is described as a *wave-function microscope* in [RC03]. Free expansion in space, also called time of flight, is a common experimental technique to map the momentum distribution of an initial state into position space after a sufficiently long time. This can be expressed as

$$|\psi(\mathbf{r}, t)|^2 \propto \left| \tilde{\psi}_0 \left( \frac{M\mathbf{r}}{\hbar t} \right) \right|^2 \left( \frac{M}{2\pi\hbar t} \right)^3 \quad (3.52)$$

where  $\tilde{\psi}_0$  is the Fourier transform of the initial position space wavefunction. In general this only holds for non-interacting particles. Although interactions play a very important role for correlated states in the LLL while being trapped, these interactions can be neglected during a free expansion. For a LLL state, the probability density after a time  $t$  can be calculated to see

$$|\psi(z, x_3, t)|^2 \propto \left| \frac{\psi_0 \left( \frac{z}{1+i\omega t}, \frac{x_3}{\sqrt{1+\omega^2 t^2}} \right)}{(1+i\omega t)(1+\omega_3^2 t^2)^{1/2}} \right|^2 \quad (3.53)$$

that this is simply the initial probability density rescaled and rotated in the plane and also scaled in  $z$  direction ( $x_3$ ). Here  $\omega$  denotes the trapping frequency in the plane and  $\omega_3$  in  $z$  direction. This property is even more apparent in the asymptotic form

$$|\psi(z, x_3, t)|^2 \xrightarrow{t \rightarrow \infty} \frac{\left| \psi_0 \left( \frac{-iz}{\omega t}, \frac{x_3}{\omega_3 t} \right) \right|^2}{(\omega t)^2 (\omega_3 t)} \quad (3.54)$$

where the density is rotated in the plane by  $\pi/2$  and magnified by  $\omega t$ . This generalizes trivially to a state of multiple non-interacting particles. The authors of [RC03] argue that interactions can be neglected, as long as the LLL approximation is valid. That is because when the trapping potential is removed, the interaction energy scale goes to zero in the same way as the mean density decreases due to centrifugal effects. Also if a Feshbach resonance was used to increase interactions during preparation of the state, it can be utilised to switch off interactions at the time of release from the trap. This wavefunction microscope property is very important to enable optical resolution of the following observables.

### 3.3.3 Correlation functions

A quite simple observable is given in terms of the single particle density  $n(\mathbf{r})$ . Its definition is analogous to the bosonic case Equation (3.23), however it also features



a spin index  $\sigma$  for fermions.

$$n(\mathbf{r})^{(\sigma)} = \langle \Phi | \Psi_{\sigma}^{\dagger}(\mathbf{r}) \Psi_{\sigma}(\mathbf{r}) | \Phi \rangle \quad (3.55)$$

$$= \sum_{jk} \rho_{jk}^{(\sigma)} \phi_j^*(\mathbf{r}) \phi_k(\mathbf{r}) \quad (3.56)$$

$$\rho_{jk}^{(\sigma)} = \langle \Phi | c_{j,\sigma}^{\dagger} c_{k,\sigma} | \Phi \rangle \quad (3.57)$$

This density is shown in Figure 3.15 for both spin components. Because angular momentum is conserved, the distribution is rotationally symmetric and only the radial dependence is shown in the two upper panels. For the lowest value of  $L$ , the density starts out as a disk of constant density in the centre and a Gaussian falloff at larger radii as expected for the Fermi sea ground state. As the angular momentum increases, the edge gets smeared out while the central density remains constant. Only for the (1, 1, 1) state, the density again takes on a flat, disk like profile like the first state. In comparison to that state, the central density is lowered to approximately half the original value and the radius is increased. Overall, the density distribution does not change drastically for all but the very last state. In the presence of experimental noise, the difference among the different states would be hard to resolve. To reveal more of the states internal structure, the second order correlation function  $g^{(2)}$  is considered. This quantity is very characteristic for the Laughlin state which should also be true for the highly correlated (1, 1, 1) state. It is also experimentally accessible, either through imaging with single particle resolution or more indirect schemes like described in [PPC04]. The second order correlation for fermions features two spin indices for the two particles considered:

$$g_{\sigma,\sigma'}^{(2)}(\mathbf{r}, \mathbf{r}') = \frac{\langle \Phi | \Psi_{\sigma}^{\dagger}(\mathbf{r}) \Psi_{\sigma'}^{\dagger}(\mathbf{r}') \Psi_{\sigma'}(\mathbf{r}') \Psi_{\sigma}(\mathbf{r}) \rangle}{n^{(\sigma)}(\mathbf{r}) n^{(\sigma')}(\mathbf{r}')} \quad (3.58)$$

$$\langle \Phi | \Psi_{\sigma}^{\dagger}(\mathbf{r}) \Psi_{\sigma'}^{\dagger}(\mathbf{r}') \Psi_{\sigma'}(\mathbf{r}') \Psi_{\sigma}(\mathbf{r}) \rangle = \sum_{jklm} \rho_{jklm}^{(\sigma,\sigma')} \phi_j^*(\mathbf{r}) \phi_k^*(\mathbf{r}') \phi_l(\mathbf{r}') \phi_m(\mathbf{r}) \quad (3.59)$$

$$\rho_{jklm}^{(\sigma,\sigma')} = \langle \Phi | c_{j,\sigma}^{\dagger} c_{k,\sigma'}^{\dagger} c_{l,\sigma'} c_{m,\sigma} | \Phi \rangle \quad (3.60)$$

Because of symmetry between the two spin components, only two (equal and different spin) out of the four possible spin combinations are plotted in the following. In order to capture the four spatial dimensions of  $g^{(2)}$ , several special cases are considered. In Figure 3.16 the radial correlation is shown when the second particle is fixed to the origin. In this case,  $g^{(2)}(x, y)$  is rotationally symmetric for the first particle and possesses no angular dependence. For two particles of the same spin (left panel), the correlation function shows a node at zero distance because of the Pauli exclusion principle. This is also referred to as antibunching and it is present for all different angular momenta. In the case of two opposite spins (right panel), the behaviour is fundamentally different. For all groundstates in the sequence, except for the very last one, the correlation function remains constant over all distances at a value of one.

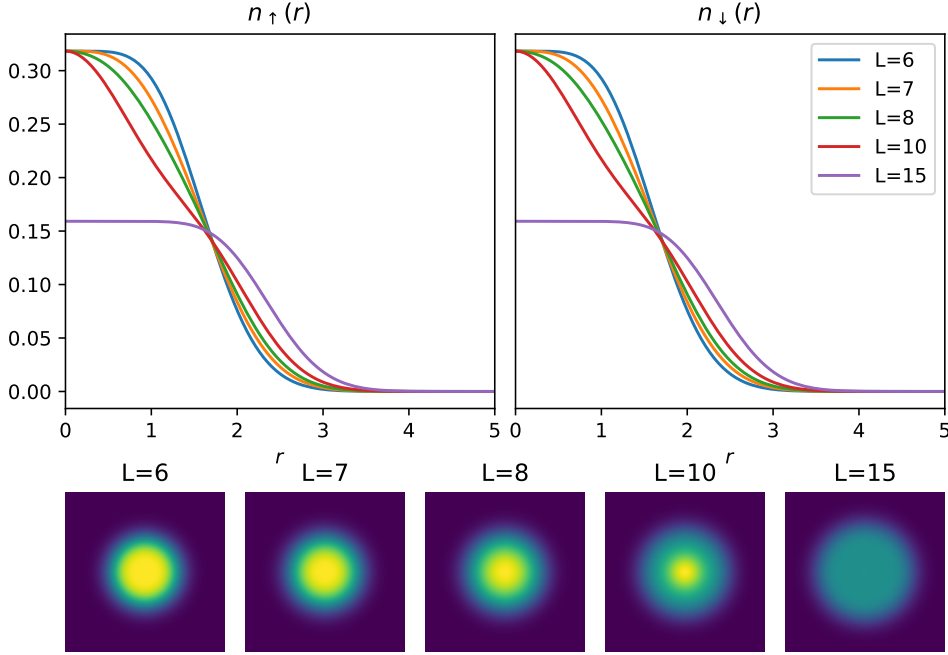


**Figure 3.15:** One particle density of the ground state for different angular momenta  $L$  for  $N_{\uparrow} = N_{\downarrow} = 3$  particles. The upper panels show equal density distributions for both spin components. Therefore only one spin component is shown in a 2D plot (lower panels), with angular momentum increasing from left to right.

This is expected for uncorrelated particles. Only the  $(1, 1, 1)$  state shows a clear node at zero distance, because the vortices  $(z_i - x_j)$  in the wavefunction Equation (3.48) prevent particles with different spins from approaching each other. In that regard, the correlation function for different spins is a good indicator to verify preparation of the  $(1, 1, 1)$  state. However only probing the radial dependence doesn't reveal structure for the intermediate states  $L = 7, 8, 10$ . For this rational symmetry of  $g^{(2)}$  has to be broken by fixing the second particle away from the origin. This is shown in Figure 3.17 In order to make the correlations of equal and different spins directly comparable, all representations of  $g_{\uparrow, \uparrow}^{(2)}$  are scaled by  $\frac{N}{N-1}$  to counteract a combinatorial factor. For two particles of the same spin  $g_{\uparrow, \uparrow}^{(2)}$ , the reduced correlation at the second particles position caused by Pauli blocking can be observed already for the first state  $L = 6$  and all subsequent ones. These vortices caused by the



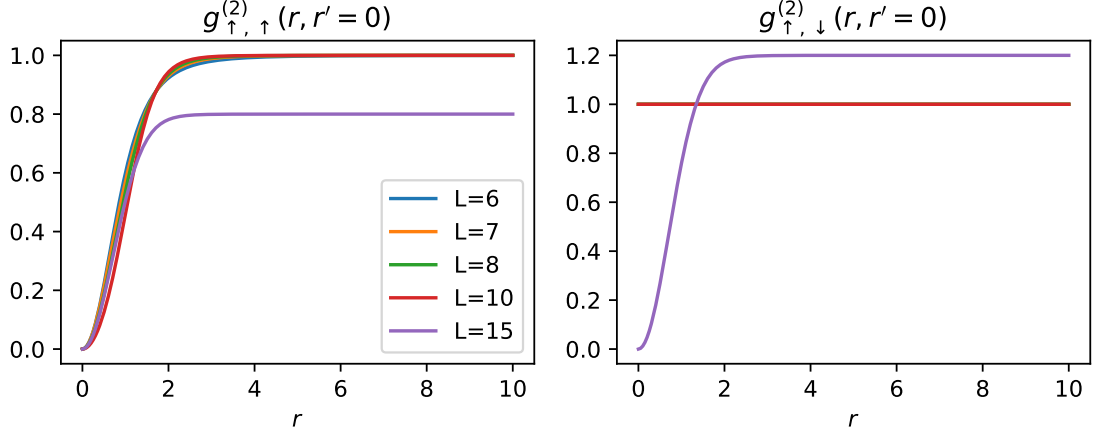


**Figure 3.16:** Two particle correlation function  $g_{\sigma, \sigma'}^{(2)}$ , for equal and different spins. Only the radial dependence for the first particle is depicted while the second one is fixed at the origin. Three atoms per spin component  $N_{\uparrow} = N_{\downarrow} = 3$  were used for this figure.

Vandermonde determinant Equation (2.31) manifest themselves as a hole at  $x' = 2$  in the two-dimensional plot  $g_{\uparrow, \uparrow}^{(2)}(x, y, x' = 2)$  and along the diagonal in  $g_{\uparrow, \uparrow}^{(2)}(x, x')$ . For two atoms of different spin, the effect of interactions by s-wave scattering is only weakly visible in  $g_{\uparrow, \downarrow}^{(2)}(x, x')$  at small distances. For states of increasing angular momentum  $L$ , stronger correlations for equal spins  $g_{\uparrow, \uparrow}^{(2)}(x, y, x' = 2)$  emerge, even though no direct interactions is present between them. Additional structure close to the origin of  $g_{\uparrow, \uparrow}^{(2)}(x, y, x' = 2)$  and along the anti-diagonals of  $g_{\uparrow, \downarrow}^{(2)}(x, x')$  emerges. This is also the case for atoms of unequal spin. In  $g_{\uparrow, \downarrow}^{(2)}(x, x')$  a suppression of correlation on the diagonal deepens for increasing angular momenta, until it resembles the same structure as the case of equal spins because of the vortices  $(z_i - x_j)$  in the  $\Psi_{(1,1,1)}$  wavefunction. For the two-dimensional plots  $g_{\uparrow, \downarrow}^{(2)}(x, y, x' = 2)$  the states at  $L = 6$  and  $L = 7$  correspond to one and two vortices between the centre-of-masses of both spin components, which can be related to the disk-shaped profile at the origin and the drop in correlations towards the second particle at  $x' = 2$ . Because the vortices only involve the centre-of-mass and not single particle coordinates, the value does not drop to zero like for the subsequent states. To explain the features of the state at  $L = 10$  and the additional states presented in Figure B.13 the corresponding wavefunctions have to be identified. Even when the wavefunction is computed as a polynomial as outlined in Equation (3.43), factorization into an insightful form is hard when no prior knowledge on the type of wavefunctions exists. More work has to be done to possibly relate the ground-states of each spin sector and their first excitations to states like the spin-charge separated state or the Haldane-Rezayi state

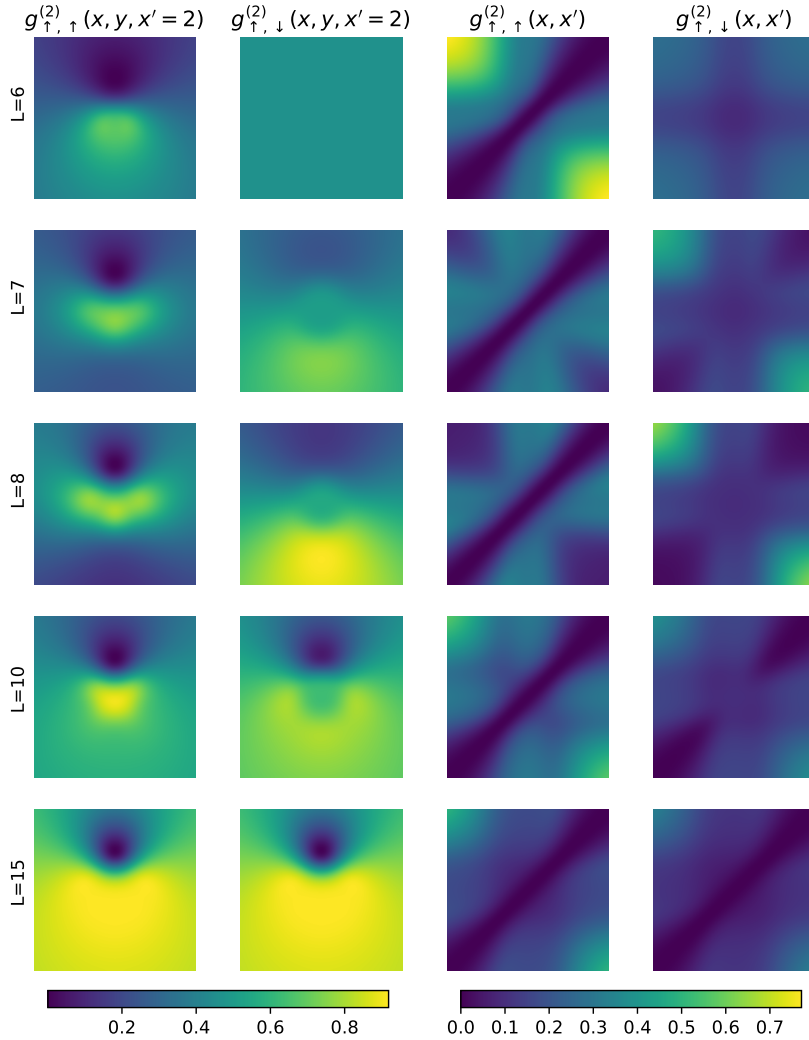


**Figure 3.17:** Two particle correlation function  $g_{\sigma, \sigma'}^{(2)}(\mathbf{r}, \mathbf{r}')$  for groundstates with different angular momenta  $L$  (rows). The two-dimensional dependence of the first particle is shown when the second one is fixed away from the origin ( $x' = 2$ ) for equal (first row) and opposite (second row) spins. Third and fourth column show the particles correlation as a function of both radii for equal (third row) and opposite (last row) spins. All plots in the first two and second two columns share the same colourbars (bottom). This plot was computed for  $N_{\uparrow} = N_{\downarrow} = 3$  particles.



predicted in [AR11]. First efforts into this direction have not been conclusive.

# Chapter 4

## Experimental Background

### 4.1 Scattering properties

In ultracold quantum gases, neutral atoms are only interacting with each other through collisions, as no Coulomb forces are present. This scattering is caused by an interaction potential  $V(\mathbf{r}_i - \mathbf{r}_j)$  which has the form of an isotropic Van-der-Waals for neutral atoms only depending on the distance  $r_{ij} = |\mathbf{r}_i - \mathbf{r}_j|$ . Because the density in a dilute sample of ultracold atoms is usually low, only the probability of finding two atoms inside of a radius  $r_0$  is not vanishing. This holds when the typical inter-particle distance  $n^{-1/3}$  is much larger than the potential range  $n^3 r_0 \gg 1$ . Only for very large scattering lengths higher order processes like three body losses can play a role. The binary scattering problem can then be described in terms of a Schrödinger equation in the relative coordinates. It is solved by the usual scattering ansatz

$$\Psi(\mathbf{r}) \propto e^{i\mathbf{k}\mathbf{r}} + f(\mathbf{k}, \mathbf{k}')e^{ikr} \quad (4.1)$$

where the prefactor  $f(\mathbf{k}, \mathbf{k}')$  describes the scattering amplitude. Because the problem is spherically symmetric, the amplitude can be decomposed into partial waves with different angular momenta  $l$

$$f(\theta) = \sum_{l=0}^{\infty} (2l+1) f_l P_l(\cos(\theta)). \quad (4.2)$$

The coefficients  $f_l$  can be written as

$$f_l = \frac{1}{k \cot \delta_l(k) - ik} \quad (4.3)$$

where  $\delta_l$  denotes the phase shift of the asymptotic wave-function after collision. The different partial wave orders  $l$  are often referred to as s-wave, d-wave, etc. for even  $l$  and p-wave, etc. odd  $l$  in analogy to angular momentum orbitals. For ultracold atoms, only s-wave scattering ( $l = 0$ ) is accessible because all higher contributions vanish in the limit  $k \rightarrow 0$  of low momenta yielding.

$$f_0 = -\frac{a}{1 - \frac{1}{2}k^2 r_e a + ika} \quad (4.4)$$



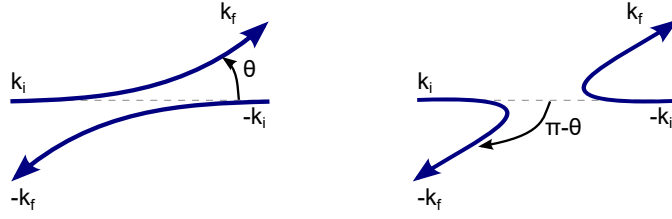


**Figure 4.1:** In the scattering of identical fermions, both paths lead to the same outcome. Because of a negative sign under particle exchange destructive interference suppresses s-wave scattering.

An additional constraint is imposed by the statistics of the colliding particles. For two fermions with equal spin resulting in a symmetric triplet state, the spatial wave-function is anti-symmetric leading to an odd value of  $l$ . Therefore equal spin fermions do not interact in the limit as s-wave scattering. This can be also seen in Figure 4.1 as both paths, that can't be distinguished, contribute with opposite sign  $f(\theta) - f(\pi - \theta)$  because of fermion statistics. Only through a p-wave Feshbach resonance scattering between equal spins can be introduced as demonstrated in [Zha+04]. In the limit of low momenta, the scattering process can be described by a single quantity, the s-wave scattering length

$$a = - \lim_{k \rightarrow 0} \frac{\tan \delta_0}{k} \quad (4.5)$$

in terms of the phase shift  $\delta_0$ . If there is no shift of the wave-function, the scattering length is zero. However as it approaches  $\pm\pi/2$ , the scattering length diverges. This happens when a bound state of the potential gets resonant with the continuum. Because the internal structure of the potential is not probed and only the asymptotic behaviour of the wave-function matters, the interaction can be represented by a pseudo potential

$$V_{int}(\mathbf{r}) = g_{3D} \delta(\mathbf{r}) = \frac{2\pi \hbar^2 a_{3D}}{m} \delta(\mathbf{r}) \quad (4.6)$$

comprising a delta function. The scattering length is set by the microscopic properties of the potential and the position of bound states in particular. These cannot be modified, but luckily there is another way to externally tune the scattering length and thereby the interaction strength. When the two atoms are approaching each other they experience a molecular potential asymptotically connected to the case of free atoms. Because ultracold collisions take place near zero energy, this potential is energetically accessible why it is referred to as the open channel. However both atoms can also form different molecular states whose potential curves are located at higher energies and are thus not accessible by the atoms. Therefore these are called closed channels and they also support a number of bound states. The spin configuration and thereby the magnetic moment of these closed channels is different

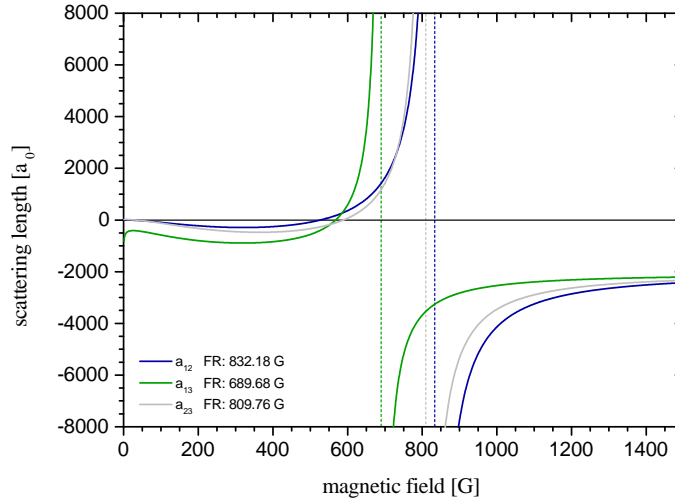


**Figure 4.2:** Feshbach resonances between the lowest three hyperfine states are present in  ${}^6\text{Li}$  at around 700 G-800 G. They allow tuning of the scattering length to positive and negative values.

than the one of the open channel, which allows their energy difference to be tuned via an external magnetic field. When the bound state of the closed channel is tuned into resonance with the incoming particles, they can virtually occupy this state for a certain time leading to a phase shift of the outgoing wave-function. This process is called a Feshbach resonance and allows tuning of the scattering length. An empirical formula quantifying this behaviour is given by [Chi+10]

$$a(B) = a_{bg} \left( 1 - \frac{\Delta B}{B - B_0} \right) \quad (4.7)$$

with the background scattering length  $a_{bg}$  and  $B_0$  and  $\Delta B$  the position and width of the resonance in terms of magnetic field. In Figure 4.2 the Feshbach resonances between the three lowest hyperfine levels  $|1\rangle$ ,  $|2\rangle$  and  $|3\rangle$  of  ${}^6\text{Li}$  are shown. All three combinations among these three states feature a broad Feshbach resonance (width of approx. 100 G) at around 700 G-800 G. With these, any two-component mixture can be tuned from non- to strongly interacting and both attractive and repulsive interactions are possible.

## 4.2 Preparation of an ultracold Fermi Gas

**Optical dipole trap** There are multiple ways to trap atoms in free space, e.g. Magnet Optical Traps (MOT). However not all of them allow cooling and confinement of the atoms below the recoil limit set by scattering of resonant photons. To circumvent this problem, magnetic traps acting on the atoms magnetic moment or



dipole traps acting on an induced dipole moment are used. Neutral atoms do not possess an intrinsic electric dipole moment. However in the presence of a strong electromagnetic field of a laser  $\mathbf{E}$ , an electric dipole moment  $\mathbf{p}$  is induced leading to a dipole potential  $V_d \propto -\mathbf{E} \cdot \mathbf{p}$ . The effective potential created by the laser field can be described in a semi-classical picture [GWO00] by

$$V_d(\mathbf{r}) = -\frac{3\pi c^2}{2\omega_0^3} \left( \frac{\Gamma}{\omega_0 - \omega} + \frac{\Gamma}{\omega_0 + \omega} \right) I(\mathbf{r}) \quad (4.8)$$

where  $\omega_0$  denotes the resonance frequency and  $\Gamma$  the line-width of the atomic transition,  $\omega$  the frequency and  $I(\mathbf{r})$  the intensity distribution of the driving laser field. This effect can equivalently be understood in a dressed state picture of a two-level atom. There the presence of a far red-detuned light field lowers the ground state energy leading to an attractive force, which is referred to as the AC-Stark shift. As apparent from Equation (4.8), there is a trade-off in choosing the detuning  $\Delta = \omega_0 - \omega$  of the trap. A larger detuning  $\Delta$  suppresses the photon scattering rate as  $\Gamma_{sc} \propto \Delta^{-2}$  while the potential depth decreases as  $V_d \propto \Delta^{-1}$ . Because of this difference in scaling it is advantageous to choose a rather large detuning to reduce scattering and counteract this by a large optical power. In the  ${}^6\text{Li}$  experiment a IPG photonics fibre laser (YLR-200-LP-WC) with a wavelength of  $\lambda \approx 1064\text{ nm}$  and power of 200 W is used leading to a detuning of  $\Delta \approx 400\text{ nm}$  to the D2 line. This method can be used to cool the atomic gas below the photon-recoil limit by evaporative cooling [Ser+11] and to trap and manipulate the system afterwards without introducing energy. Using this cooling technique temperatures of the order of 100 nK can be obtained.

**Deterministic preparation** To prepare a sample of few ( $\propto 10$ ) ultracold atoms from an initially large number of particles, a two stage process is used. First, an additional dipole trap with a much narrower waist (called *microtrap*) is superimposed on the original large dipole trap now acting as a reservoir. Using this so-called *dimple trick* [Ser11], the degeneracy of the Fermi gas can be greatly increased as shown in Figure 4.3. This ensures that all lowest lying states in the microtrap are occupied and no holes are present to a high probability. After this the large dipole trap is switched off removing the reservoir. In order to reduce the atom number in the microtrap even further, a spilling technique is used as it was demonstrated in [Ser+11] and is shown in Figure 4.4. In addition to the optical trapping potential a magnetic field gradient is applied along the long axis of the microtrap. This deforms the initially gaussian potential in a way that allows atoms down to a certain level to escape from the trap. This technique allows preparation of well-defined number of atoms with a fidelity well above 90%.

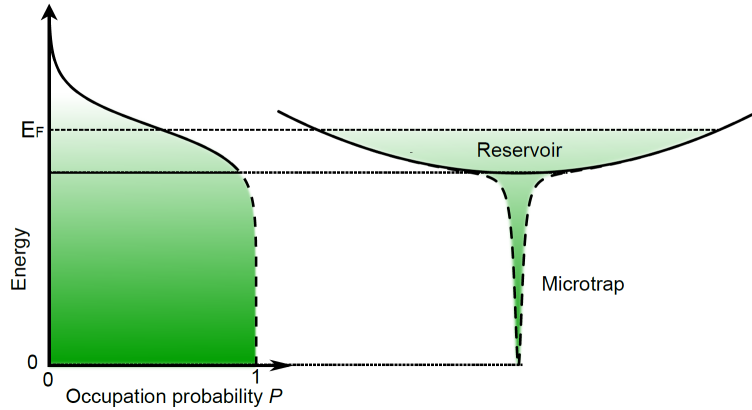


**Figure 4.3: Dimple trick** for preparation of a highly degenerate Fermi gas. A large optical dipole trap acting as a reservoir contains a Fermi gas at a temperature of 250 nK or  $T/T_F \approx 0.5$ . By overlapping a tightly focused microtrap the local Fermi energy can be increased leading to a lower temperature and increased degeneracy of  $T/T_F \approx 0.05$  and a very high occupation probability of the ground state of  $P_0 > 99.99\%$ . Figure taken from [Ber17].

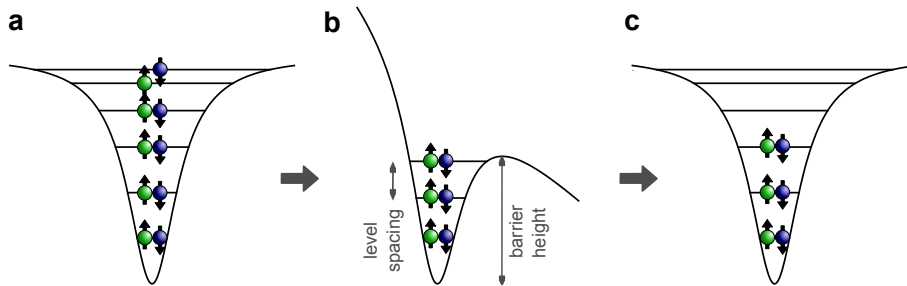


**Figure 4.4: Spilling technique** used to deterministically prepare a small number of atoms in the groundstate of the trap (c). A magnetic field gradient along the long axis of the optical microtrap deforms the confining potential (b). In this way all levels above a certain barrier height cleared. Figure taken from [Ber17].



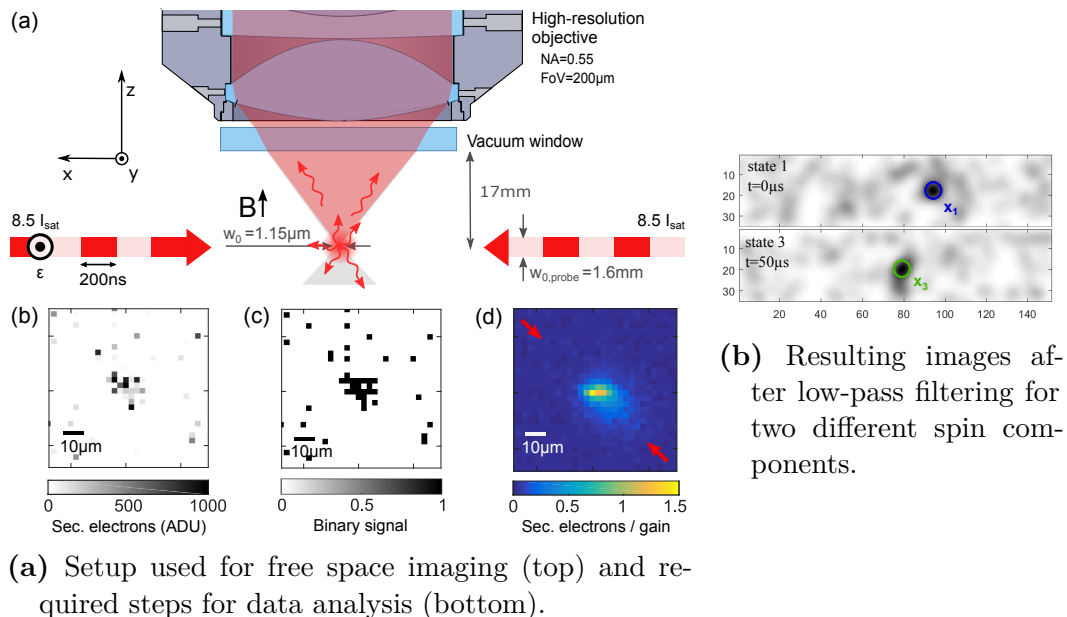
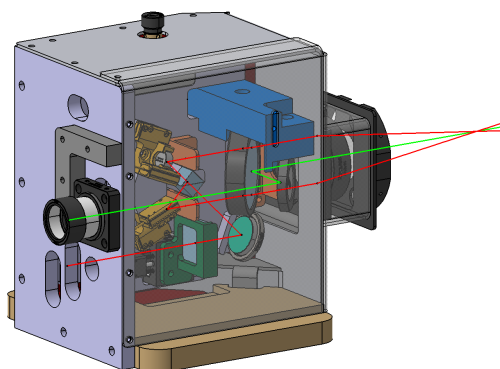


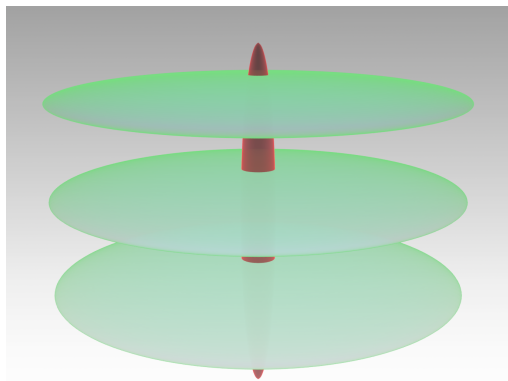
Figure 4.5: Overview of the single particle imaging method.

### 4.3 Single Particle Imaging Method

After performing experiments with the previously prepared sample of ultracold atoms, the state of the system has to be measured. There are various methods to resolve the density on a single-particle level [Quantum Gas Microscope]. In our experiment we employ a recently developed imaging scheme to image single atoms either in situ or after a time of flight. In this way we extract the spin-resolved real- or momentum space distribution of single atoms [Ber+18]. For this, resonant light is scattered off the atoms and collected using a high NA objective. An advantage of this imaging method is it not requiring any cooling scheme compared to quantum gas microscopes. Instead, atoms perform a random walk upon photon scattering leading to a spread on the order of  $\mu\text{m}$  that is not much larger than the imaging resolution itself. An overview over this method is given in Figure 4.5a. Because the different hyperfine levels  $|1\rangle$ ,  $|2\rangle$  and  $|3\rangle$  of  ${}^6\text{Li}$  experience a different Zeeman shift in the magnetic field, their transitions can be individually addressed by choosing the right laser frequency. In this way two spin components can be imaged separately on two different pictures, as shown in Figure 4.5b. As this imaging technique allows single particle localisation and spin readout with high fidelity, it is well suited for the detection of correlated quantum Hall states. As described in Section 3.3.2, a sample of the full wave-function can be obtained which enables extraction of higher order correlation functions.



(a) Technical drawing of the 2d dipole trap (red beams) with included MOT beam (green). Figure taken from [Pet16].



(b) Iso-surfaces of the 2d dipole trap intensity (blue). The red ellipse indicates the beam of the optical microtrap used for stirring in perpendicular direction.

**Figure 4.6:** Overview of the crossed beam 'pancake trap' confining the atoms to two spatial dimensions.

## 4.4 2D Confinement

The quantum hall physics described in Chapter 3 and described by the Hamiltonian Equation (3.1) only occur in two spatial dimensions (or higher multiples of two [PPZ18]). Therefore the atoms have to be confined in a way that makes the system effectively 2d. This is achieved by choosing a trap frequency  $\omega_z$  along the z-axis that is much larger than in the radial direction  $\omega_z \gg \omega_r$  so that only the ground state is populated in this direction. This can be expressed in terms of the aspect ratio  $R = \frac{\omega_z}{\omega_r}$  which should be on the order of  $\approx 100$ . In the experiment this will be realised using a standing wave dipole trap that was designed in [Pet16]. In Figure 4.6a a rendering of the trap construction is depicted. It works by interfering two beams obtained from a single input beam by a beam splitter under an angle of  $2\theta \approx 14^\circ$ . This configuration is chosen because optical access along the z-direction is already used by the imaging system. Indeed this small angle increases the spacing between interference maxima as  $d_z = \lambda/2 \sin(\theta)$  compared to a retro-reflected beam. The resulting optical potential is shown schematically in Figure 4.6b. The setup is designed in a way to yield a trapping frequency of  $\omega_z \approx 2\pi \times 30$  kHz along the axial and  $\omega_r \approx 2\pi \times 400$  Hz in the radial direction resulting in an aspect ratio of  $R \approx 70$ . For the creation of FQHE states an additional rotating microtrap (red ellipse in Figure 4.6b) will be superimposed.





# Chapter 5

## Experimental realization of a rotating optical trap

In order to realise rotating microtraps for artificial gauge fields as discussed in Chapter 3, an optical system has to be designed and built. Some attempts have been made in the past CITE to build a rotating optical trap using mechanical rotation. Here any vibrations directly translate to a trap modulation and consequentially heating. Therefore, an all-optical method has to be deployed to create such a rotating optical potential. The system must be able to achieve high frequencies of rotation on the same magnitude as the confinement, i.e. on the order of kHz. Furthermore, the strength  $\epsilon$  of the rotating perturbation must be precisely controlled in order to navigate through the energy landscape  $\Delta(\alpha, \epsilon)$  as presented in Figure 3.7 in an adiabatic way. The central idea to fulfil these requirements was first presented in [Fra+07]. It relies on two optical modes of different orbital angular momenta interfering with each other. Orbital angular momentum describes a change of phase in the optical field along the angular coordinate. The phase must be unambiguously defined, it is thus quantized to integer multiples of  $2\pi$ . A natural choice for beams with orbital angular momentum are Laguerre-Gaussian modes

$$u(r, \phi, z) = \frac{C_{lp}^{LG}}{w(z)} \left( \frac{r\sqrt{2}}{w(z)} \right)^{|l|} \exp\left(-\frac{r^2}{w^2(z)}\right) L_p^{|l|} \left( \frac{2r^2}{w^2(z)} \right) \times \quad (5.1)$$

$$\exp\left(-ik\frac{r^2}{2R(z)}\right) \exp(-il\phi) \exp(-ikz) \exp(i\psi(z)) , \quad (5.2)$$

where  $L_p^{|l|}$  are the generalized Legendre polynomials,  $C_{lp}^{LG}$  a normalisation constant (and parametrization is chosen in cylinder coordinates  $(r, \phi, z)$ ). The modes are parametrized by two integers  $l$  and  $p$  denoting the azimuthal and radial index. As one can see from the term  $\exp(-il\phi)$  a mode with index  $l$  carries an orbital angular momentum of  $l$ . The phase has a vortex in the centre (for  $l > 0$ ), the amplitude must thus vanish there, leading to a ring shaped intensity. The terms not featuring one of these indices are reminiscent of the Gaussian beam. When two modes of different  $l$  are overlapped, the intensity features an interference term with angular



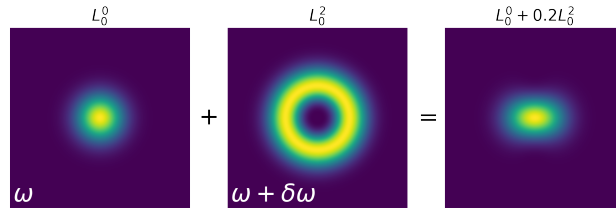


**Figure 5.1:** Interference of a Gaussian  $L_0^0$  and Laguerre-Gaussian  $L_0^2$  beam results in an elliptically shaped intensity. Detuning one of the modes by  $\delta\omega$  leads to a rotation around the origin.

dependence of the form  $\cos((l_1 - l_2)\phi)$ . This leads to an anisotropy of the resulting intensity distribution, like is shown in Figure 5.1 for  $l_1 = 0$  and  $l_2 = 2$ . If both modes have the same optical frequency and therefore a constant phase relationship over time, this interference is static. If, on the other hand, one of them is detuned in frequency by  $\delta\omega$  the difference in phase changes constantly and the pattern starts to rotate. When detuning the two beams by acousto optical modulators (AOM), the frequency of rotation and strength of the anisotropy can be precisely controlled by setting frequencies and amplitudes of the radio frequency driving the AOMs. The main steps in order to realise this scheme are therefore:

- generate two beams, each controlled in frequency and amplitude
- imprint a different optical mode onto each of them
- interfere them in the trapping plane in order to obtain a rotating potential

## 5.1 Spatial Light Modulation

To shape laser light into a particular optical mode, traditionally optical elements like wave-plates were used. A much more versatile tool to shape arbitrary distributions of light are available in terms of spatial light modulators nowadays. Their functional principle is shown in Figure 5.2 and further details are to be found in [Hol14]. They work like a liquid crystal display (LCD) where birefringent liquid crystals change their index of refraction as a function of orientation and thereby introduce a variable phase delay for a certain polarization of the incident light. A light modulator working in this way is called *phase-only*, in contrast to other existing technologies like digital mirror devices (DMD), which only modulate the light amplitude. However also a phase-only SLM allows control of phase *and* amplitude in the configuration shown in Figure 5.2. After the incoming collimated beam receives a phase modulation by the SLM, it is imaged by a lens into the Fourier plane. A thin lens acts like a Fourier

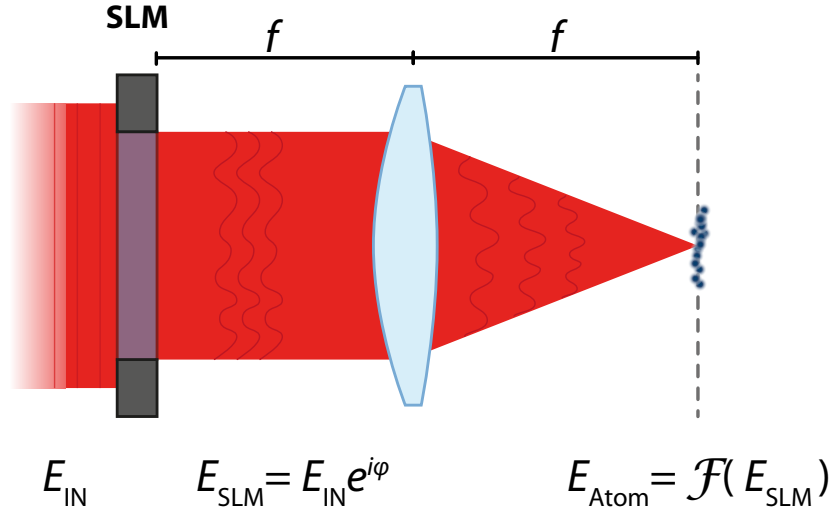


**Figure 5.2:** A Spatial light modulator (SLM) can be used to imprint a phase  $\varphi$  on the incident field. A thin lens in 2f-configuration results in a Fourier transform of the wavefront in the image plane  $E_{\text{atom}}$ . Figure adapted from [Hol17].

transform on the wavefront when placed in the shown 2f-configuration. Therefore, the intensity distribution in the Fourier plane is described by

$$I(\mathbf{r}) = |\mathbf{E}_{\text{fourier}}|^2 = \left| \mathcal{F}(\mathbf{E}_{\text{in}} e^{i\phi(x,y)}) \right|^2, \quad (5.3)$$

where  $\mathcal{F}$  denotes the Fourier transform and the incident field  $\mathbf{E}_{\text{in}}$  is assumed to have homogeneous amplitude. Because the resulting intensity and also phase depends in a non-linear way on the imprinted phase  $\phi(x, y)$ , it is possible to shape both of them. There is, however, a limitation to the amount of control in practice. Only a limited number of degrees of freedom are available to modulate the phase in the input plane and thus only a limited part of the output plane can be controlled in terms of amplitude and phase. In the remaining region control over the field has to be given up. There exist also different, more involved schemes that use multiple SLMs to control amplitude and phase either separately [Oka+11] or in an interferometric fashion [Shi+14]. The second possibility has been evaluated briefly since it greatly simplifies calculation of the required phase patterns.

### 5.1.1 Short revision of Fourier optics

The propagation of a monochromatic scalar light field can be described in paraxial approximation through Fraunhofer diffraction [KM01]. In the far-field the field can



be written as

$$u(x_0, y_0) \propto \int u(x_1, y_1) \exp\left(-\frac{2\pi i}{\lambda z}(x_0 x_1 + y_0 y_1)\right) dx_1 dy_1 \quad (5.4)$$

where  $\lambda$  denotes the wavelength and  $z$  the distance on the optical axis. The light propagation behaves just as the Fourier transform in this limit, only when short distances are considered additional factors for wavefront curvature have to be introduced. From this, some key properties of spatial light modulation, also called computer generate holograms (CGH) in the literature, can be derived analytically. When a linear gradient is added to the incident wavefront, this results in a linear displacement in the Fourier plane. One notes that the linear phase  $\phi(x) = \frac{2\pi x}{nd_{SLM}}$  results in an input field  $u(x) = e^{i\phi(x)}$ , where  $d_{SLM}$  is the size of an SLM pixel. Because the SLM can only add phases modulo  $2\pi$  the linear gradient becomes a sawtooth pattern with period  $n$ . When this wavefront is propagated to the Fourier plane (see Equation (5.4)) this results in a displacement

$$u(x') = \delta\left(\frac{1}{nd_{SLM}} - \frac{x'}{\lambda f}\right), \rightarrow x' = \frac{\lambda f}{nd_{SLM}}, \quad (5.5)$$

with  $f$  the focal length of the lens and  $\lambda$  the lights wavelength. From this the maximum angle of diffraction can be calculated, where the gradient period  $n$  has to be an integer number extending over several pixels. Otherwise the diffraction efficiency is drastically reduced, as explained in more detail in Section 5.1.2. With a pixel size of  $d_{SLM} = 12.5 \mu\text{m}$  and wavelength  $\lambda = 1.064 \mu\text{m}$  a maximum displacement of  $\approx 20 \text{ mrad}$  can be achieved for a period of  $n = 4$  pixel. The displacement  $x'$  can be expressed in a dimensionless quantity through dividing it by the size of the focal spot. This size also depends on the focal length of the lens and the beam diameter, which is determined by the SLMs aperture...

The phase pattern displayed on the SLM is not a continuous function, but sampled on a limited number of square pixels. This introduces additional structure into the diffraction pattern that has to be taken care of in order to obtain a smooth result. To see this, the total light field after the SLM  $t(x, y)$  can be decomposed into different contributions

$$t(x, y) = \text{rect}\left(\frac{x}{Md}, \frac{y}{Md}\right) \left(\text{rect}\left(\frac{x}{d}, \frac{y}{d}\right) \otimes q(x, y)\right), \quad (5.6)$$

where the two rectangle functions correspond to the square aperture with an edge length of  $M$  pixels and the size of the pixels  $d$  themselves. The individual pixels are convoluted by the actual phase pattern sampled on a a grid

$$q(x, y) = e^{i\phi(x, y)} \sum_{n, m=0}^{M-1} \delta(x - md, y - nd). \quad (5.7)$$

Again, the resulting image is obtained from the Fourier transform Equation (5.4). The convolution theorem relating products in real space to convolutions in Fourier space and vice versa greatly simplifies the integral yielding

$$T(u, v) = (A \otimes W)(u, v) \quad (5.8)$$

$$A(u, v) = M^2 d^2 \text{sinc}(Mdu, Mdv) \quad (5.9)$$

$$W(u, v) = d^2 \text{sinc}(du, dv) \mathcal{F}\left(e^{i\phi(x,y)}\right) \sum_{n,m=-\infty}^{\infty} \delta\left(u - \frac{m}{d}, v - \frac{n}{d}\right). \quad (5.10)$$

For a flat phase pattern the resulting intensity distribution  $T^2$  is depicted in Figure 5.3 where only one spatial dimension is shown for clarity. The first term  $A$  describes the sinc-shaped point spread function of the focus determined by the rectangular SLM window, which is shown in the lower figure. All spatial distances scale inversely under a Fourier transform, and thus the large aperture determines the smallest features in the image plane. The period of the Dirac comb in Equa-

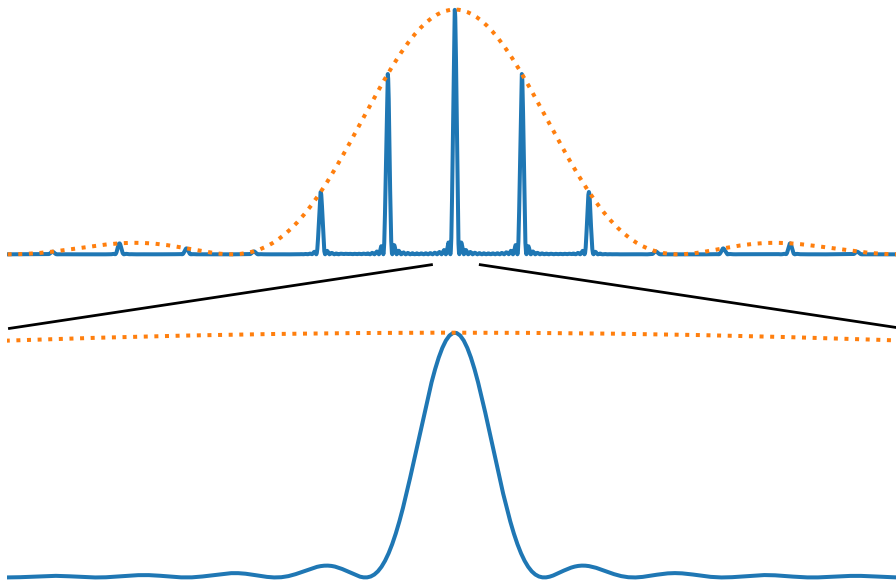


**Figure 5.3:** Far field intensity distribution when no phase pattern is displayed on the SLM. Sampling of the phase on pixels causes additional diffraction orders on large scales (upper panels) while the rectangular window gives a sinc-shaped point spread function (lower panel).

tion (5.7) is just rescaled by  $d^{-2}$  in the Fourier transform  $W$  leading to a number of higher diffraction orders with a distance  $S = \lambda f/d$ . For a typical focal length  $f = 200$  mm this equates to  $S = 1.7$  cm. These higher orders are suppressed by an envelope function (orange dashed line) stemming from the rectangular pixel shape. Not included in this model is an additional contribution from light experiencing



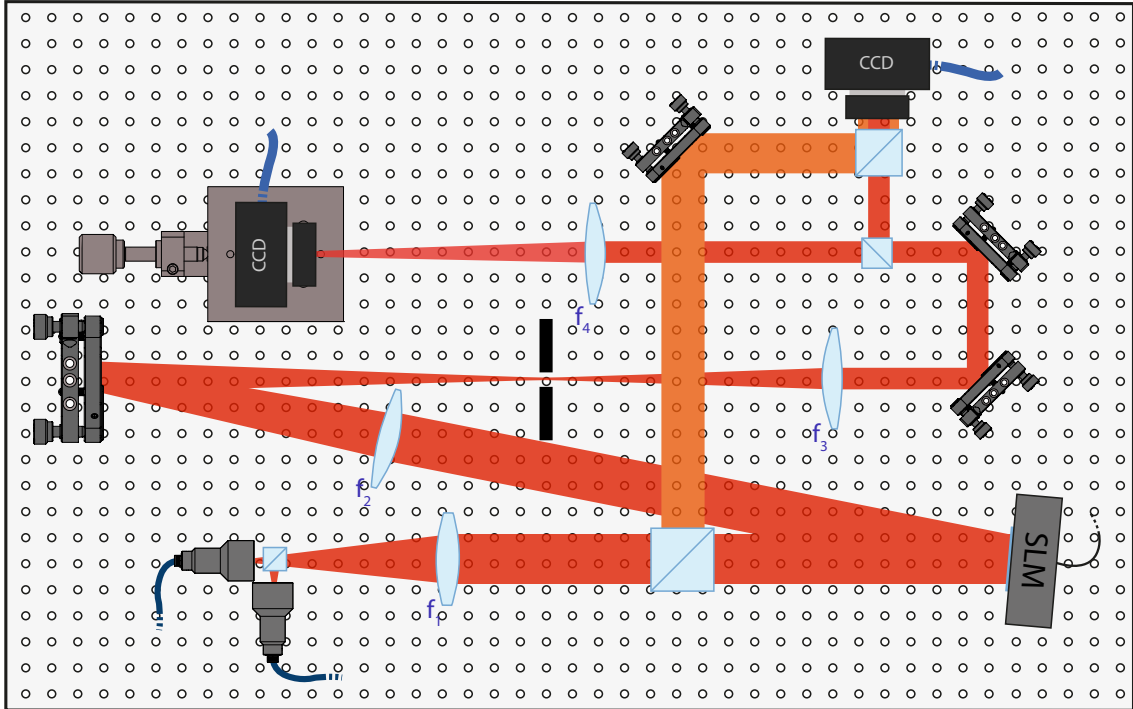


**Figure 5.4:** Schematic drawing of the optical setup used to create rotating optical traps. The two beams leaving the optical fibres are prepared in a different setup not shown here. In orange, the reference arm of the interferometer for measurements of the phase is indicated, the difference in colour does not denote a different frequency. All components are explained in detail in the text.

no modulation by the SLM. This light is also called zeroth order and its a result from the pixels not covering the entire surface. This fraction of un-diffracted light cannot be controlled but it interferes with the desired field giving rise to unwanted interference fringes. The only way to avoid this is to filter out the zeroth order by a mask and displace the desired first diffraction order away from this. Hence a spatial filter in an intermediate image plane is necessary to suppress all but the first diffraction orders. The optical setup for two beams is sketched in fig. 5.4. Not shown in the Figure is another small optical breadboard containing a beam-splitter and two AOMs for preparing two coherent beams with a frequency detuning on the order of kHz from a single laser. From there the beams are transported to the main setup using two short optical fibres. This allows for more flexible collimation geometries and provides sufficient interferometric stability. Initially both beams are diverging from the fibre core and are collimated by a single lens  $f_1$ . In the course of this they are overlapped under a small angle through a beam-splitter cube. This additional element is necessary as the spatial distance of both fibre tips could not be decreased

far enough because of the surrounding connector. In a final version this could be circumvented by keeping only the ferrule of the fibres and securing them in a special mount. Afterwards both beams are reflected by the SLM resulting in the desired phase modulation. The first lens  $f_2$  focuses the collimated beam down to a diffraction limited focus in the Fourier plane. There a pinhole is located that blocks the zeroth and other undesired diffraction orders. The relay telescope formed by  $f_3$  and  $f_4$  images the first diffraction order onto a camera while reducing the beam diameter. An additional interferometer is integrated into the setup to enable measurements of the lights phase after modulation. To this extent a reference wavefront is split off before the SLM as indicated in light orange.

### 5.1.2 SLM characterization

The SLM used for the optical setup in this thesis is a X10468-03 Liquid Crystal on Silicon (LCoS) SLM by Hamamatsu. It features 792x600 pixels that can each perform a phase shift from 0 to  $2.3\pi$  where the exact maximal value depends on the used wavelength. This particular model is optimized for a wavelength of 1064 nm and has a high light utilisation efficiency of up to 95% because of its little dead space between the pixels. Each pixel can be set to an 8 bit grey value between 0 and 255 corresponding to a phase in the full range. Because phases are usually defined modulo  $2\pi$ , all displayed phase patterns have to be scaled into this range by choosing an appropriate upper integer grey value corresponding to  $2\pi$ . This value is therefore also referred to as  $2\pi$ -value and is specified by the manufacturer to 216 for the wavelength used. In order to verify this value, different phase patterns are displayed while varying the  $2\pi$ -value from 0 to 255. The resulting scalar light field can be written as  $u(x) = \exp(ia\phi(x))$  where  $a$  denotes the modulation depth. In the far field, the different diffraction orders intensities  $I_n$  can be identified as the components of the Fourier series

$$u(x) = e^{ia\phi(x)} = \sum_n C_n e^{ik_n x}, \quad I_n = |C_n|^2. \quad (5.11)$$

For a binary grating described by a square wave  $\phi(x) = \text{square}(x)$  these can be calculated as

$$I_{\{0,\dots,3\}} = \left\{ \cos^2(a), \frac{4 \sin^2(a)}{\pi^2}, 0, \frac{4 \sin^2(a)}{9\pi^2} \right\}. \quad (5.12)$$

In comparison a sine-shaped phase  $\phi(x) = \sin(x)$  leads to intensities  $I_n = |J_n(a)|^2$  in terms of the Bessel functions  $J_n$  of the first kind. For these two phase patterns the positive and negative orders have equal intensity  $I_n = I_{-n}$  because of their symmetry. This is different in case of a linear gradient  $\phi(x) = x$  equivalent to a sawtooth wave when the phase is wrapped around  $2\pi$ . Here the different diffraction orders scale as

$$I_n = \frac{\sin(a)^2}{(a - n\pi)^2}. \quad (5.13)$$



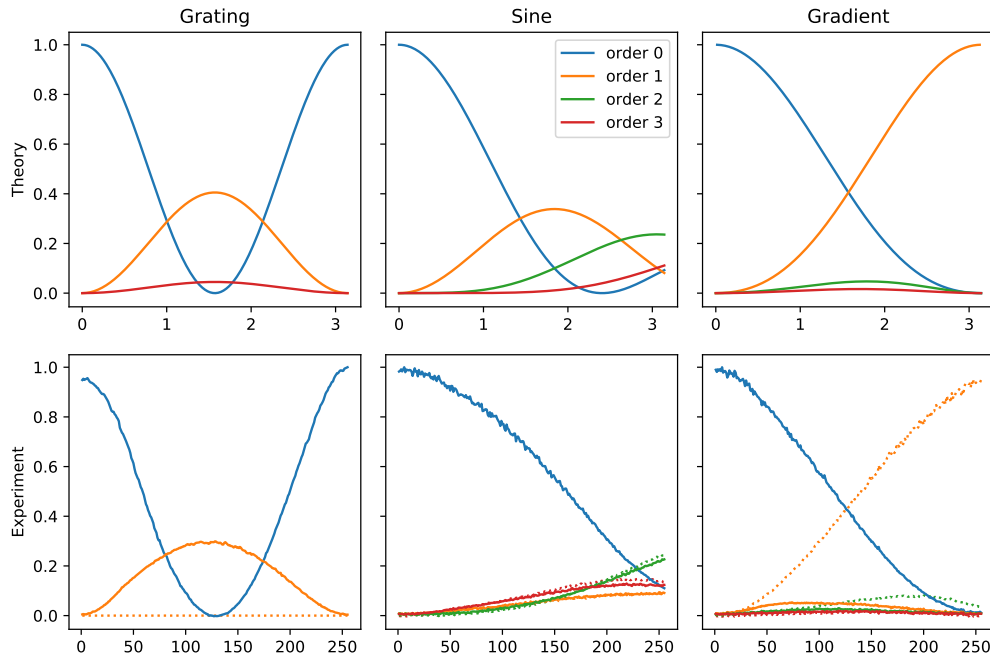


**Figure 5.5:** Intensities of different diffraction orders  $I_n$  as a function of modulation depth  $a$ . The latter is given in units of  $rad$  for the theoretical predictions and 8 bit grey values for the measurements. Three different phase patterns are shown (columns), a binary grating, sine and linear gradient.

The intensities are now different for positive and negative orders as the gradient acts like a blazed grating. For a particular modulation depth  $a$  the intensity of the first positive order  $I_1$  is maximized while being minimal for all others. This behaviour is wanted when displacing beams in order to achieve a high light utilisation efficiency. In Figure 5.5 these theoretical values are shown alongside experimentally obtained intensities for the different diffraction orders as a value of the modulation depth  $a$ . The figure shows good qualitative agreement between theory and measurements, only in the case of the sine pattern significant deviations are apparent for all diffraction orders. These measurements were obtained by taking an image of the far field intensity distribution for every modulation depth. Unfortunately the laser power was not stabilized during the measurements and fluctuations thereof pose the largest source of error. Therefore, no quantitative conclusions can be made. However, the different dependence of the Fourier components on  $a$  for the binary grating and sine pattern can give some insight into what is called crosstalk. When two neighbouring pixels are set to distinct phase values, the orientation of the liquid crystal layer is expected to smooth out the resulting phase distribution. To investigate this, a binary grating with a very short period of only few pixels is displayed. When a

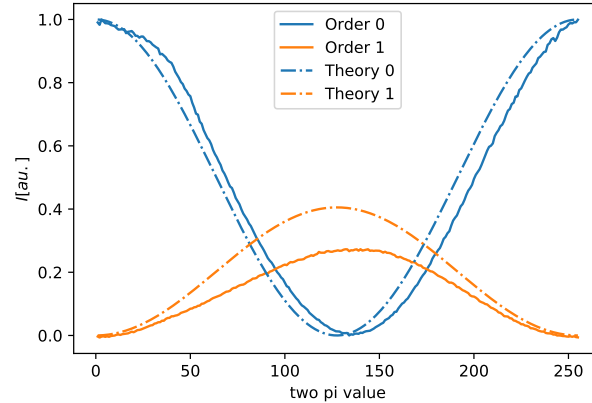


**Figure 5.6:** Intensity of the zeroth and first diffraction order as a function of modulation depth for a binary grating with a period of two pixel.

lot of crosstalk is present, one would expect the grating to be washed out into a more sine shaped pattern. In Figure 5.6 a measurement of the resulting diffraction intensities is shown. When compared to Figure 5.5, the behaviour of the zeroth and first diffraction order resemble the theoretical prediction of the grating case closer than the sine. However both measured curves are shifted to the right compared to the theory curve of the grating. This indicates that some crosstalk at a period of two pixels is present. A measurement for a spacing of only one pixel could not be performed as this resulted in the first diffraction order being off camera. When a non-binary phase pattern like a linear gradient is displayed on the SLM, sampling can become an issue. If a small period of the pattern is chosen to achieve large diffraction angles, the continuous phase is represented by only a small number of discrete levels. This leads to a reduced diffraction efficiency that can be calculated as [KM01]

$$\eta_m^N = \left( \frac{\sin\left(\frac{m\pi}{N}\right)}{\frac{m\pi}{N}} \right)^2, \quad (5.14)$$

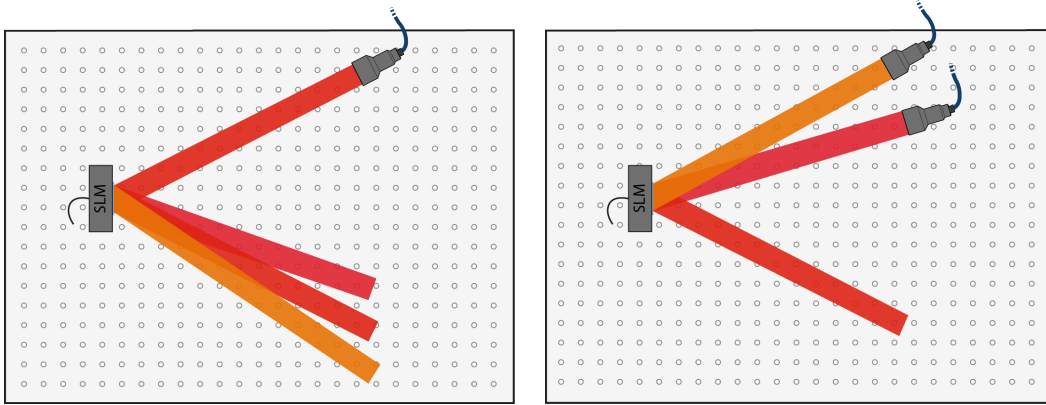
where  $N$  denotes the number of levels and  $m$  the diffraction order.

### 5.1.3 Analytic beam shaping

As calculated in Equation (5.5), a linear phase gradient can be used in order to displace the incident beam. There are several other analytical phase patterns for which the resulting light field is known. Of special importance are the quadratic phase

$$\phi(x, y) = \frac{1}{f}(x^2 + y^2) \quad (5.15)$$





- (a) By displaying a superposition of multiple gradients, a number of diffracted beams can be derived from a single one.
- (b) This also works in reversed order where two different incident beams can be made overlapping. Other side orders like in (a) are also present but not shown for clarity.

**Figure 5.7:** Multiple optical modes can be created or overlapped with a single SLM. This is used to imprint different wavefronts on two beams that are co-propagating afterwards.

acting as a thin lens of focal length  $f$  and the phase vortex

$$\phi(r, \theta) = l\phi = l \arctan(y, x). \quad (5.16)$$

This creates a Laguerre-Gaussian beam with angular momentum  $l$  as shown in Figure 5.1. From these a number of intensity distributions can be easily derived. When a number of phase patterns is summed together, where the resulting phase is taken modulo  $2\pi$ , their effects just add up. However is also possible to display a superposition of the from

$$\phi_{total} = \arg \left( e^{i\phi_1} + e^{i\phi_2} + e^{i\phi_3} + \dots \right), \quad (5.17)$$

where  $\arg$  denotes the argument. It is worth noting that this is different from the case where all exponentials are just multiplied. This would represent their concatenation yielding  $\phi_{total} = \phi_1 + \phi_2 + \dots$  like described above. When multiple gradients of different pitch are combined in this fashion, several beams are being diffracted. This situation is sketched in Figure 5.7 (a). The same technique can be employed to overlap two beams coming from different sources, which is shown in (b). Again two gradients are displayed with the period chosen in a way that aligns one diffraction order of each beam on top the other one. Of course there are two side diffraction order which are not overlapping nor shown in the figure. They can easily be blocked by a spatial filter but about 50% of light intensity is lost in this way. However, this is the only way to overlap the beams coming from

two different sources along their whole length of propagation while having the same polarisation. This ensures interference not only in a limited spot but over a large distance needed for a cylindrical lattice. As explained above, a detuning between the different optical modes is needed in order to make the trap rotate in time. The two sources in Figure 5.7 are therefore derived by two acousto optical modulators (AOM) from one common input beam. Each AOM offsets the frequency by the RF frequency  $\omega = 2\pi \times 110$  MHz used for driving. One of them is set to a slightly different frequency  $\omega + \delta\omega$  resulting in a rotation of the interference pattern at exactly  $\delta\omega$ . At the same time the AOMs allow for precise control of the beams amplitude by setting the amplitudes of the driving field accordingly.

#### 5.1.4 Algorithm for arbitrary amplitude and phase

When expanding the intensity and correspondingly potential depth  $V(r)$  of a Gaussian beam in a Taylor series

$$V(r) = V_0 \exp\left(-\frac{2r^2}{\omega^2}\right) = V_0 \left(1 - \frac{2r^2}{\omega^2} + \frac{2r^4}{\omega^4} + \mathcal{O}(r^6)\right), \quad (5.18)$$

where only the radial coordinate  $r$  is considered and  $\omega$  denotes the beam waist, one can observe that the contribution of order  $r^4$  has a positive sign associated with anti-confinement. Therefore an atom trapped in this potential experiences a smaller trapping force for larger  $r$  compared to the purely harmonic potential. This is especially bad for a rotating trap as the potential gets very shallow at large rates of rotation and any deconfining terms can lead to the loss of atoms. A more fine-grained control over the optical modes used for trapping is therefore desirable. For other experiments trapping geometries like a flat-bottom potential that are hardly attainable through analytic modes are interesting. For this a method to create arbitrary light fields in the trapping plane is required. With the employed SLM setup only the phase of the light in the input plane can be modulated and not its amplitude. Therefore, the mapping to intensity in the image plane given by Equation (5.3) is not invertible because of the absolute square. Instead an iterative algorithm has to be used in order to obtain the phase pattern yielding a desired target intensity. Several of these algorithms like IFTA and MRAF were devised in the past, which [Hol14] and [Bij13] describe in further detail. These are semi-heuristic algorithms that rely on alternating between real and Fourier space while enforcing the target intensity as a constraint in the Fourier domain. Another class of algorithms uses gradient descent in order to minimize some distance between the intensity resulting from a particular phase pattern and target intensity. This is expressed through a loss (sometimes also called cost) function

$$\mathcal{L} = \sqrt{\sum_{x,y} |I(\phi(x,y)) - I_{target}|^2}, \quad (5.19)$$



where the  $L_2$  norm is a specific choice minimizing RMS error. From this loss function a gradient  $\nabla_{\Psi}\mathcal{L}$  with respect to the input phase  $\phi(x, y)$  can be derived by means of the chain rule. When only a target intensity is desired, this is still tractable analytically as it was carried out in [Har+14]. All of the algorithms listed above produce an uncontrolled phase in the trapping plane. Usually this is not a problem as the dipole potential Equation (4.8) only depends on the lights intensity. However, for the creation of moving traps by interference, not only the intensity but also the phase in the trapping plane has to be controlled. This can be achieved by defining an appropriate loss function

$$\mathcal{L} = \left[ 1 - \sum_{i,j} \sqrt{I_{i,j}T_{i,j}} \cos(\Phi_{i,j} - \varphi_{i,j}) \right]^2, \quad (5.20)$$

incorporating an additional target phase  $\Phi_{i,j}$ . It calculates the overlap or fidelity in terms of intensity and phase being written in a way  $\mathcal{L} = (1 - \mathcal{F})^2$  that is minimized for  $\mathcal{F} \rightarrow 1$ . The computation of this loss functions gradient, however, becomes analytically intractable which is why an automatic differentiation framework is used. It contains the corresponding derivatives for all arithmetic operations involved and can therefore work out the total gradient by applying the chain rule. All necessary steps for computing the phase pattern resulting in the desired light field are summarized in Algorithm 1. The algorithm takes the incident and target light field as well as a mask for the region of interest as an input. Subsequently the optimization start by applying an initial phase guess  $\phi_0$  to the incident field and propagating it to the output plane. In order to fulfil the Nyquist sampling theorem an additional zero-padding around the phase pattern has to added before and removed after propagation to the image plane. In the Fourier plane the distance between output and target field is evaluated in terms of the cost function Equation (5.20). From this also the gradient can be computed which is used to bring the phase pattern  $\phi$  closer to an optimum. These steps are iterated until the loss reaches a specified lower threshold or a maximum number of iterations is reached. As the computational cost for calculating  $\mathcal{L}$  and its gradient becomes significant when a number of optimization steps is performed, an acceleration by GPU computing is desirable. Otherwise the optimization time is on the order of 5 min when executed only on a CPU. Therefore an *NVIDIA* GeForce GTX 1080 GPU was used, decreasing the typical optimization time to approximately 30 s. Instead of manually implementing all algorithms necessary for propagation and optimization on the GPU itself, the *Tensorflow* [Aba+16] framework was used to build a computational graph. This could be natively executed on the GPU without resorting to a specialized programming language like CUDA. This framework is a perfect fit for the task at hand because it features automatic differentiation also for advanced functions like the 2D Fourier transform. It also handles complex variables and their gradients naturally, contrary to other frameworks like Theano. Instead of the very simple update step denoted in Algorithm 1,

**Algorithm 1** Gradient descent algorithm for phase calculation**Require:**Step size  $\alpha$ Incident laser field  $E_{laser} = \sqrt{I_{laser}} \exp(\varphi_{laser})$ Target light field  $\tau = \sqrt{T} \exp(\Phi)$ Initial phase guess  $\phi^{(0)}$ 

- 1: **while**  $\mathcal{L} > \mathcal{L}_s$  and  $N_{iter} < N_{max}$  **do**
- 2:      $E_{in} \leftarrow E_{laser} \exp(\phi)$  ▷ Apply phase pattern
- 3:      $E_{out} \leftarrow \mathcal{F}[E_{in}]$  ▷ Propagate to output plane
- 4:      $I \leftarrow |E_{out}|^2, \varphi \leftarrow \arg(E_{out})$
- 5:      $\mathcal{L} = \left[1 - \sum_{i,j} \sqrt{I_{i,j} T_{i,j}} \cos(\Phi_{i,j} - \varphi_{i,j})\right]^2$  ▷ Compute loss function
- 6:      $\phi \leftarrow \phi - \alpha \nabla_{\phi} \mathcal{L}$  ▷ Update phase with gradient

a number of more involved gradient descent methods like conjugate gradient can be used. They are tailored to specific mathematical properties of the function to optimize and can lead to faster convergence. For the implementation in this thesis a method called ADAM [KB14] was chosen. It was developed in the context of machine learning, outperforms several other methods (see reference) and was already implemented in *Tensorflow*. The particular details of this algorithm are not important here and a learning rate of  $\alpha = 0.5$  was found to give good convergence for all target distributions. In Figure 5.8 the evolution of the loss, fidelity and efficiency is shown as a function of iteration number for the ring target shown in Figure 5.16. The efficiency is defined as the fraction of light intensity inside the masked region compared to the total intensity. Initially, the fidelity increases rapidly to a value close to unity while at the same time the efficiency drops down to about 20%. This is because in order to set both intensity and phase in the target region, the algorithm has to give up control over the field outside of this region and a substantial amount of diffracted light ends up there. For more complex pattern like Figure 5.18 the light utilisation efficiency can drop below 10%. Some examples of arbitrary light fields obtainable using this algorithm are depicted in Section 5.3. A measurement of the resulting intensity can be easily obtained by taking an image on a camera. This is not as straight forward for the resulting phase of the diffracted light. In order to measure the latter an interferometric measurement using a flat reference wavefront has to be used. For that reason a Mach–Zehnder type interferometer was built into the optical setup that is indicated as orange in Figure 5.4. The resulting image shows a number of interference fringes whose exact shape encodes the desired phase information. Recovering only the wavefronts phase separate from the carrier given by the fringes between two flat wavefronts is not a trivial task. A class of techniques [TIK82], [BBS86], [ZW10] relies on the spacing of both components in frequency space employing a Fourier transform. In frequency space the relevant



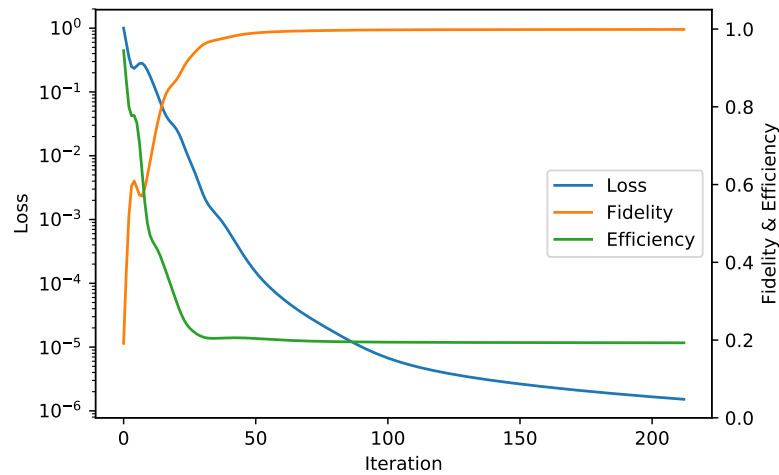


**Figure 5.8:** Loss, fidelity and efficiency as a function of iteration number during optimization of an arbitrary target field.

component has to be cut out and shifted to the origin followed by a backwards transform. Although this method works in principle, it requires manual tuning of certain parameters and is not very robust. Instead an algorithm called phase shift interferometry [Bru+74] is used because it is robust and does not require manual adjustment. It will be described in the following section (see Equation (5.23) and Figure 5.12) in greater detail. The resulting phase measurements obtained in this fashion are displayed in Section 5.3.

## 5.2 Optical aberration correction

Every optical setup suffers from aberrations introduced by inexact alignment of its optical components or imperfections of the elements themselves like spherical lenses. This degrades the optical performance below the diffraction limit and introduces unwanted disturbances to the point spread function. For an optical micro trap this is especially unfavourable as these introduce additional anharmonic perturbations. To quantify aberrations in an optical system so called Zernike polynomials are employed. These are obtained as the eigenmodes of a circular aperture described by the unit disk. Thereby they represent common optical errors like tilt of an element or spherical aberrations of an imperfect lens. This makes them useful to gain some insight about the causes responsible for non-optimal performance. In Figure 5.9 the first 15 Zernike polynomials for a rectangular aperture are depicted. These were obtained in [Mah12] by cutting them from the unit disk and orthogonalising subsequently. The first three terms describe a total phase offset and tilt in the x- and y-direction.

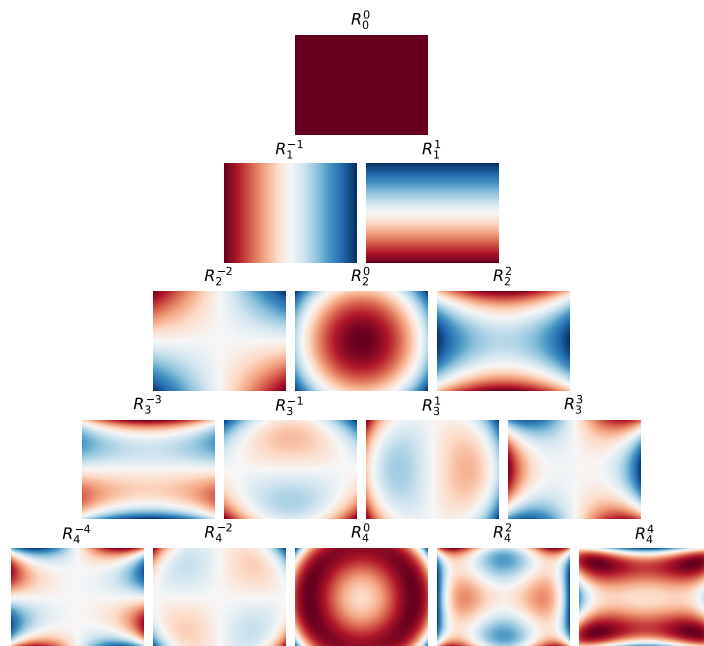


**Figure 5.9:** Zernike polynomials defined for a rectangular aperture. The different orders describe optical aberrations like tilt, astigmatism, defocus and coma.



They do not influence the quality of the focus. However, the higher-order polynomials with upper index zero describe a defocus and spherical aberrations which are present frequently and severely distort the point spread function. As the Zernike polynomials form a complete set, every wavefront  $W$  can be decomposed into a linear combination of the form

$$W(x, y) = \sum_{i=1}^L a_i R_i(x, y) \quad (5.21)$$

with coefficients  $a_i$ . In order to fit these to a real wavefront, the phase is measured at  $N$  discrete data points  $W(x_n, y_n)$ ,  $n = 1, \dots, N$ . All data points are arranged in a  $N \times 1$  matrix and the coefficients  $a$  are obtained from a least squares fit inverting  $Ra = W$  where  $R$  is the matrix containing  $N \times L$  Zernike coefficients. When these aberrations can be measured, the SLM itself can be used to display a correction pattern and thereby cancel all aberrations present in the system. In order to do this a phase map of the wavefront must be obtained. A variety of methods that often originate from telescope manufacturing exist. One group of these are *Shack-Hartmann*-type methods. They rely on the angular deflection of one or multiple probe beams by a local tilt of the wavefront in order to obtain a distortion map of the whole wavefront. More details on the Shack-Hartmann algorithm can be found in [Hol14]. It is well suited to measure large optical aberrations, however for local phase deviations below  $1\lambda$  the shift of the probe beams focus gets hard to measure reliably. Therefore two interferometric methods were implemented and used in this thesis. They provide phase information about a beam by interfering it with a reference beam of known phase. Two types of techniques for extracting the phase information can be distinguished as spatial and temporal methods. Spatial algorithms work with one interference pattern as seen in Figure 5.11 and strive to separate the phase  $\Delta\phi$  from its spatial carrier  $\sin(\alpha)x$  (as in Equation (5.22)) in the frequency domain [TIK82]. This method is not well suited in the present case as only very few interference fringes are visible due to the beams envelope. Consequently, this leads to a large spread in the frequency domain which prevents good separation. Instead, a temporal method is employed that relies on taking multiple interferograms at different phase shifts of the reference beam. It is known as *Phase shift interferometry* (PSI) in the literature [Bru+74] and allows a precise measurement of aberrations down to  $0.1\lambda$ . Its principle of operation is shown in Figure 5.10. Two beams are used whereas one serves as a reference and the other one as the probe. When overlapping in the focus their interference pattern is visible in the intensity and the exact position of the peaks is determined by their relative phase  $\Delta\phi$ . Because the reference beam is always on the optical axis this phase difference represents all wavefront errors picked up in the optical system by the probe beam. The interference patterns intensity in the focal plane can be derived as

$$I(x, y) = I_r + I_p + 2\sqrt{I_r I_p} \cos(\sin(\alpha)x + \sin(\beta)y + \Delta\phi), \quad (5.22)$$

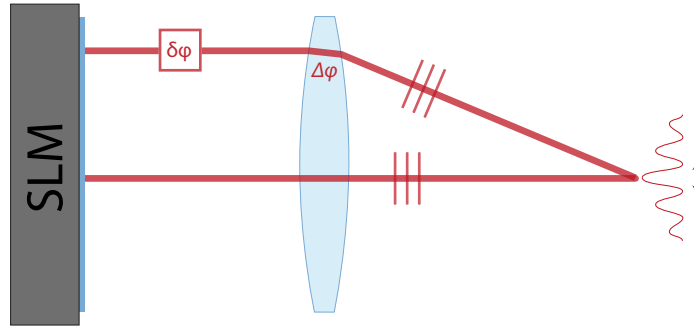


**Figure 5.10:** Simplified scheme of the phase shift interferometry used to measure optical aberrations. A beam on the optical axis serves as a reference, while a second moving beam probes the aberrations of the optical system. Phase errors on the wavefront are indicated by  $\Delta\varphi$  in the lens and give rise to a shift of the interference pattern. To perform phase shift interferometry, an additional phase offset  $\delta\varphi$  can be introduced by the SLM.

with  $I_r$  and  $I_p$  the intensity of the reference- and probe-beam and  $\alpha$  and  $\beta$  the relative angles between both. As the probe beams position is varied on the SLM plane, both of these angles and consequently the spacing of the fringes changes. In the left panel of Figure 5.11 this intensity is shown for one particular position of the probe beam. In principle the displacement of the central peak is proportional the the phase difference  $\Delta\phi$ . However a fit of the whole interference pattern is not reliable enough to extract this position. Therefore an additional phase shift  $\delta\phi$  is introduced into the probe beam by the SLM as indicated in Figure 5.10. When this

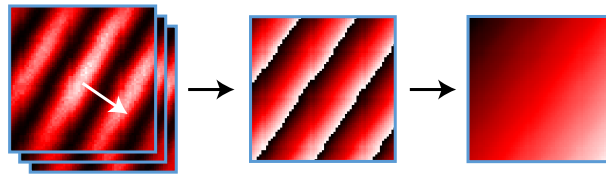


**Figure 5.11:** Steps involved in phase shift interferometry at one spatial position of the probe beam. Interference pattern for different offset phases  $\delta\varphi$  are merged into a single phase map by Equation (5.23), that has to be unwrapped afterwards to give the local phase  $\Delta\varphi(x, y)$ .

is done for a number of equally spaced phase shifts  $\delta\varphi_j = 2\pi j/N$  the sequence of intensity distributions  $I(x, y)_j$  can be decomposed into a Fourier series. As derived



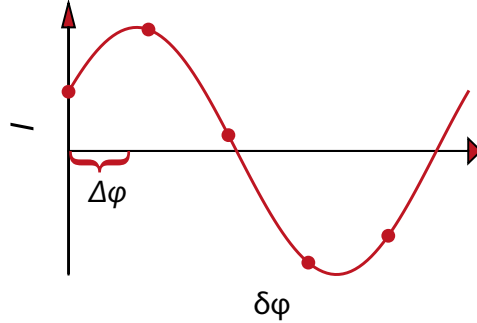


**Figure 5.12:** Principle of phase shift interferometry for one single pixel in the interference pattern. The intensity varies as a function of the relative phase shift  $\delta\phi$ .

in [Sch+83], the phase  $\Delta\varphi$  can be recovered as

$$\tan(\Delta\varphi(x, y)) = \frac{\sum_{j=1}^N I_j(x, y) \sin(\delta\varphi_j)}{\sum_{j=1}^N I_j(x, y) \cos(\delta\varphi_j)}. \quad (5.23)$$

This is also shown in Figure 5.12 for one single position in the interference image as a function of the reference phase. The dots indicate the equidistant offsets  $\delta\phi_j$ . At least  $N = 3$  points have to be measured in order to solve for the offset intensity  $I_r + I_p$ , amplitude  $2\sqrt{I_r I_p}$  and phase  $\Delta\varphi$  in Equation (5.22), increasing this number enhances the precision of the measurement. As derived in [Sch+83], the main source of error in this method is the linearity of the phase shifter. For the SLM used, this is calibrated by the manufacturer so that the quantisation of the phase to an 8 bit value remains as the largest source of error. Figure 5.11 shows this reconstruction and its result (central panel) for a whole image of the interference pattern. Thereby a simultaneous measurement for multiple  $I(x, y)$  is obtained. Because the phase in Equation (5.22) has a linear relationship in x- and y-direction, a linear 2d fit is performed to the unwrapped phase (right panel) to obtain an offset term representing the aberration phase  $\Delta\varphi$ . This fit serves as an average over the whole image subtracting the linear spatial contributions and thereby reducing imaging noise.

When this measurement is performed on a grid of probe beam locations, an aberration map of the optical system is obtained as shown in Figure 5.13 (upper row). The phase measurements in the corners and very centre are not reliable as the patch generating the probe beam is cut off in these cases. All remaining measurements are interpolated to the full SLM resolution of 792x600 pixel by fitting either Zernike

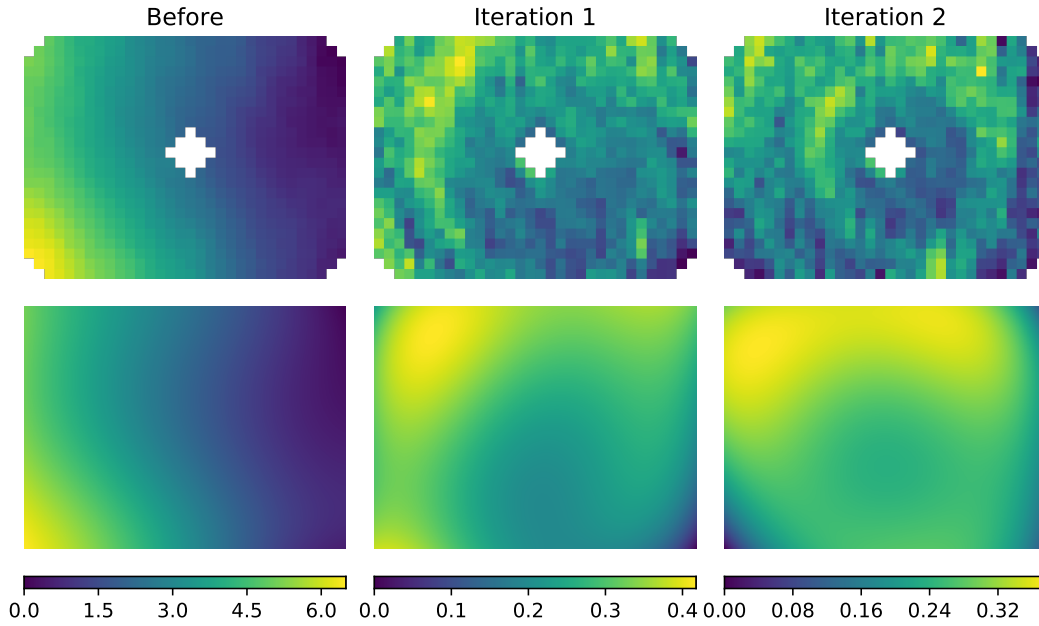


**Figure 5.13:** Phase map of optical aberrations before and after correction for two iterations. In the upper row raw measurements are displayed while the bottom row shows the corresponding fits with Zernike polynomials. The colorbars indicate the phase deviation in units of rad.

polynomials (lower row, see Equation (5.21)) or splines when higher spatial frequencies shall be resolved. After the inverse of this phase is added as a correction to the SLM, the same measurement can be performed again in order to determine the residual error. In order to quantify the residual optical aberrations in a single number, three different metrics are defined

$$\epsilon_{RMS} = \sqrt{\frac{1}{N} \sum_{i=1}^N (\phi_i - \bar{\Psi})^2}, \quad (5.24)$$

$$\epsilon_{max} = \max_i |\phi_i - \bar{\Psi}|, \quad (5.25)$$

$$\epsilon_{PV} = \max_i \phi_i - \min_i \phi_i, \quad (5.26)$$

where  $\epsilon_{RMS}$  describes the root mean square deviation,  $\epsilon_{max}$  the maximum deviation from the mean and  $\epsilon_{PV}$  the peak to valley difference as defined by Hamamatsu. In Figure 5.14 their values are shown for one measurement before correction and two iterations of the method from Figure 5.13. The error before correction is one the order of  $1\lambda$  in terms of Max and PV error. After the first iteration of the algorithm this is reduced by over an order of magnitude for all metrics. It is also



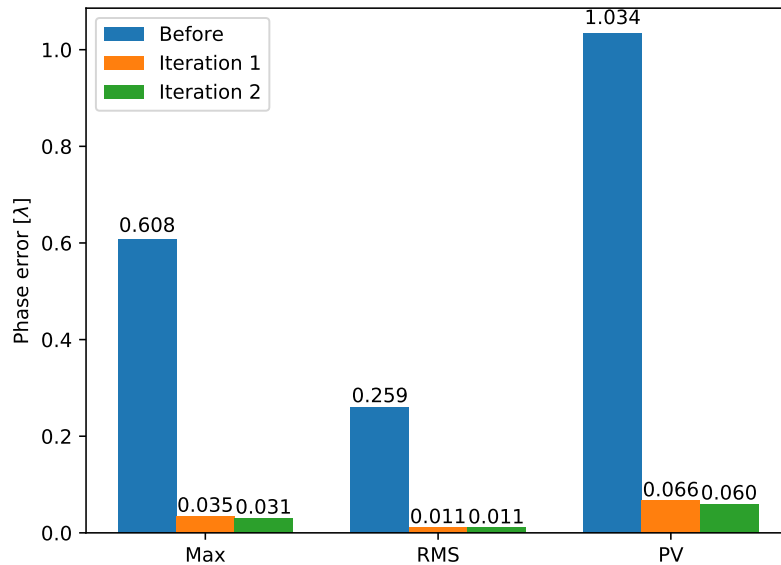


**Figure 5.14:** Different error metrics before and after optical aberration correction. All values are given in terms of  $\lambda$ .

apparent from the figure that a second iteration of the correction method leads to no significant improvement, only for the PV and Max metric a further reduction by 10 % can be observed. Both residual errors in Figure 5.13 are dominated by random noise, however some remaining structure is visible in a ring-like shape. The final RMS error is on the order of  $\lambda/100$  which should allow for a smooth diffraction limited focus. An image of the focus for different stages of correction is shown in Figure 5.15, where a logarithmic scale highlights features at low intensities. The first image shows the point spread function when no correction is applied. In this case severe distortions are visible which are due to a deformation of the SLM chip itself that is not perfectly flat. The central image shows the focus when only the deformation correction pattern supplied by the SLM manufacturer is applied, this corresponds to the case before correction in Figure 5.13. For the right image an additional aberration correction like described above is applied. The resulting point spread function agrees well with the diffraction limited  $\text{sinc}^2$  distribution derived in Equation (5.9).

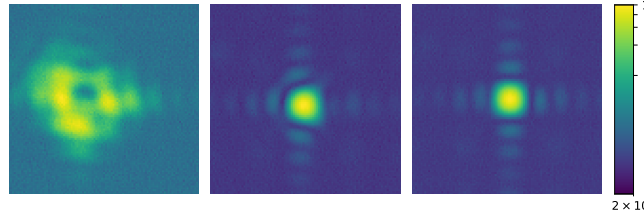


**Figure 5.15:** Images of the focus with no phase correction (left), only the SLM correction pattern supplied by the manufacturer (middle) and the latter one plus measured aberration correction (right) applied. The colour-map is in a logarithmic scale to highlight features at low intensities.

## 5.3 Measurements

In this section experimental measurements using the optical system outlined in Figure 5.4 are presented for the different methods described in the last section. First, some examples of arbitrary light fields are compared in respect of agreement between theoretical predictions and measurements. Secondly, results for a single analytically shaped beam are shown to assess their smoothness and phase distribution. Afterwards, different trap geometries are realized using the optical setup for two beams.

### 5.3.1 Arbitrary light fields

In order to test the performance of the algorithm (described in Section 5.1.4) for creating arbitrary intensities and phases, three different targets are defined that could be useful for trapping atoms. First a ring shape with a radial Gaussian envelope is defined as

$$T(r, \phi) = \exp\left(-\frac{(r-d)^2}{\sigma^2}\right), \quad \Phi(r, \phi) = l\phi \quad (5.27)$$

in polar coordinates with a diameter  $d$  and width  $\sigma$ . This target is shown in the first column of Figure 5.16 and it looks very similar to a Laguerre-Gaussian mode as defined in Equation (5.1) but it possesses a symmetric behaviour in  $r$ . The mask defining the region of control was chosen with a radius  $r = 2d$  and is shown in the second column along with the kinoform (phase pattern on the SLM) resulting from optimization. As the third column shows, the algorithm reaches good agreement between the target and theoretically propagated field for both intensity and phase inside of the masked region. Also the measurement results obtained from the optical setup show in the last column agree qualitatively with the desired field, although they show some imperfections. As a second example a quadratic potential defined



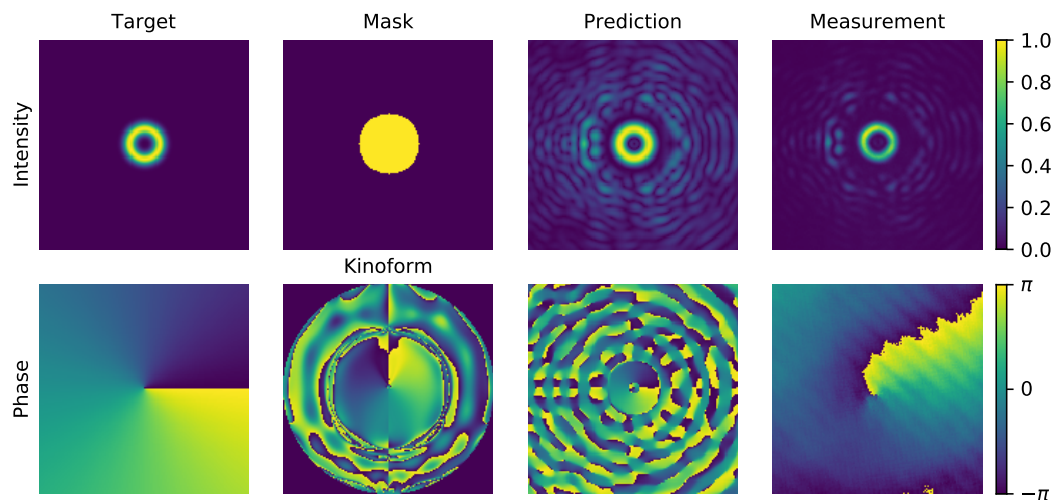


**Figure 5.16:** Overview of arbitrary light shaping for a ring-shaped intensity and a vortex phase. The first column shows the target light field as defined in Equation (5.27) sampled on the computational grid. In the second column a mask defining the region of control and the phase pattern (Kinoform) resulting from optimization is shown. The following two columns show the intensity and phase as predicted by the numerical algorithm Algorithm 1 and measured in the optical setup Figure 5.4. The field of view was approximately matched for the intensity but the measured phase shows a smaller segment. The size of the ring was defined as  $d = 10$  and width  $\sigma = 4$  in focal units.

as

$$T(r, \phi) = \begin{cases} -\left(\frac{r}{r_0}\right)^2 + 1 & \text{for } r \leq r_0 \\ 0 & \text{for } r > r_0 \end{cases}, \quad \Phi(r, \phi) = \text{const.} \quad (5.28)$$

and of size  $r_0$  is shown in Figure 5.17. This is especially relevant for trapping ultracold atoms because it is a truly harmonic potential without higher order terms in contrast to the case of a Gaussian focus. In the case of a rotating trap geometry this could circumvent problems arising from the deconfining term  $r^4$  that plays an increasing role when approaching the deconfinement limit  $\Omega \rightarrow \omega$ . When interfering this trap with a Laguerre-Gauss to create a trap anisotropy, a flat phase is desired. From Figure 5.17 it is apparent that such a quadratic potential can be realized quite

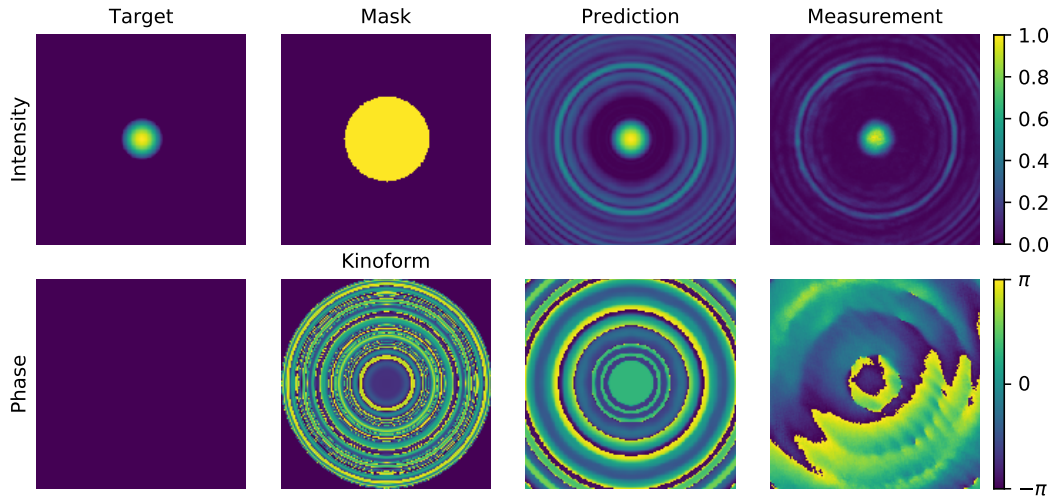


**Figure 5.17:** Overview of arbitrary light shaping analogous to Figure 5.16. As a target intensity a clipped quadratic potential with a flat phase as defined in Equation (5.28) was used. The radius was set to  $r_0 = 10$  focal units.

accurately because the intensity deviates little from a Gaussian beam. However the smoothness of the measured intensity is difficult to assess given the present imaging noise.

As a final test of the algorithms performance a picture containing lines as sharp features and large regions of vanishing intensity is chosen. From Figure 5.18 it is apparent that the high frequency components of the picture cannot be reproduced, even in the theoretical calculation, and all sharp edges look blurred. In the measured intensity distribution this effect is even worse and only the large scale features are resolved. The measured phase shows a large number of vortices and the flat region, visible in the prediction, cannot be identified. For all measurements presented above,



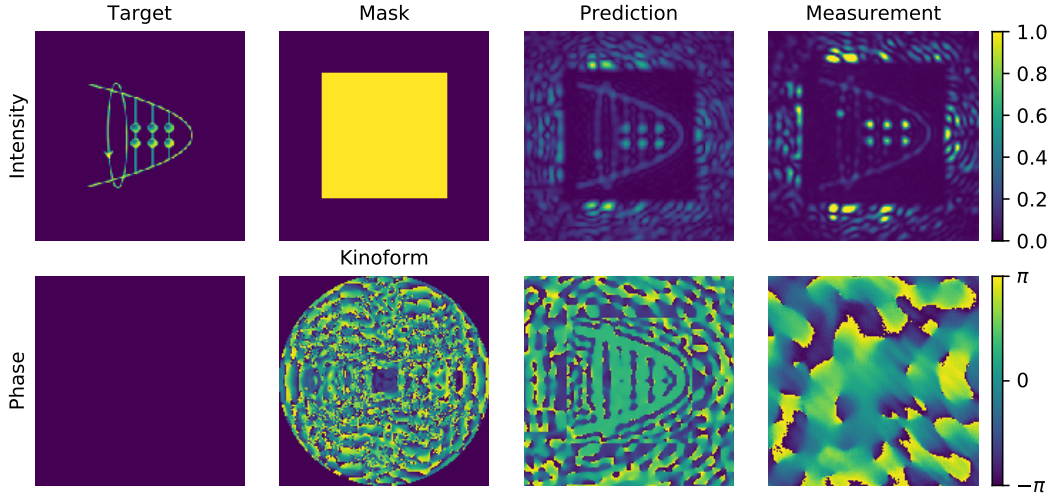


**Figure 5.18:** Overview of arbitrary light shaping analogous to Figure 5.16. As a target intensity the title picture of this thesis along with a flat phase was used.

only a circular subsection of the SLM with a radius of 300 pix was used as this results in a circular point spread function, naturally suiting the rotationally symmetric intensities in Figure 5.16 and Figure 5.17. However, this reduces the already limited resolution of the SLM even further and prohibits access to higher frequency components in the Fourier plane. When compared to other arbitrary intensity-only targets created in [Bru+11],[GH12], [Har+14] or [Bij13] the performance of the present algorithm seems worse when only comparing the intensities. This is certainly expected because the light field is further constrained and some degree of control over the intensity has to be given up in order to set the desired phase. One possibility to increase performance would therefore be to use a SLM with a higher resolution like they are available from HOLOEYE<sup>1</sup> (the device GAEA-2 features  $4000 \times 2160$  pixel). It is worth noting that this in turn would substantially increase the computation time for optimization. Another way to control both amplitude and phase of the light field is described in [Shi+14] as dual-phase modulation. The basic principle is shown in Figure 5.19 and works by interfering two copies of the input beam each modulated by an individual phase  $\theta_{1,2}$ . If these phases are chosen according to

$$\theta_{1,2} = \phi(x, y) \pm \arccos\left(\frac{A(x, y)}{2}\right), \quad (5.29)$$

where  $A$  and  $\phi$  denote the target intensity and phase, the interference yields the

<sup>1</sup><https://holoeve.com/spatial-light-modulators/> However, these device seen to produce a lot of phase noise.

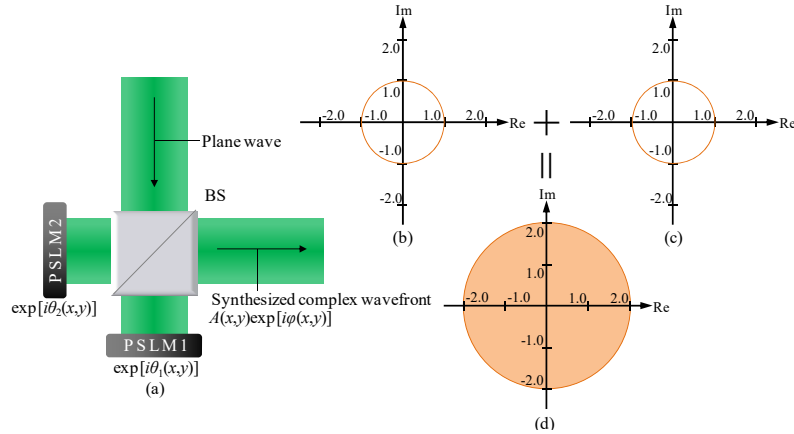


**Figure 5.19:** Dual-phase modulation method by inference of two different phase-only SLMs can control amplitude and phase of the output field (a). Each single SLM can only access the complex unit circle (b),(c) but together they enable access of the complex disk (d). Figure taken from [Shi+14].

desired result

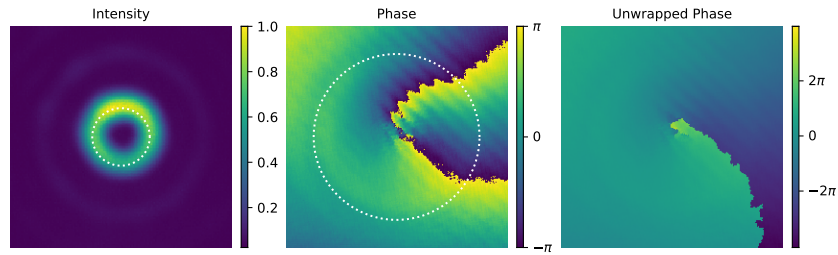
$$\exp(i\theta_1) + \exp(i\theta_2) = A \exp(i\phi). \quad (5.30)$$

This method was shortly evaluated in a slightly modified geometry in order to utilize two halves of the SLM plane to imprint  $\theta_1$  and  $\theta_2$ . This method is advantageous in not requiring an iterative algorithm to obtain the phase pattern but having a simple analytical solution. To obtain the desired field in the focus of a lens an inverse Fourier transform can be performed on the target first. However, this scheme requires careful alignment and is very susceptible to disturbances after the interferometer resulting in intensity fluctuations. Unfortunately it is not possible to simply use this method for two beams because the two modes after the beam-splitter won't overlap for a slightly angled beam. Therefore this route was not pursued further, even when the results for a single beam looked promising.

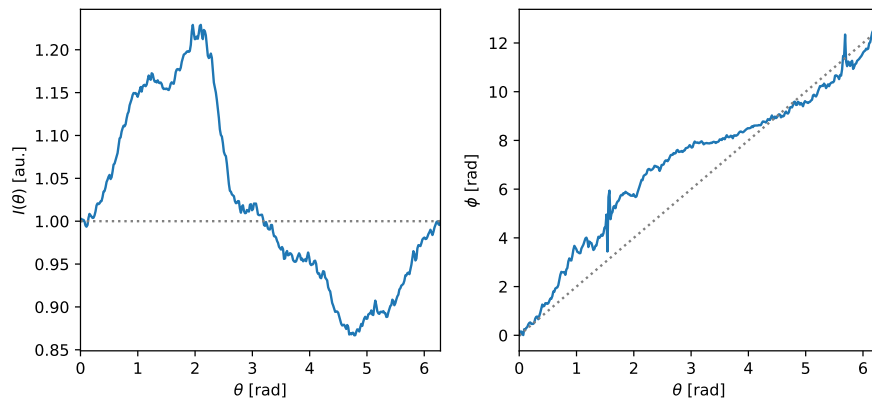
### 5.3.2 Single Beam Amplitude and Phase

The quality of a single Laguerre-Gauss mode is examined in the following since it is an important component of rotating optical traps and an interesting trapping geometry with periodic boundary conditions itself. It is created by displaying a phase vortex as defined in Equation (5.16) and the resulting light field in the image plane is displayed in Figure 5.20. The intensity distribution in (a) shows the expected ring shape, however the amplitude along the angular coordinate is not constant as it is the case for an ideal mode as in Equation (5.1). To quantify this deviation the





(a) Intensity, wrapped and unwrapped phase measured in the image plane.



(b) Angular dependence of intensity and phase at locations indicated by white circles in (a) show deviations from the ideal behaviour (dashed grey line).

**Figure 5.20:** Intensity and phase of a Laguerre-Gauss mode when a phase vortex with  $l = 2$  is displayed on the SLM.

integral

$$I(\theta) = \int_{r_{min}}^{r_{max}} I(r, \theta) r dr \quad (5.31)$$

is evaluated numerically to average over a certain radial range and thereby decrease noise from imaging. The resulting intensity in Figure 5.20b (left panel) shows substantial deviations of more than 20% as well as smaller high frequency components which might be an artefact from the camera pixels. The resulting phase is measured using phase shift interferometry as described in Section 5.2. A mode with  $l = 2$  is created and thus the phase changes by  $4\pi$  around the circumference. This can be seen in the central panel of (a) where it is in addition apparent that the phase does not increase linearly. To see this, a cut along the white dashed circle is depicted in Section 5.2 (right panel) where the unwrapped phase is plotted against the angular coordinate. Apart from the two spikes that are a result of noise present at both phase jumps, a maximal deviation of about 2 rad can be observed. These results indicate that only correcting static aberrations is not sufficient to create smooth potentials suited for trapping of atoms. Additional measures like active camera feedback are necessary to achieve sufficiently precise trapping geometries.

### 5.3.3 Two Beams

So far, only measurements for a single optical mode have been presented. For the creation of rotating traps, however, two beams with different optical frequencies are necessary. As indicated in the schematic Figure 5.4 the two beams coming from optical fibres are combined under a small angle and collimated by a single lens onto the SLM. Because of this angle the collimating lens cannot be perfectly aligned for both beams at the same time but is slightly tilted. To correct for this, optical aberrations are measured and removed like described in Section 5.2. The aberrations before and after correction are shown in Figure 5.21 for both beams. In the first row both phase maps look almost mirrored horizontally as the lens is placed slightly to the left or right of the optical axis for the first and second beam, respectively. With this correction in place two different optical modes can be used to creating rotating traps.

#### Rotating microtrap

First, a rotating microtrap with a small elliptical perturbation should be created in order to prepare FQHE states like described in detail in Chapter 3. For this purpose a Gaussian and Laguerre-Gaussian beam  $L_2^0$  as defined in Equation (5.1) are interfered to obtain an intensity of the form

$$I = \left| L_0^0(\omega) + L_2^0(\omega + \delta\omega) \right|^2 = |A_0|^2 + |A_2|^2 + 2 |A_0 A_2| \cos(2\theta - \delta\omega t), \quad (5.32)$$



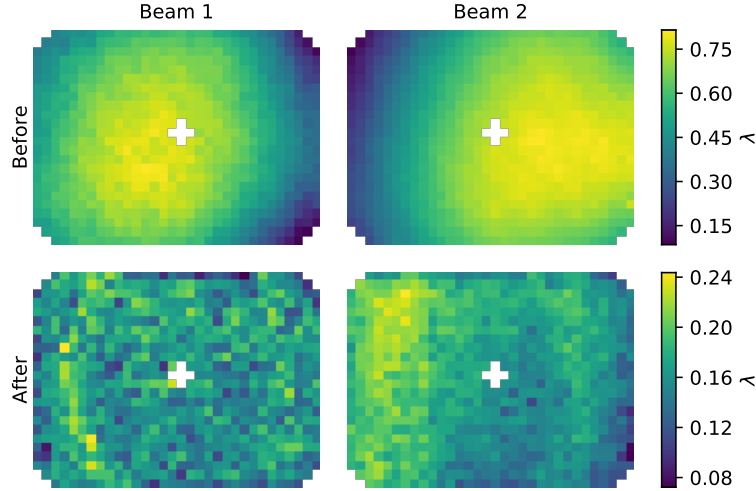


**Figure 5.21:** Optical aberrations of the two-beam setup (see Figure 5.4) when collimating both beams diverging from the fibres with a single lens, before and after correction, respectively.

where the radial dependence is absorbed in  $A$ . The constituents along with the resulting interference are shown in Figure 5.22 in terms of intensity and phase. In order to produce these two modes optically, a combined phase pattern

$$\phi_{total} = \arg \left[ e^{i(\phi_{grad. 1} + \phi_{abb. 1})} + e^{i(\phi_{grad. 2} + \phi_{vortex\ l=2} + \phi_{abb. 2})} \right] + \phi_{SLM\ corr.} \quad (5.33)$$

is displayed. The terms  $\phi_{grad. 1,2}$  describe the two gradients required to overlap the two beams of different frequency and  $\phi_{abb.}$  denote their respective optical aberrations. For one of them an additional vortex  $\phi_{vortex\ l=2}$  is added for creation of the Laguerre-Gauss mode. The SLM deformation correction pattern is equal for both beams and can be added separately. The resulting total phase is shown in Figure 5.23 where the phase vortex is visible as a 'fork'. After spatial filtering of unwanted diffraction orders in an intermediate image plane the resulting intensity is observed on a CMOS camera whose images are shown in Figure 5.24 for three different relative intensities. For the weakest perturbation strength (right panel) the trap has a purely elliptical shape whereas for larger strengths additional structure, especially along the short axis, is visible. However, the relative strengths of the Laguerre-Gauss mode displayed here were chosen for visualisation and are far larger than the actual values on the order of  $10^{-3}$  which would be used in an experiment. The exact shape of the optical potential is determined by the waist of the Gaussian and Laguerre-Gaussian mode and their relative intensity

$$V(x, y, \omega, \xi) = |\mathbf{G}(x, y) + \xi \mathbf{LG}(x, y, \omega, l = 2)|^2, \quad (5.34)$$

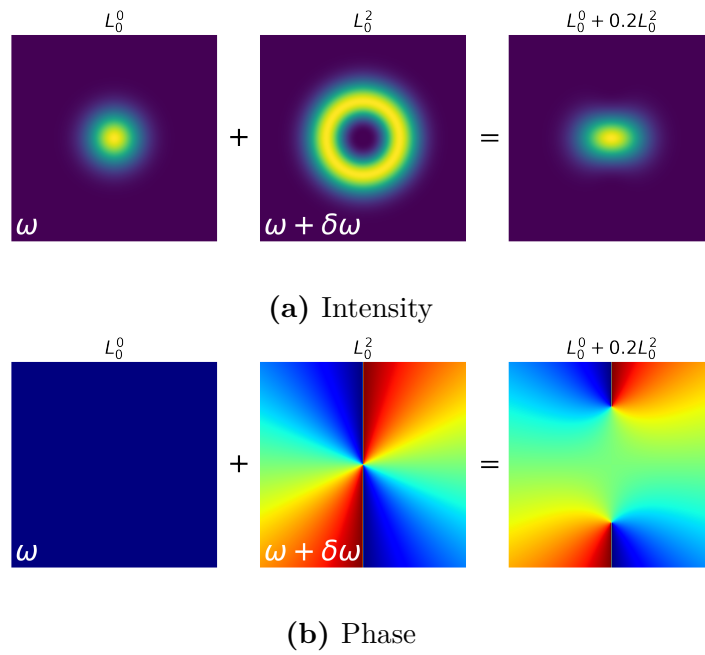


**Figure 5.22:** Interference pattern of a Gaussian and Laguerre-Gaussian beam  $L_2^0$  for a relative intensity of 0.2.

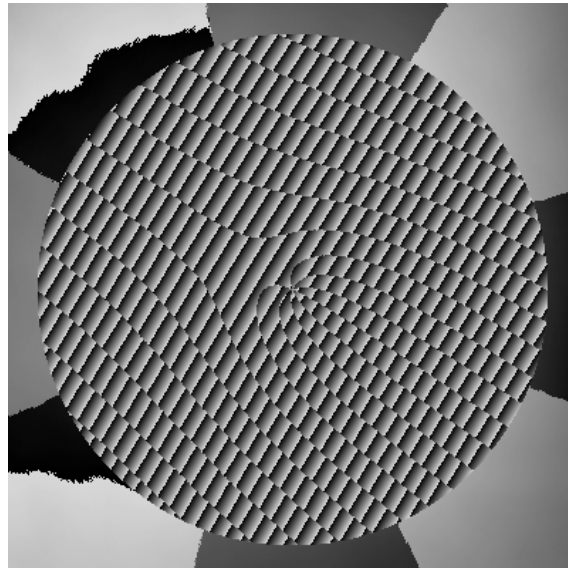


**Figure 5.23:** Phase pattern displayed on the SLM to create the rotating microtrap. It is a superposition of two gratings and a vortex for one of them added to the aberration correction pattern.



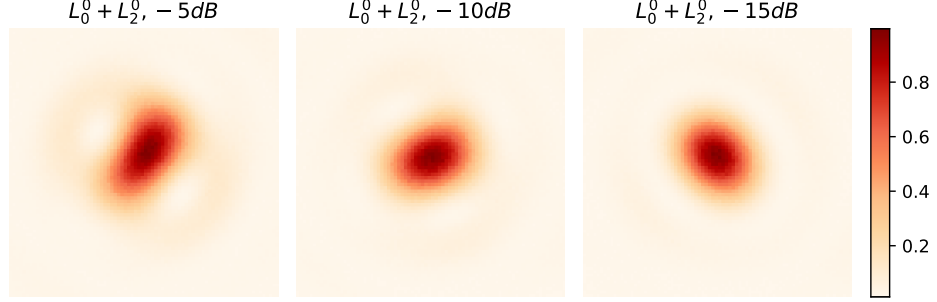


**Figure 5.24:** Camera image of elliptical microtraps from a Gaussian and Laguerre-Gaussian beam  $L_2^0$  for relative intensity of  $-5db$ ,  $-10db$  and  $-15db$  of the latter one.

where the waist of the gaussian beam is set to unity. In order to obtain an analytical expression in terms of the leading orders in  $x$  and  $y$ , an expansion around the origin and for small  $\xi$  yields

$$V(x, y, \omega, \xi) = 1 - 2(x^2 + y^2) + \frac{4\xi}{\omega^2}(x^2 - y^2) + 2(x^4 + y^4) + \quad (5.35)$$

$$\xi \left( \frac{4}{\omega^4} + \frac{4}{\omega^2} \right) (y^4 - x^4) + 4x^2y^2 - 4(x^2y^4 + x^4y^2). \quad (5.36)$$

This contains terms of the desired harmonic trap ( $x^2 + y^2$ ) and anisotropic perturbation ( $x^2 - y^2$ ) which is responsible for the coupling Hamiltonian  $\mathcal{H}_\epsilon$  in Equation (3.17) that enables transfer of angular momentum into the system. By choosing appropriate parameters for the relative waist  $\omega$  and strength  $\xi$  of the Laguerre-Gauss beam, the strength of the anisotropic perturbation can be set as  $\epsilon = 2\xi/\omega^2$ . Here, it is advantageous to choose a larger relative waist of the LG beam in order to minimize influence of higher order terms. As detailed in Section 5.4 these terms can be also minimized by choosing a large waist of the gaussian beam in combination with a high optical power.

### Analysis of trap imperfections

Unfortunately, also unwanted higher perturbations of the order  $\mathcal{O}(x^2y^2)$  and  $\mathcal{O}(x^4 \pm y^4)$  are present in Equation (5.35), that destroy rotational symmetry and can lead to unwanted couplings to states outside the lowest Landau level (LLL). Restriction to the LLL was assumed throughout all of Chapter 3. In order to examine these additional couplings their effect is evaluated in second quantisation where the single particle states can be written as

$$|m, p\rangle = \frac{(a^\dagger)^p (b^\dagger)^m}{\sqrt{p!m!}} |0, 0\rangle \quad (5.37)$$

where the Landau level index  $p$  is now included,  $m$  denotes the angular momentum index and  $a$  and  $b$  are the respective ladder operators. The term  $\epsilon(x^2 - y^2)$  leads to two additional couplings to the one describing only interaction inside a Landau level in Equation (3.17). They can be evaluated to

$$\mathcal{H}_\epsilon^{(1)} = \frac{\epsilon}{2} \sum_{m,p} \left( \sqrt{p+2} \sqrt{p+1} c_{m,p+2}^\dagger c_{m,p} + h.c. \right) \quad (5.38)$$

$$\mathcal{H}_\epsilon^{(2)} = \epsilon \sum_{m,p} \left( \sqrt{p+1} \sqrt{m} c_{m-1,p+1}^\dagger c_{m,p} + h.c. \right) \quad (5.39)$$

where  $c_{m,p}$  are the fermionic mode operators in the Fock-Darwin basis. The first term  $H_\epsilon^{(1)}$  describes excitations to the second next LL while  $H_\epsilon^{(2)}$  reduces angular momentum by two and couples to the first excited LL.

Additional error terms are created when the centres of both beams are misaligned

$$V_u(x, y, \omega, \xi, u) = |\mathbf{G}(x, y) + \xi \mathbf{L} \mathbf{G}(x - u, y, \omega, l = 2)|^2 \quad (5.40)$$

by a displacement  $u$ . To leading order in  $u$  and  $x$  this results in a perturbation of the form

$$V_u(x, y, \omega, \xi, u) - V = \frac{8u\xi}{\omega^2} (x^3 - x) + \xi u \left( \frac{8}{\omega^2} - \frac{16}{\omega^4} \right) xy^2. \quad (5.41)$$

The leading order term  $x$  leads to a coupling Hamiltonian

$$\mathcal{H}_u = u\epsilon \sum_{m,p} \left( \sqrt{p+1} c_{m,p+1}^\dagger c_{m,p} + \sqrt{m+1} c_{m+1,p}^\dagger c_{m,p} + h.c. \right). \quad (5.42)$$

The system is assumed to always be in an eigenstate  $|\Psi_0\rangle$  of the Hamiltonian Equation (3.1) in the LLL with  $p = 0$  when no trap defects are present. Any of the perturbation Hamiltonians Equations (5.39) to (5.42) leads to a decay into a state  $|\Psi_b\rangle \propto \mathcal{H}_\epsilon |\Psi_0\rangle$  in a higher Landau level  $p$  or of different angular momentum  $m$ . In order to quantify the effect of the different terms a simple Rabi oscillation calculation in the two-level system can be employed. The well known expression

$$P_0(t) = 1 - \frac{\Omega^2}{\tilde{\Omega}^2} \sin^2 \left( \frac{\tilde{\Omega}t}{2} \right), \quad \tilde{\Omega} = \sqrt{\Omega^2 + \delta^2} \quad (5.43)$$

describes the depletion of the initial state in terms of the detuning  $\delta = |E_b - E_0|/\hbar$  and Rabi frequency  $\hbar\Omega = 2 \langle \Psi_b | \mathcal{H} | \Psi_0 \rangle$  determined by the coupling matrix element. For large detunings  $\delta \gg \Omega$  the initial state is protected as the Rabi oscillation amplitude is strongly suppressed. In contrary, for the resonant case  $\delta = 0$  it is depleted as  $1 - \sin^2(\Omega t/2)$  which imposes a limit on the total time  $T \ll \Omega^{-1}$  of preparation. In this way, the mayor decay channels can be identified as the ones



with smallest detuning. After preparation of the target state  $|\Psi_0\rangle$  the stirring is removed and only the trap Hamiltonian is present, which reads

$$\mathcal{H}_0 = \sum_{m,p} (m+p) c_{m,p}^\dagger c_{m,p}, \quad (5.44)$$

when including higher Landau levels  $p$ . From this it can be seen that only the state  $|\Psi_b\rangle \propto H_\epsilon^{(2)} |\Psi_0\rangle$  produced by a trap anisotropy is resonant with  $|\Psi_0\rangle$  as the sum  $m+p$  is conserved. Its coupling matrix element and corresponding Rabi frequency can be evaluated to

$$\langle \Psi_b | \mathcal{H}_\epsilon | \Psi_0 \rangle = 4\epsilon \langle \Psi_0 | \sum_{m,p} n_{m,p} | \Psi_0 \rangle = 4\epsilon L = \epsilon 8N(N-1) \quad (5.45)$$

where  $|\Psi_0\rangle$  is assumed to be the  $\Psi_{(1,1,1)}$  state Equation (3.48) with an angular momentum of  $L = 2N(N-1)$  and any intermediate states are omitted for simplicity. The two states  $|\Psi_0\rangle$  and  $|\Psi_b\rangle$  are only resonant in the absence of interactions. Their difference in interaction energy gives rise to a small detuning  $\delta \approx \Delta$ . With this approximation the resonance condition  $\delta \gg \Omega$  can be solved to give an upper bound on  $\epsilon$ . A similar analysis can be performed for the perturbation Hamiltonian  $\mathcal{H}_u$  resulting from misalignment of the two modes. It is apparent that in first order this only results in states which are off-resonant with the target state  $|\Psi_0\rangle$ . Therefore any off-centering contributes very little to the decay and it is suppressed even further by the small amplitude  $\epsilon$  of the stirring beam.

### Rotating cylindrical lattice

The same optical setup can be used to create another interesting trapping geometry in form of a cylindrical lattice. This configuration is described in [Lac+16] in great detail. A two-dimensional cut of the light intensity and corresponding optical trapping potential is shown in Figure 5.25. It is a result of two co-propagating Laguerre-Gaussian modes with opposite angular momentum  $\pm l$ . This forms a one-dimensional ring lattice or a cylindrical one when several layers of the additional confinement in the  $z$ -direction are considered. The authors of [Acki2016] derive a non-interacting Hamiltonian of the form

$$\mathcal{H} = - \sum_{\mathbf{j}} J_{\mathbf{j}}^z e^{i\phi_{\mathbf{j}}} a_{\mathbf{j}}^\dagger a_{\mathbf{j}+\hat{z}} - \sum_{\mathbf{j}} J_{\mathbf{j}}^\phi a_{\mathbf{j}}^\dagger a_{\mathbf{j}+\hat{\phi}} \quad (5.46)$$

where  $J_{\mathbf{j}}^z$  and  $J_{\mathbf{j}}^\phi$  describe nearest-neighbour hopping between sites along the axial  $\hat{z}$  and azimuthal  $\hat{\phi}$  direction. In the first case the atoms pick up a complex phase  $e^{i\phi_{\mathbf{j}}}$  analogous to the effect of a magnetic field piercing the surface of the cylinder. In order to enable tunnelling between the lattice sites their individual potential depths need to be equal to a high precision. To evaluate this property experimentally, a

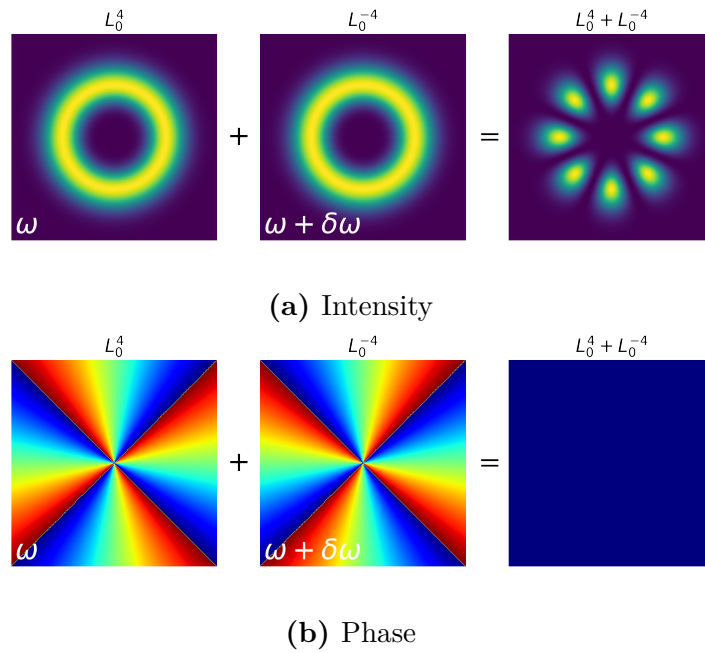


**Figure 5.25:** Interference pattern of a Gaussian and Laguerre-Gaussian beam  $L_2^0$  for a relative intensity of 0.2.

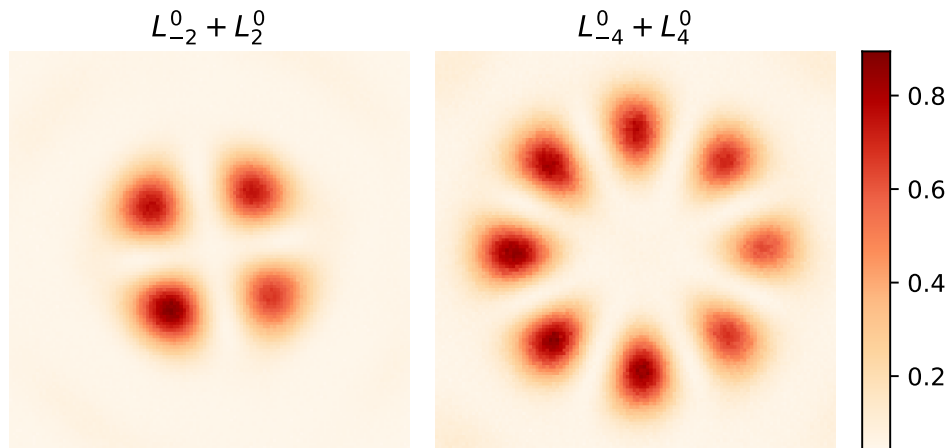


**Figure 5.26:** Camera images of two cylindrical lattices with from two Laguerre-Gaussian modes with  $L_{\pm 2}^0$  (left) and  $L_{\pm 4}^0$  (right).



measurement for two different optical angular momenta  $l$  is shown in Figure 5.26. From the figure it is apparent by eye that the height of the individual intensity maxima varies considerably. An expansion similar to Equation (5.40) can be performed to determine the deviation caused by off-centring between both modes. This misalignment is the main source of error apart from the quality of the individual Laguerre-Gauss modes. Therefore both beams must be carefully adjusted. This alignment could also be achieved through the use of the aberration correction algorithm presented in Section 5.2. First, both beams have to be roughly aligned with a linear gradient for each of them. In this way the same camera ROI can be used for both measurement and any shift between the two foci will be corrected by the linear Zernike polynomials  $R_1^{-1}$  and  $R_1^1$ .

## 5.4 Estimation of realistic experimental parameters

Up to this point, all calculations were performed in dimensionless units. In order to determine optimal parameters for a real experiment, SI units have to be reintroduced by scaling all energies with  $\mathcal{H} = \tilde{\mathcal{H}}\hbar\omega$  and lengths with  $x = \tilde{x}l$  in terms of harmonic oscillator lengths  $l = \sqrt{\frac{\hbar}{m\omega}}$ , where the dimensionless variables are denoted by a tilde. First, the optimal beam parameters yielding the desired trapping frequencies in axial  $\omega_z$  and radial  $\omega$  direction shall be derived. From the optical trapping potential of a Gaussian beam with waist  $w_0$  and total power  $P_0$

$$V(r) = V_0 e^{-\frac{2r^2}{w_0^2}} = V_0 \left( \frac{2r^2}{w_0^2} - \frac{2r^4}{w_0^4} + \mathcal{O}(r^6) \right), \quad V_0 \propto \frac{2P_0}{\pi w_0^2} \quad (5.47)$$

the harmonic oscillator frequency is calculated from the curvature

$$\omega = \sqrt{\frac{1}{m} \partial_r^2 V} = \sqrt{\frac{8P_0}{\pi m w_0^4}}. \quad (5.48)$$

From this it is apparent that the frequency is set by power and waist of the beam where one degree of freedom remains. However, also higher orders like the quartic potential  $r^4$  are present in the potential which are undesirable especially for rotating traps. Their influence can be controlled by choosing the right ratio between beam power and waist. The relevant quantity in this case is the relative strength of the different potential orders at a position one harmonic oscillator length away from the trap centre where the density has dropped to  $e^{-2}$ . This captures the shirking of the ground state wave-packet as the harmonic oscillator frequency is increased. The relative strength of quartic order contributions can be evaluated to

$$\frac{V^{(4)}(l)}{V^{(2)}(l)} = \sqrt{\frac{\pi \hbar^2}{8mP_0}} \propto \sqrt{\frac{1}{P_0}}, \quad \frac{V^{(6)}(l)}{V^{(2)}(l)} \propto \frac{1}{P_0}. \quad (5.49)$$

The results above indicates that unwanted higher orders can be suppressed by choosing a large beam power  $P_0$  and adjusting the waist according to the desired trap frequency. By setting the trapping frequency  $\omega_z$  in the z-direction the correspond-

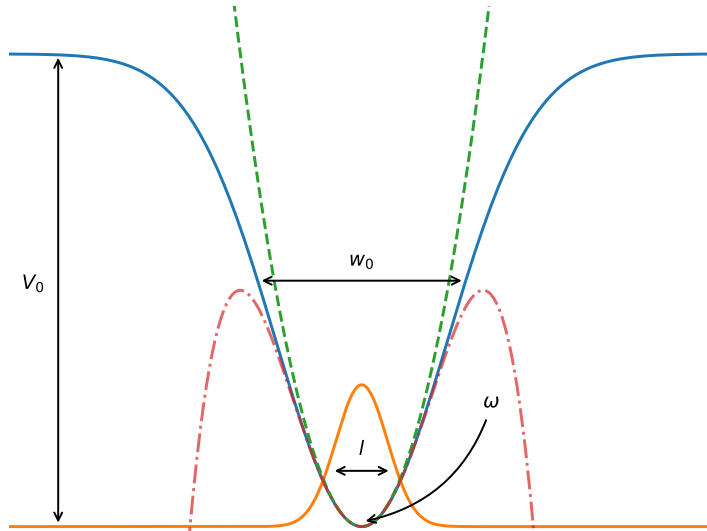


**Figure 5.27:** Optical trapping potential by a gaussian beam (blue) of depth  $V_0$  in harmonic approximation (green) and up to quartic order (red) compared to the ground state wavepacket (orange) with harmonic oscillator length  $l$ . The harmonic oscillator frequency  $\omega$  is determined by the curvature at the origin.

ing harmonic oscillator length  $l_z$  is fixed. A constraint on  $l_z$  is stated in [PPC04] as  $a_0 \ll l_z$  where  $a_0$  denotes the finite range of the interaction. For s-wave scattering of  ${}^6\text{Li}$  this value is approximately  $a_0 \approx 70 a_B$  in units of the Bohr radius  $a_B$ . However, this constraint is quite weak as it allows for trap frequencies on the order of MHz. As a second step, the interaction parameter  $\eta$  in Equation (3.5) has to be determined by setting the scattering length  $a_s$ . As shown in Figure 4.2 it can take large positive and negative values but is constraint by  $a_s \ll l_z$  as specified in [PPC04]. When this condition is evaluated for a frequency of  $2\pi\omega_z = 30 \text{ kHz}$  it reads  $a_s \ll 11\,225 a_B$ . The interaction parameter in dimensionless units can be then calculated as

$$\eta = \sqrt{8\pi} \frac{a_s}{l_z}, \quad \text{with } l_z = \sqrt{\frac{\hbar}{m\omega_z}} \quad (5.50)$$

in terms of scattering length  $a_s$  and harmonic oscillator length  $l_z$  in the strongly confined z-direction. For a scattering length of  $a_s = 2000 a_B$  this results in  $\eta = 0.893$ , i.e.



already close to unity. In Table 5.1 some additional values of  $\eta$  have been calculated for typical trap frequencies and scattering lengths. Two additional constraints have to be fulfilled in order for the lowest Landau level approximation to be valid. They can be understood in terms of the simple picture given in Figure 5.28. In order to

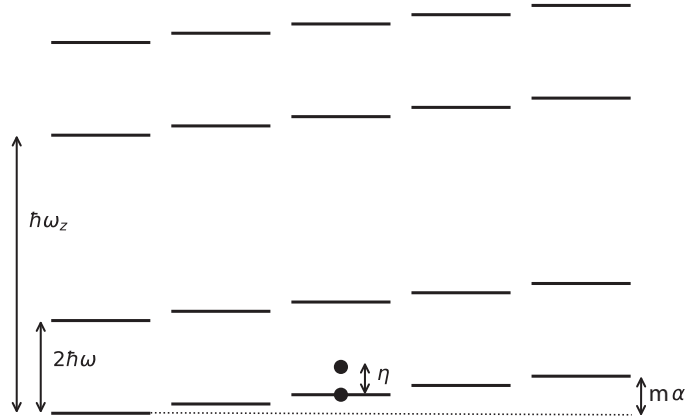


**Figure 5.28:** Energy scales in the Landau level picture. The two lowest Landau levels with a distance of  $2\hbar\omega$  and the first excited level in  $z$ -direction ( $2\hbar\omega_z$ ) are shown. For Fermions the maximal interaction energy per site is  $\eta$  and the remaining tilt of the LLL is given by the distance to the deconfinement limit  $\alpha$ .

remain in the LLL manifold, the interaction energy  $\eta$  per site must be smaller than the gap to first excited LL. In dimensionless units this reads  $\eta \ll 2$  for Fermions, because only two atoms with opposite spin can occupy the same angular momentum state. This weakens the constraint when compared to the bosonic case  $(N-1)\eta \ll 2$  given in [PPC04] already for small particle numbers. As a second restriction, the energy of the highest occupied angular momentum state  $m_{max}$  determined by the tilt  $\alpha$  must still lay below the next highest LL yielding  $(N-1)\alpha \ll 2$  where  $N$  is the number of atoms per spin component. Because all level-crossings already occur at  $\alpha < 0.5$  for  $N_\uparrow = N_\downarrow = 2$  as shown in Figure 3.9 this constraint is fulfilled for small particle numbers and also for larger  $N$  because the critical rotation  $\alpha_c$  decreases for with atom number Figure 3.14. Some realistic parameters are listed in the following table. Another important quantity is the size of the gap  $\Delta$  computed in Figure 3.12 and Figure 3.13. For  $N_\uparrow = N_\downarrow = 2$  it is on the order of 0.05 to 0.02, independent of interaction strength and for all spin manifolds. The time required for an adiabatic evolution across the gap can be approximated as  $T^{-1} = \frac{\omega_z}{2\pi R} \Delta = 25 \text{ Hz to } 10 \text{ Hz}$  for  $2\pi\omega_z = 30 \text{ kHz}$  and an aspect ratio  $R = 60$ . This is still reasonable, when compared

axial trap $2\pi \times \omega_z$ [kHz]	h.o. length $l_z$ [ $a_B$ ]	scattering length $a_s$ [ $a_B$ ]	interaction strength $\eta$
20	13747	1000	0.364
		2000	0.729
		5000	1.823
30	11224	1000	0.446
		2000	0.893
40	9720	1000	0.516
		2000	1.031

**Table 5.1:** Values of the interaction parameter  $\eta$  for some typical trap frequencies  $\omega_z$  and scatterings lengths  $a_s$  set by the Feshbach resonance.

to typical lifetimes of atoms in the microtrap. However, the time required for preparation should be minimized especially in presence of the possible decay channels discussed in Equation (5.39). To this extent, the aspect ratio  $R$  of the trap can be reduced by adding an additional confinement along the radial direction to the relatively weak one produced by the pancake trap described in Section 4.4. This is already achieved by the optical microtrap creating the rotating anisotropy, so that  $R$  can be varied in a certain range while still satisfying the 2d approximation. For the quasi 2d regime to be valid, the condition  $(n_x + n_y)\omega < \omega_z$  with  $n_{x,y}$  the quantum numbers of a cylinder symmetric harmonic oscillator has to be fulfilled. The maximal number  $N_{max}$  of particles accessible in the ground-state along the z-direction of the trap can then be estimated as  $N_{max} = \frac{1}{2}n_x n_y = \frac{\omega_z^2}{2\omega^2} = \frac{1}{2}R^2$ . In the few-particle regime  $N_{max} \approx 10$  per spin component, considered in this thesis, an aspect ratio on the order of  $R \approx 10$  could be already sufficient to be clearly in the 2d regime. This would decrease the time required for adiabatic evolution to  $T^{-1} = 100$  Hz to 40 Hz. Beyond this, more involved control schemes like discussed in [BHM08] or even optimal control methods could be employed to further reduce the time required for preparation.

Lastly, the maximal perturbation strength  $\epsilon$  still compatible with the decay channel into higher Landau levels calculated in Equation (5.45) can be estimated. In order to suppress loss from the target state, the detuning  $\delta$  has to be larger than the Rabi frequency  $\Omega$  determined by the corresponding matrix element. As the detuning is only due to the energy gap  $\Delta$  because of interactions, the inequality  $\delta \gg \Omega$  can



be rewritten in dimensionless units as

$$\Delta \gg 2 \langle \Psi_b | \mathcal{H}_\epsilon | \Psi_0 \rangle = \frac{\epsilon}{2} \sqrt{L} = \frac{\epsilon}{2} \sqrt{2N(N-1)} \approx \frac{\epsilon}{N}. \quad (5.51)$$

For the gap-sizes given above, this results in a condition  $\epsilon \ll 10^{-3}$  for small particle numbers resulting in only small possible perturbation strengths. These can be set choosing the appropriate ratio  $\epsilon = \frac{\xi}{\omega^2}$  in Equation (5.35) of relative beam power  $\xi$  and waist  $\omega$  of the Laguerre-Gauss mode used for stirring.

Parameter	Symbol	Value
axial trap	$\omega_z$	$2\pi \times 30$ kHz
harmonic oscillator length	$l_z$	100 $a_B$
scattering length	$a_s$	$2000 a_B$
interaction parameter	$\eta$	0.5
radial trap	$\omega$	$2\pi \times 500$ Hz
aspect ratio	$R$	60
critical speed of rotation	$\alpha$	$0.7\omega$
perturbation strength	$\epsilon$	$1 \times 10^{-3}$
gap size	$\Delta$	25 Hz

**Table 5.2:** Overview of realistic parameters for realising FQH states.

A number of parameters are relevant for the creation of FQH states in a rotating microtrap. Some of them, like the exact trap frequencies and the scattering length, can be varied to a certain degree while others are constraint through the numerical results like the gap size. Therefore Table 5.2 provides an overview of realistic values suitable for an actual experimental realisation.

# Chapter 6

## Conclusion

### 6.1 Theory

Realisation of quantum Hall states using ultracold fermionic atoms is feasible, as the exact diagonalisation results of Chapter 3 indicate. When compared to spin-polarized electrons in a condensed matter system or ultracold bosons, the introduction of a spin degree-of-freedom opens up a larger richness of possible states. At that the particular interactions determined by s-wave scattering result in an unusual kind of bilayer system with only inter-layer interactions. This is in contrast to similar condensed matter systems where intra-layer interactions usually dominate the inter-layer ones because of the larger spatial distance. Only little literature exists on the theory of spin-full fermions [AR11] [Vyb06] when compared to the spin-polarized case, for which a plethora of work exists, that is in large part summarized in [Han+16]. However there is no prior work on the exact problem for ultracold fermions to our knowledge. Therefore i performed an exact diagonalisation study to identify the sequence of correlated states of different spins concluding in the  $\Psi_{(1,1,1)}$  Halperin [Hal83b] state. No avoided level crossings are present among the different spin manifolds in the spectra Figure 3.9, Figures B.1 to B.3 since the total spin is conserved. Only states in the same spin sector as the initially prepared one are therefore accessible without breaking the associated  $SU(2)$  symmetry. Inside a spin-manifold, introduction of an anisotropic perturbation opens up an energy gap that was calculated in Figure 3.12 and Figure 3.13. This enables either adiabatic preparation [PPC04] by following a path of maximal gap size, or a scheme involving pulses [BHM08] in the control parameters. Only results for a relatively small atom numbers up to five particles per spin were obtainable numerically because of the exponentially increasing dimensionality of the problem. However, it is intriguing that states of only so few atoms already show the characteristic properties of the quantum Hall effect. This is in contrast to many other correlated many-body phenomena like BCS superconductivity, where a large number of particles is required in order give rise to the effect. This limited number of atoms is also favourable for preparation and detection of quantum Hall with ultracold atoms. Opposed to condensed matter systems, where primarily bulk-properties like conductivity of a sample can be studied,



imaging of individual atoms is possible in a quantum gas experiment. This enables observation of the full wavefunction and access to correlations. As demonstrated in Section 3.3.2, the two-body correlation function  $g_{\sigma,\sigma'}^{(2)}(\mathbf{r}, \mathbf{r}')$  for different spins is well suited in order to detect and verify spinful quantum Hall states. It provides a distinct signature in the case of the  $\Psi_{(1,1,1)}$  state. Also the experimental parameters required for preparation of FQHE states in a rotating micro-trap were evaluated in Section 5.4. Especially the large scattering lengths obtainable by a Feshbach resonance in  ${}^6\text{Li}$  turn out to decrease the required speeds of rotation considerably when compared to a bosonic species [Gem07]. As shown in Figure 3.14 interesting states are already accessible at around 70 % of the trap frequency for realistic interactions strengths. This reduces the influence of trap anharmonicities present in all optical traps.

## 6.2 Experiment

In Chapter 5 an optical setup for the creation of rotating optical microtraps was built and evaluated. It relies on the technique of spatial light modulation in order to shape the required optical modes. Some properties of the SLM device used were characterized in Section 5.1.2. Only little crosstalk between neighbouring pixels seems to be present when compared to measurements in [Ron+12] enabling high utilisation of the devices resolution. Removal of wavefront aberrations present in optical systems proved crucial to obtain a diffraction-limited focus. For this purpose an interferometric phase measurement technique was implemented in Section 5.2. Using the resulting wavefront map as a correction, a residual error of  $\epsilon_{RMS} = 0.011\lambda$  and  $\epsilon_{PV} = 0.060\lambda$  could be obtained. Optical components with a flatness on the order of  $\lambda/20$  are considered 'precision grade' which is only attainable for mirrors. For lenses, or even a whole optical assembly, the errors on the wavefront are usually far larger. This illustrates the performance of the aberration correction algorithm. In order to facilitate more control over the optical trapping potential, an algorithm for creation of arbitrary light fields was examined in Section 5.1.4. This method enables control over amplitude and phase in the atom plane required for an interference based trap. Albeit the results in Figures 5.16 to 5.18 show that this technique works in principle, the resulting intensities are not yet suited for trapping of ultracold atoms. The performance of this method might be improved by an active feedback algorithm or an increased resolution of the SLM device. Therefore, analytical beam-shaping is used to create the Gaussian and Laguerre-Gaussian beams producing the rotating microtrap. The resulting anisotropic perturbation yields an elliptically shaped trap responsible for the introduction of angular momentum into the atomic sample. At that, the exact parameters of the trap can be precisely controlled in terms of the relative waist and power of the two optical modes. The interferometric principle of the rotating trap enables large rates of rotation up to MHz while the exact frequency

can be set with a precision only limited by the RF source used. Overall this provides accurate and fast control of the systems parameter in order to navigate the landscape of the energy gap.

As the main result, this thesis identifies an experimentally realistic parameter regime enabling the study of FQHE physics using ultracold fermions. When the optical setup for rotating traps is built into the experiment, this gives access to a completely new class of many-body states for cold atoms.

## 6.3 Outlook

The next thing to do is to incorporate the optical system built during this thesis into the actual experiment. All major ingredients as deterministic preparation and single-particle resolved imaging are already working there. For this, additional electronics for stabilisation of the optical intensities and control of the RF signals are necessary. After that, all aberrations of the combined optical system could be measured at the position of the atoms using the interferometric technique described in Section 5.2. This measurement could take a substantial amount of time (approx. 10 h), but is crucial in order to obtain a diffraction-limited trap. Subsequently, first experiments can be performed and analysed in terms of two-body correlation function as calculated in Section 3.3.2. For an increased speed of preparation a more involved control scheme like in [BHM08] could be applied. To that end the numerical algorithm could easily be extended to include time-dependent parameters.

In addition, the exact diagonalisation study could be extended in many directions incorporating additional processes also accessible in the experiment.

As one possibility, interactions among atoms of the same spin-state could be included. In an experiment with ultracold fermions this could be realised by means of a p-wave Feshbach resonance [Zha+04]. A simple delta potential as employed for s-wave scattering between different spins cannot capture the interactions among same spin atoms since the different contributions as indicated in Equation (3.13) cancel out because of the fermionic anti-commutation relations. Instead an effective potential describing p-wave scattering like it is presented in [RJ04] and derived with great detail in [RF01] would be necessary. To convert this into a second-quantised form, the matrix elements analogous to Equation (3.5) would have to be evaluated in terms of the complex coordinates. For another route, one could devise a sort of spin-orbit coupling which links an atoms spin degree-of-freedom to its angular momentum orbital. This would break the  $SU(2)$  symmetry of the spin sector and could lead to a richer structure of level crossings. Unfortunately the coupling of the atoms to an optical potential is not dependent on spin. Therefore a spatially varying magnetic or radio frequency field would have to be used. This is however difficult to achieve because of the rotational symmetry of the single-particle orbitals. Lastly, the species  ${}^6\text{Li}$  features three high-field seeking hyperfine components. These



states labelled  $|1\rangle$ ,  $|2\rangle$  and  $|3\rangle$  could be used to form a three-component quantum Hall system with  $SU(3)$  symmetry.

Further theoretical work into the states obtained by the exact diagonalisation could be gained by computing the so-called entanglement spectrum [LH08]. The entanglement spectrum is a generalisation of the entanglement entropy and can be used to identify topological order in certain FQHE states. The notion of entanglement always involves a decomposition of the full Hilbertspace  $\mathcal{H}$  into two partitions  $\mathcal{H}_A \otimes \mathcal{H}_B$ , obtained by a cut along a certain border. For the spinful FQHE this cut can be made either between both spin components or at a certain angular momentum mode. The spectrum is then derived from a Schmidt decomposition with coefficients  $e^{-\frac{1}{2}\xi_i}$  as singular values. The 'energy levels'  $\xi_i$  can reveal a gap identifying topologically ordered states as detailed in [LH08]. Such a spectrum could be obtained with the numerical code, however they require further interpretation.

# Bibliography

- [Aba+16] Martín Abadi et al. “TensorFlow: Large-Scale Machine Learning on Heterogeneous Distributed Systems”. In: (2016). DOI: 10.1038/nm.3331. arXiv: 1603.04467.
- [AR11] E Ardonne and N Regnault. “Structure of spinful quantum Hall states: A squeezing perspective”. In: *Physical Review B - Condensed Matter and Materials Physics* 84.20 (2011). DOI: 10.1103/PhysRevB.84.205134. arXiv: 1107.2232.
- [BBS86] Donald J. Bone, H.-a. Bachor, and R. John Sandeman. “Fringe-pattern analysis using a 2-D Fourier transform”. In: *Applied Optics* 25.10 (1986), p. 1653. DOI: 10.1364/AO.25.001653.
- [Ber+18] Andrea Bergschneider et al. “Spin-resolved single-atom imaging of  $^6\text{Li}$  in free space”. In: *Physical Review A* 97.6 (June 2018), p. 063613. DOI: 10.1103/PhysRevA.97.063613. arXiv: 1804.04871.
- [Ber17] Andrea Bergschneider. “Strong correlations in few-fermion systems”. In: (2017).
- [BHM08] Stefan K. Baur, Kaden R A Hazzard, and Erich J. Mueller. “Stirring trapped atoms into fractional quantum Hall puddles”. In: *Physical Review A - Atomic, Molecular, and Optical Physics* 78.6 (2008), pp. 1–4. DOI: 10.1103/PhysRevA.78.061608. arXiv: 0806.1517.
- [Bij13] van RMW Rick Bijnen. *Quantum engineering with ultracold atoms*. 2013. DOI: 10.6100/IR754785.
- [Bru+11] Graham D Bruce et al. “A smooth, holographically generated ring trap for the investigation of superfluidity in ultracold atoms Related content Feedback-enhanced algorithm for aberration correction of holographic atom traps A smooth, holographically generated ring trap for the i”. In: *Phys. Scr* 143 (2011), pp. 14008–5. DOI: 10.1088/0031-8949/2011/T143/014008.
- [Bru+74] J. H. Bruning et al. “Digital Wavefront Measuring Interferometer for Testing Optical Surfaces and Lenses”. In: *Applied Optics* 13.11 (1974), p. 2693. DOI: 10.1364/AO.13.002693.



- [Chi+10] Cheng Chin et al. “Feshbach resonances in ultracold gases”. In: *Reviews of Modern Physics* 82.2 (2010), pp. 1225–1286. DOI: 10.1103/RevModPhys.82.1225. arXiv: 1401.2945.
- [CS96] Jean-François Cardoso and Antoine Souloumiac. “Jacobi Angles for Simultaneous Diagonalization”. In: *SIAM Journal on Matrix Analysis and Applications* 17.1 (Jan. 1996), pp. 161–164. DOI: 10.1137/S0895479893259546.
- [Fet09] Alexander L. Fetter. “Rotating trapped Bose-Einstein condensates”. In: *Reviews of Modern Physics* 81.2 (2009), pp. 647–691. DOI: 10.1103/RevModPhys.81.647. arXiv: 0801.2952v1.
- [Flä+16] N. Fläschner et al. “Experimental reconstruction of the Berry curvature in a Floquet Bloch band”. In: *Science* 352.6289 (May 2016), pp. 1091–1094. DOI: 10.1126/science.aad4568. arXiv: 1509.05763.
- [Fra+07] S Franke-Arnold et al. “Optical ferris wheel for ultracold atoms.” In: *Optics express* 15.14 (2007), pp. 8619–8625. DOI: 10.1364/OE.15.008619. arXiv: 0611154 [physics].
- [GBZ16] N. Goldman, J. C. Budich, and P. Zoller. “Topological quantum matter with ultracold gases in optical lattices”. In: *Nature Physics* 12.7 (2016), pp. 639–645. DOI: 10.1038/nphys3803. arXiv: 1607.03902.
- [Gem07] Nathan Gemelke. “Nathan D Gemelke June 2007 t”. In: June (2007).
- [GH12] Alexander L. Gaunt and Zoran Hadzibabic. “Robust Digital Holography For Ultracold Atom Trapping”. In: *Scientific Reports* 2.1 (2012), p. 721. DOI: 10.1038/srep00721. arXiv: 1111.5941.
- [Gre+13] Daniel Greif et al. “Short-Range Quantum Magnetism Optical Lattice”. In: *Science* 340.June (2013), pp. 1307–1310. DOI: 10.1126/science.1236362.
- [GSC10] Nathan Gemelke, Edina Sarajlic, and Steven Chu. “Rotating Few-body Atomic Systems in the Fractional Quantum Hall Regime”. In: (2010), pp. 1–22. arXiv: 1007.2677.
- [GWO00] Rudolf Grimm, Matthias Weidemüller, and Yurii B. Ovchinnikov. “Optical Dipole Traps for Neutral Atoms”. In: *Advances in Atomic, Molecular and Optical Physics* 42.C (2000), pp. 95–170. DOI: 10.1016/S1049-250X(08)60186-X. arXiv: 9902072 [physics].
- [Hal83a] F. D.M. Haldane. “Fractional quantization of the hall effect: A hierarchy of incompressible quantum fluid states”. In: *Physical Review Letters* 51.7 (1983), pp. 605–608. DOI: 10.1103/PhysRevLett.51.605.
- [Hal83b] B.I. Halperin. “Theory of the quantized Hall conductance University of California When the Fermi level is between two Landau levels , the longitud  $\sigma_{xx}$ ”. In: *Helvetica Physica Acta* 56.1-3 (1983), pp. 75–102.

- [Han+16] T. H. Hansson et al. “Quantum Hall Physics - hierarchies and CFT techniques”. In: (2016), pp. 1–68. DOI: 10.1103/RevModPhys.89.025005. arXiv: 1601.01697.
- [Har+14] Tiffany Harte et al. “A conjugate gradient minimisation approach to generating holographic traps for ultracold atoms”. In: 22.22 (2014), pp. 26548–26558. DOI: 10.1364/OE.22.026548. arXiv: 1408.0188.
- [HK10] M. Z. Hasan and C. L. Kane. “Colloquium: Topological insulators”. In: *Reviews of Modern Physics* 82.4 (2010), pp. 3045–3067. DOI: 10.1103/RevModPhys.82.3045. arXiv: 1002.3895.
- [Hol14] Marvin Holten. “Hamiltonian Engineering in Ultracold Atom Experiments using a Spatial Light Modulator”. PhD thesis. University of Heidelberg, 2014.
- [Hol17] Marvin Holten. “Collective Modes and Turbulence in Two-Dimensional Fermi Gases”. PhD thesis. University of Heidelberg, 2017.
- [Jai89] J. K. Jain. “Composite-fermion approach for the fractional quantum Hall effect”. In: *Physical Review Letters* 63.2 (1989), pp. 199–202. DOI: 10.1103/PhysRevLett.63.199. arXiv: arXiv:1011.1669v3.
- [KB14] Diederik P. Kingma and Jimmy Ba. “Adam: A Method for Stochastic Optimization”. In: (2014), pp. 1–15. DOI: <http://doi.acm.org.ezproxy.lib.ucf.edu/10.1145/1830483.1830503>. arXiv: 1412.6980.
- [KL09] Alexei Kitaev and Chris Laumann. “Topological phases and quantum computation”. In: (2009). arXiv: 0904.2771.
- [KM01] Bernard Kress and Patrick Meyrueis. *Digital Diffractive Optics*. John Wiley & Sons, Ltd, 2001.
- [Lac+16] Mateusz Lacki et al. “Quantum Hall physics with cold atoms in cylindrical optical lattices”. In: *Physical Review A* 93.1 (2016). DOI: 10.1103/PhysRevA.93.013604. arXiv: 1507.00030.
- [Lau] Robert B. Laughlin. “Elementary Theory: the Incompressible Quantum Fluid”. In: *The Quantum Hall Effect*. Ed. by Richard E. Prange and Steven M. Girvin. Springer-Verlag.
- [Lau83] R. B. Laughlin. “Anomalous quantum Hall effect: An incompressible quantum fluid with fractionally charged excitations”. In: *Physical Review Letters* 50.18 (1983), pp. 1395–1398. DOI: 10.1103/PhysRevLett.50.1395. arXiv: 1111.4781.



- [LH08] Hui Li and F. D M Haldane. “Entanglement spectrum as a generalization of entanglement entropy: Identification of topological order in non-Abelian fractional quantum hall effect states”. In: *Physical Review Letters* 101.1 (2008), pp. 1–4. DOI: 10.1103/PhysRevLett.101.010504. arXiv: 0805.0332.
- [LK90] Dung-hai Lee and Charles L Kane. “Boson-vortex-Skyrmion duality, spin-singlet fractional quantum Hall effect, and spin-1/2 anyon superconductivity”. In: *Physical Review Letters* 64.12 (Mar. 1990), pp. 1313–1317. DOI: 10.1103/PhysRevLett.64.1313.
- [Loh+16] M. Lohse et al. “A Thouless quantum pump with ultracold bosonic atoms in an optical superlattice”. In: *Nature Physics* 12.4 (2016), pp. 350–354. DOI: 10.1038/nphys3584. arXiv: 1507.02225v1.
- [Loh+18] Michael Lohse et al. “Exploring 4D quantum Hall physics with a 2D topological charge pump”. In: *Nature* 553.7686 (2018), pp. 55–58. DOI: 10.1038/nature25000. arXiv: 1705.08371.
- [Mah12] Virendra N. Mahajan. “Orthonormal polynomials in wavefront analysis: analytical solution: errata”. In: *Journal of the Optical Society of America A* 29.8 (2012), p. 1673. DOI: 10.1364/JOSAA.29.001673.
- [MDD02] R. H. Morf, N. D’Ambrumenil, and S. Das Sarma. “Excitation gaps in fractional quantum Hall states: An exact diagonalization study”. In: *Physical Review B - Condensed Matter and Materials Physics* 66.7 (2002), pp. 754081–7540818. DOI: 10.1103/PhysRevB.66.075408. arXiv: 0202407 [cond-mat].
- [Oka+11] Atsushi Okamoto et al. “Holographic diversity interferometry for optical storage”. In: *Optics Express* 19.14 (2011), p. 13436. DOI: 10.1364/OE.19.013436.
- [Pet16] Ram-Janik Petzold. “A two-dimensional optical dipole trap for a system of few ultracold fermions”. PhD thesis. University of Heidelberg, 2016.
- [PPC04] M. Popp, B. Paredes, and J. I. Cirac. “Adiabatic path to fractional quantum Hall states of a few bosonic atoms”. In: *Physical Review A - Atomic, Molecular, and Optical Physics* 70.5 B (2004), pp. 1–6. DOI: 10.1103/PhysRevA.70.053612. arXiv: 0405195 [cond-mat].
- [PPZ18] Ioannis Petrides, Hannah M. Price, and Oded Zilberberg. “The 6D quantum Hall effect and 3D topological pumps”. In: (2018). arXiv: 1804.01871.
- [RC03] N. Read and N. R. Cooper. “Free expansion of lowest Landau level states of trapped atoms: a wavefunction microscope”. In: *Order A Journal On The Theory Of Ordered Sets And Its Applications* 3.1 (2003), p. 5. DOI: 10.1103/PhysRevA.68.035601. arXiv: 0306378 [cond-mat].

- [RF01] R. Roth and H. Feldmeier. “Effective s- and p-wave contact interactions in trapped degenerate Fermi gases”. In: *Physical Review A. Atomic, Molecular, and Optical Physics* 64.4 (2001), pp. 436031–4360317. DOI: 10.1103/PhysRevA.64.043603. arXiv: 0102416 [cond-mat].
- [RJ04] N. Regnault and Th Jolicoeur. “Quantum Hall fractions in ultracold fermionic vapors”. In: *Physical Review B - Condensed Matter and Materials Physics* 70.24 (2004), pp. 1–4. DOI: 10.1103/PhysRevB.70.241307. arXiv: 0404093 [cond-mat].
- [Ron+12] Emiliano Ronzitti et al. “LCoS nematic SLM characterization and modeling for diffraction efficiency optimization, zero and ghost orders suppression”. In: *Optics Express* 20.16 (2012), p. 17843. DOI: 10.1364/OE.20.017843.
- [Sch+04] V. Schweikhard et al. “Rapidly Rotating Bose-Einstein Condensates in and near the Lowest Landau Level”. In: *Physical Review Letters* 92.4 (2004), p. 4. DOI: 10.1103/PhysRevLett.92.040404. arXiv: 0308582 [cond-mat].
- [Sch+83] J. Schwider et al. “Digital wave-front measuring interferometry: some systematic error sources”. In: *Applied Optics* 22.21 (1983), p. 3421. DOI: 10.1364/AO.22.003421.
- [Ser+11] F Serwane et al. “Deterministic preparation of a tunable few-fermion system”. In: *Science* 332.6027 (Apr. 2011), pp. 336–338. DOI: 10.1126/science.1201351. arXiv: 1101.2124.
- [Ser11] Friedhelm Serwane. “Deterministic preparation of a tunable few-fermion system”. PhD thesis. Ruperto-Carola-University of Heidelberg, Germany, 2011.
- [Shi+14] Atsushi Shibukawa et al. “Digital phase conjugate mirror by parallel arrangement of two phase-only spatial light modulators”. In: *Optics Express* 22.10 (2014), p. 11918. DOI: 10.1364/OE.22.011918.
- [Son+93] S. L. Sondhi et al. “Skyrmions and the crossover from the integer to fractional quantum Hall effect at small Zeeman energies”. In: *Physical Review B* 47.24 (1993), pp. 16419–16426. DOI: 10.1103/PhysRevB.47.16419.
- [Tho83] D. J. Thouless. “Quantization of particle transport”. In: *Physical Review B* 27.10 (1983), pp. 6083–6087. DOI: 10.1103/PhysRevB.27.6083.
- [TIK82] Mitsuo Takeda, Hideki Ina, and Seiji Kobayashi. “Fourier-transform method of fringe-pattern analysis for computer-based topography and interferometry”. In: *Journal of the Optical Society of America* 72.1 (1982), p. 156. DOI: 10.1364/JOSA.72.000156.



- [Ton16] David Tong. “Lectures on the Quantum Hall Effect”. In: January (2016). DOI: 10.1007/978-1-4612-3350-3. arXiv: 1606.06687.
- [TSG82] D C Tsui, H L Stormer, and A C Gossard. “Two-dimensional magnetotransport in the extreme quantum limit”. In: *Physical Review Letters* 48.22 (1982), pp. 1559–1562. DOI: 10.1103/PhysRevLett.48.1559. arXiv: arXiv:1011.1669v3.
- [Vie08] Susanne Viefers. “Quantum Hall physics in rotating Bose-Einstein condensates”. In: (2008). DOI: 10.1088/0953-8984/20/12/123202. arXiv: 0801.4856.
- [Vyb06] Karel Vyborny. “Spin in fractional quantum Hall systems”. In: (2006). DOI: 10.1002/andp.200610228. arXiv: 0603451 [cond-mat].
- [ZBN16] Junyi Zhang, Jérôme Beugnon, and Sylvain Nascimbene. “Creating fractional quantum Hall states with atomic clusters using light-assisted insertion of angular momentum”. In: *Physical Review A* 94.4 (2016). DOI: 10.1103/PhysRevA.94.043610. arXiv: 1608.07460.
- [Zha+04] J Zhang et al. “P-wave Feshbach resonances of ultracold Li-6”. In: *Physical Review A* 70.3 (2004), p. 30702. DOI: 10.1103/PhysRevA.70.030702. arXiv: 0406085 [quant-ph].
- [ZW10] Jingang Zhong and Jiawen Weng. “Generalized Fourier analysis for phase retrieval of fringe pattern.” In: *Optics express* 18.26 (2010), pp. 26806–20. DOI: 10.1364/OE.18.026806.
- [Zwi+05] M. W. Zwierlein et al. “Vortices and superfluidity in a strongly interacting Fermi gas”. In: *Nature* 435.7045 (2005), pp. 1047–1051. DOI: 10.1038/nature03858. arXiv: 0505635 [cond-mat].

# Appendix A

## Exact diagonalisation algorithm details

Exact diagonalisation is a well-established numerical technique, yet some details specific to the system considered in this thesis are explained for reference. Every ED calculation consists of three major steps:

- Choose a computational basis of the Hilbertspace
- Build the Hamiltonian matrix
- Compute eigenvalues and eigenstates by diagonalisation

For the spinful fermionic quantum Hall effect, the natural representation of basis states is given in terms of the occupation number basis

$$|n_0, n_1, \dots, n_M\rangle_{\uparrow} |n_0, n_1, \dots, n_M\rangle_{\downarrow} \quad (\text{A.1})$$

in terms of angular momentum modes  $n_m$  for two spin components  $\{\uparrow, \downarrow\}$  from Equation (3.30). Fermi statistics only allow one occupation per orbital and spin, therefore a state could be described as a vector of booleans. To make the implementation generic enough to also allow for bosons, each  $n_m$  is represented by a uint8 allowing for up to 255 particles per mode. The length of each state vector is determined by the angular momentum cut-off  $M$ , which is assumed to be equal for both spin components for simplicity. All possible basis states with a constrained number of particles can be generated by standard algorithms for drawing mode numbers without or with replacement (for fermions and bosons, respectively). The resulting number of states equals the Hilbert space dimensions

$$\dim(\mathcal{H})_F = \binom{M}{N}^{2s+1}, \quad \dim(\mathcal{H})_B = \left( \binom{M}{N} \right) = \binom{M+N-1}{N} \quad (\text{A.2})$$

where  $s$  is the single-particle spin for fermions and bosons are considered spin-less.

To find a matrix representation of the Hamiltonian under consideration all basis states are labelled using a single index  $|i\rangle$ ,  $i = 1, \dots, \dim(\mathcal{H})$ . For each of the



states  $|i\rangle$  the action of the operators  $a_m \in \{b_m, c_m\}$  in the Hamiltonian is evaluated  $\mathcal{H}|i\rangle = h_{ij}|j\rangle$  leading to a new state  $|j\rangle$  and a complex number  $h_{ij}$ . These coefficients are stored in a sparse matrix representing the Hamiltonian. This format of storage is much more efficient in terms of memory because most of the entries in  $h$  are vanishing. Already for a small number of atoms the resulting matrices can have sizes on the order of GBs, as they scale with  $\mathcal{O}(\dim(\mathcal{H})^2)$ . Therefore, a computation of all eigenstates is prohibitive. Instead, only the lowest-lying states including the ground-state are computed using a Implicitly Restarted Arnoldi Method implemented in ARPACK<sup>1</sup>. These methods are much faster than a full diagonalisation when only a small number of states is desired. They are also usually very good at finding the largest eigenvalues, but for the spectrum of a Hamiltonian the lowest energies are of interest. Therefore, the ARPACK algorithms offer an option to solve a shifted problem and return the eigenvalues  $\lambda' = \frac{1}{\lambda - \sigma}$ . In order to solve for the lowest energies, the shift parameter is set to  $\sigma = 0$ . The diagonalisation results in a number of eigenstates

$$|\Psi_\alpha\rangle = \sum_{i=1}^{\dim(\mathcal{H})} \xi_i |i\rangle \quad (\text{A.3})$$

in terms of coefficients  $\xi_i$  for the basis states  $|i\rangle$  and corresponding energies  $E_\alpha$ . These are real numbers when the operator  $\mathcal{H}$  is hermitian, as it is the case for physical Hamiltonians. The eigenvalues of the states with respect to some observable  $O$  could then be calculated as  $O|\Psi_\alpha\rangle = o|\Psi_\alpha\rangle$ , however this is not well conditioned because of floating point errors. Instead, expectation value  $\bar{o} = \langle\Psi_\alpha|O|\Psi_\alpha\rangle$  and variance  $\Delta o = \langle\Psi_\alpha|(O - \bar{o})^2|\Psi_\alpha\rangle$  are calculated. If the variance falls below a certain threshold the state can be considered an eigenstate. So far, the diagonalisation procedure is fairly ordinary. A complication arises through the large degeneracy of states in terms of interaction energy especially for the highest spin manifold as observable in Figure 3.10. This degeneracy causes the eigenstates of  $\mathcal{H}$  to not necessarily be eigenstates of total spin  $S$ , but some linear combination thereof. The only possibility to resolve this problem and compute the spin of these states is to resort to a simultaneous diagonalisation. Although this is a standard technique in analytical calculations, surprisingly few numerical algorithms exist [CS96] which are not readily available and much slower than usual diagonalisation routines. Luckily there is an exception in the special case when only two hermitian matrices  $A$  and  $B$  have to be diagonalised simultaneously. By combining them into a complex matrix  $C = A + iB$ , the resulting matrix  $C$  is *normal* ( $C^\dagger C = C C^\dagger$ ) in case when the two matrices commute  $[A, B] = 0$  as it is the case for the Hamiltonian and spin-operator  $[\mathcal{H}, S] = 0$ . Then  $C$  is always diagonalisable by a unitary transformation  $C = UDU^\dagger$  where  $D = \text{diag}(\lambda_1, \dots, \lambda_N)$  contains the eigenvalues and  $U$  the corresponding eigenvectors. As a result, eigen-energies  $E$  and spin-eigenvalues  $S$  can be read off

---

<sup>1</sup><https://www.caam.rice.edu/software/ARPACK/>

---

as the real and imaginary parts  $\lambda_j = E_j + iS_j(S_j + 1)$ , this is analogous for the eigenstates.

Only in this way the spectra of states Figure 3.10 and energies Figure 3.9 can be labelled with the total spin of each state. Using this method the existing highly optimized numerical routines can be utilised increasing the computational time only slightly. It is worth noting that the shift-value  $\sigma$  has to be set to different imaginary values  $\sigma = is(s + 1)$ ,  $s = 0, \dots, S$  in order to obtain all eigenstates up to a total spin  $S$ .





# Appendix B

## Extended figures

For future reference, also spectra for higher atom numbers are shown in the following.

### B.1 Spectra for higher particle numbers

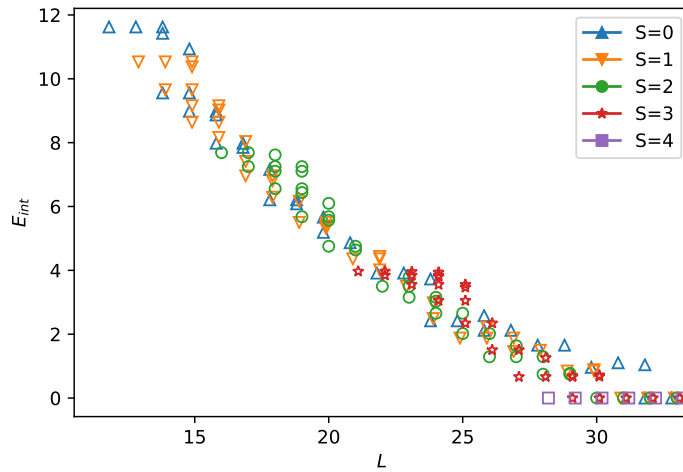


**Figure B.1:** Spectrum of states analogous to Figure 3.11, but for  $N_{\uparrow} = N_{\downarrow} = 4$  particles. Only the lowest lying states were computed because of the large dimension of the Hilbertspace. A variety of additional states exists to the right of the ones displayed here. They represent excited states of the ground-states visible at the lower left edge and are not of particular interest in general. Higher total spins  $S$  are accessible due to the increased particle number. The  $\Psi_{(1,1,1)}$  state can be found at an angular momentum of  $L = 28$  and total spin  $S = 4$ . In the  $S = 0$  manifold, the first state with vanishing interaction energy occurs at  $L = 32$ .



# spin-up $N_{\uparrow}$	# spin-down $N_{\downarrow}$	spin states $ S, S_z\rangle$
3	2	$ \frac{1}{2}, \frac{1}{2}\rangle,  \frac{3}{2}, \frac{1}{2}\rangle,  \frac{5}{2}, \frac{1}{2}\rangle$
2	3	$ \frac{1}{2}, -\frac{1}{2}\rangle,  \frac{3}{2}, -\frac{1}{2}\rangle,  \frac{5}{2}, -\frac{1}{2}\rangle$
4	3	$ \frac{1}{2}, \frac{1}{2}\rangle,  \frac{3}{2}, \frac{1}{2}\rangle,  \frac{5}{2}, \frac{1}{2}\rangle,  \frac{7}{2}, \frac{1}{2}\rangle$
4	3	$ \frac{1}{2}, -\frac{1}{2}\rangle,  \frac{3}{2}, -\frac{1}{2}\rangle,  \frac{5}{2}, -\frac{1}{2}\rangle,  \frac{7}{2}, -\frac{1}{2}\rangle$

**Table B.1:** Possible spin configurations for the spin-imbalanced case.

## B.2 Imbalanced spin components

Throughout Chapter 3, an equal number  $N_{\uparrow} = N_{\downarrow}$  of spin-up and -down particles was assumed. In order to study the effect of an imbalance, two cases with a difference  $N_{\uparrow} - N_{\downarrow} = 1$  of one atom are calculated. As a consequence of the imbalance the z-projection  $S_z$  of the total spin is no longer zero. Instead it can be evaluated to

$$S_z = \frac{1}{2} \sum_j n_{j,\uparrow} - n_{j,\downarrow} = \frac{1}{2}(N_{\uparrow} - N_{\downarrow}). \quad (\text{B.1})$$

In Table B.1 the possible spin configurations for some imbalanced number of spin-up and -down atoms are shown, Figure B.2 and Figure B.3 show the corresponding spectra of states.

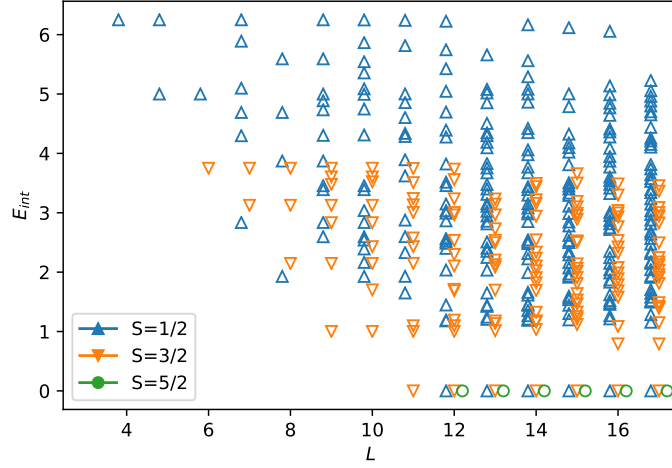


**Figure B.2:** The spectrum of states for  $N_{\uparrow} = 3, N_{\downarrow} = 2$  shows the interaction energy  $E_{int}$  versus the total angular momentum  $L$ . In contrast to Figure 3.10, Figure 3.11 and Figure B.1 the first state to minimize interaction energy does not belong to the highest, but the intermediate spin-manifold.

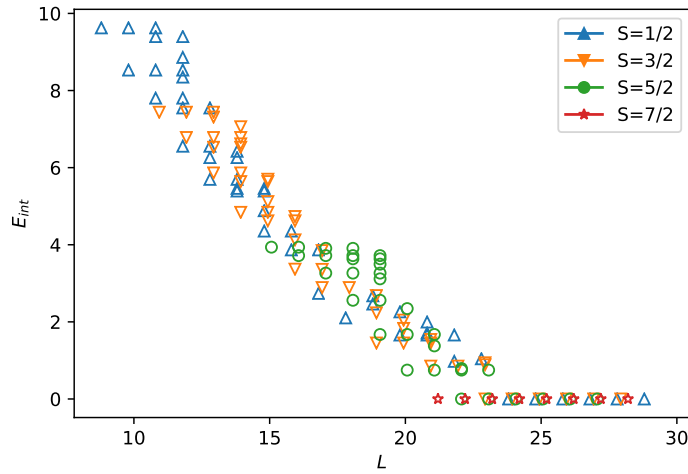
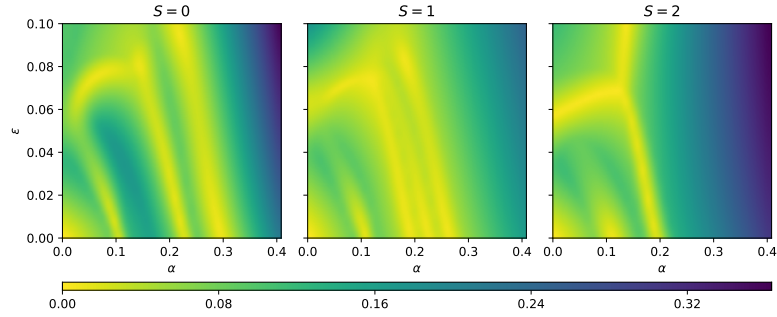


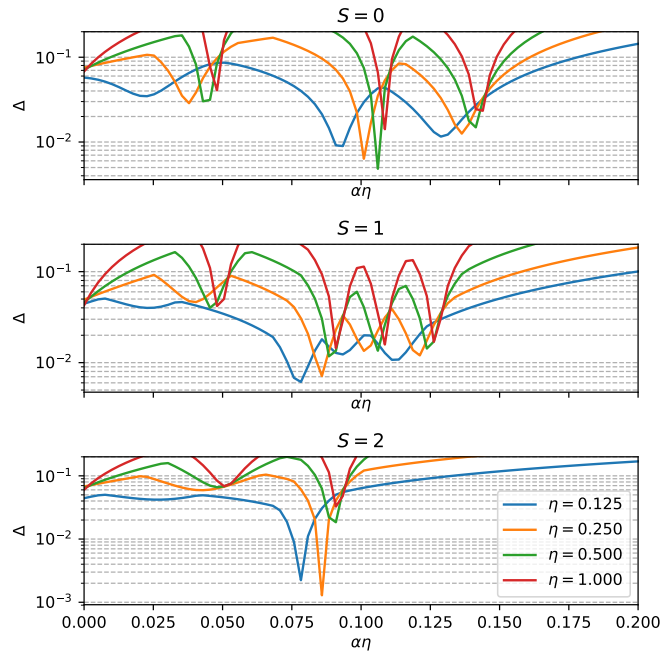
**Figure B.3:** The same figure as in Figure B.2 but for  $N_{\uparrow} = 4, N_{\downarrow} = 3$  particles.



### B.3 Energy Gap for higher particle numbers



(a) The gap  $\Delta$  is computed as a function of rotational frequency  $\alpha$  and perturbation strength  $\epsilon$  for an interaction parameter  $\eta = 0.25$ .



(b) Cut of (a) along a line with  $\epsilon = 0.02$  shown on a logarithmic scale for different interactions strengths  $\eta$ .

**Figure B.4:** Energy gap between ground- and first excited state inside a manifold of spin  $S$  for  $N_{\uparrow} = N_{\downarrow} = 3$  particles. The frequency of rotation  $\alpha$  and has been scaled by  $\eta$  in order to collapse the lines of different  $\eta$  onto each other.

## B.4 Density and two-body correlation functions

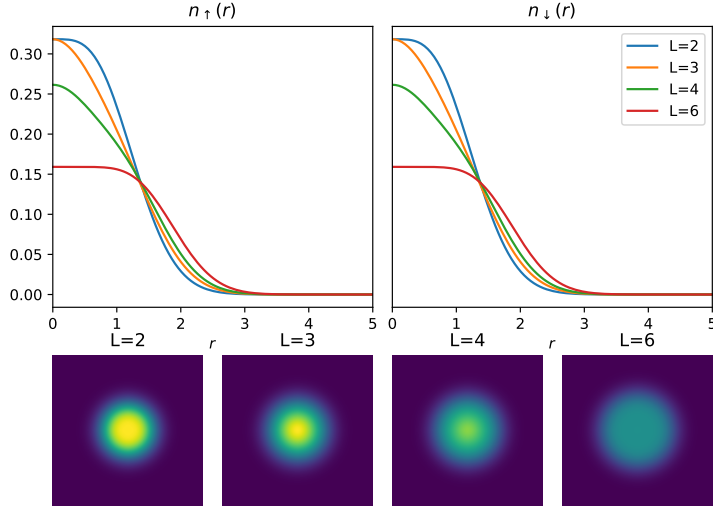


**Figure B.5:** Single particle density of both spin-components for  $N_{\uparrow} = N_{\downarrow} = 2$  for the sequence of groundstates  $L = 2, 3, 4, 6$ . The lower panels show the two-dimensional density distribution for the corresponding states.

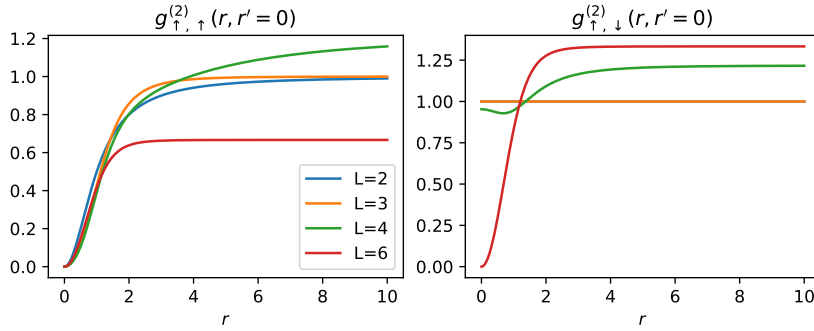


**Figure B.6:** The radial part of the two-body correlation function Equation (3.26) is depicted for the same sequence of states as in Figure B.5. The second particle is always fixed at the origin.



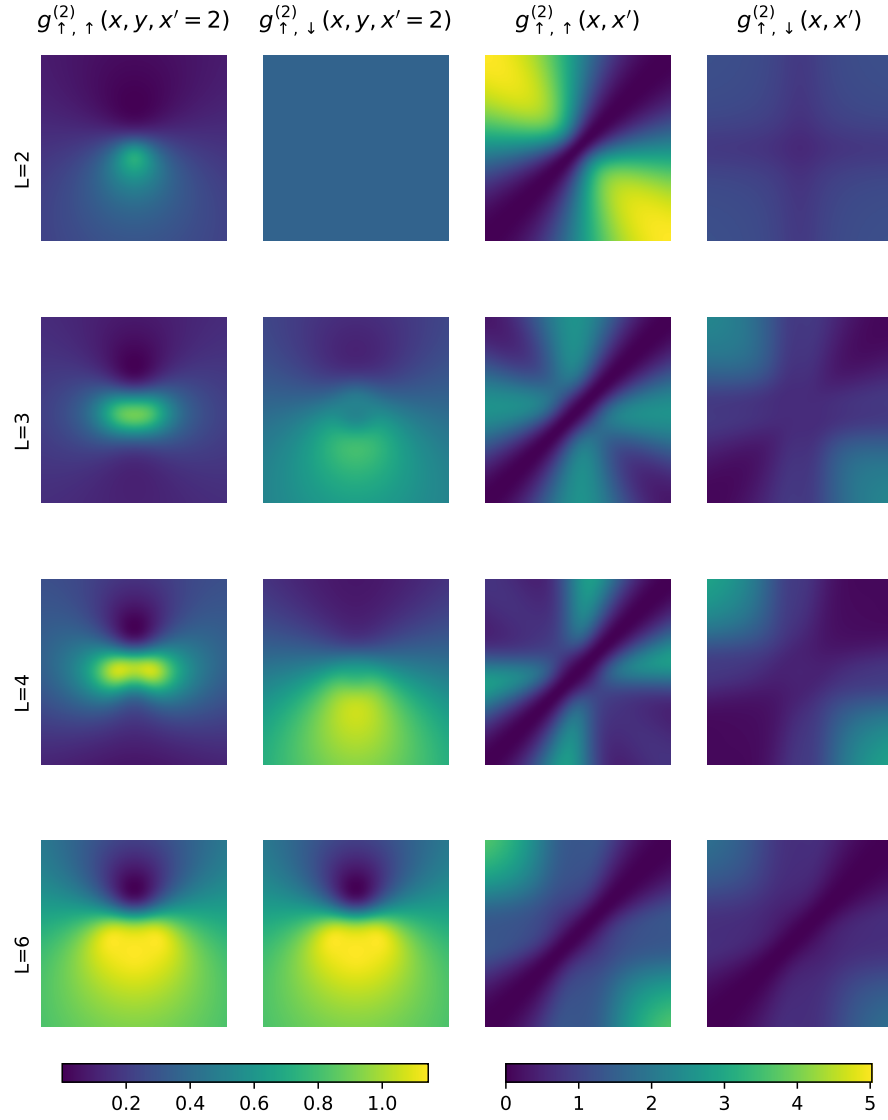


**Figure B.7:** Two-body correlation function  $g_{\sigma,\sigma}^{(2)}(x, x')$  for the sequence of groundstates denoted by angular momenta  $L$  (rows). The two-dimensional dependence on the first particle is shown when the second one is fixed away from the origin ( $x' = 2$ ) for equal (first row) and opposite (second row) spins. Third and fourth column show the particles correlation as a function of both radii for equal (third row) and opposite (last row) spins. All plots in the first two and second two columns share the same colourbars (bottom). This plot was computed for  $N_{\uparrow} = N_{\downarrow} = 2$  particles.

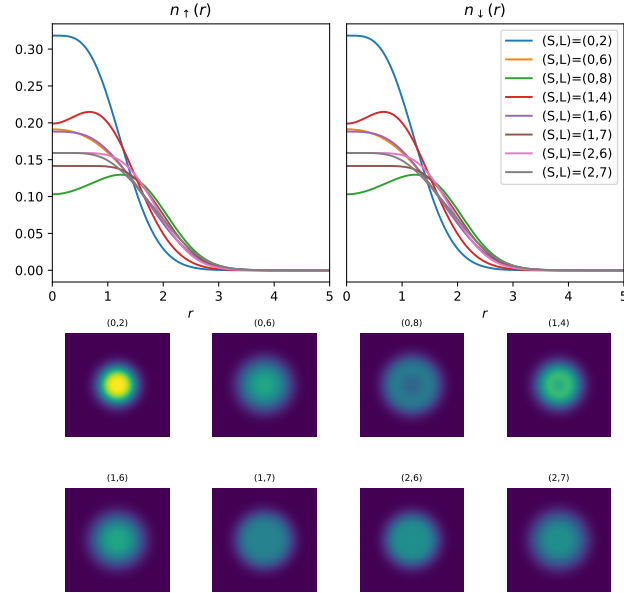


**Figure B.8:** Single particle density for  $N_{\uparrow} = N_{\downarrow} = 2$  as in Figure B.5. Instead of the ground-states a number of other interesting states that lie at cusps in the spectrum are depicted, they are denoted by total spin  $S$  and angular momentum  $L$ .

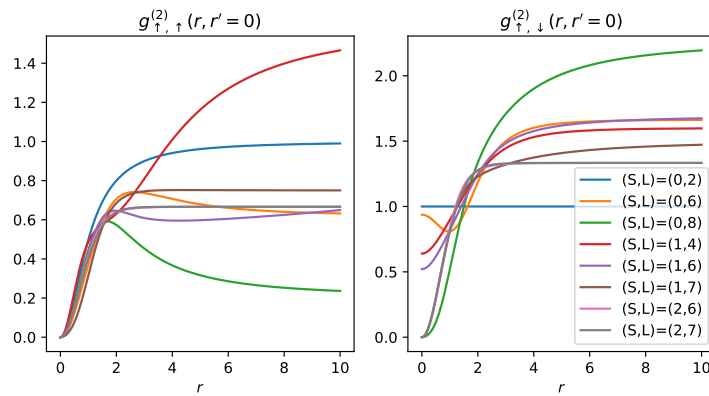


**Figure B.9:** Radial two-body correlation function for  $N_{\uparrow} = N_{\downarrow} = 2$  as in Figure B.6. The same states as in Figure B.8 are shown.

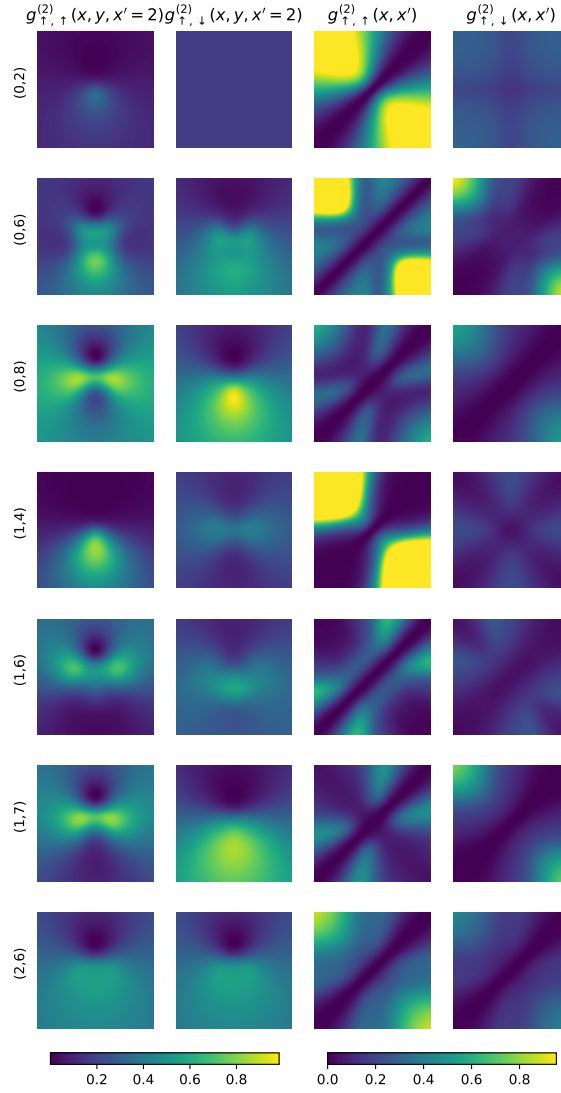


**Figure B.10:** Full two-body correlation function for  $N_{\uparrow} = N_{\downarrow} = 2$  as in Figure B.7. The same states as in Figure B.8 are shown. In some regions the correlation function  $g_{\sigma,\sigma'}^{(2)}(x, x')$  clips because of numeric instabilities at large distances.

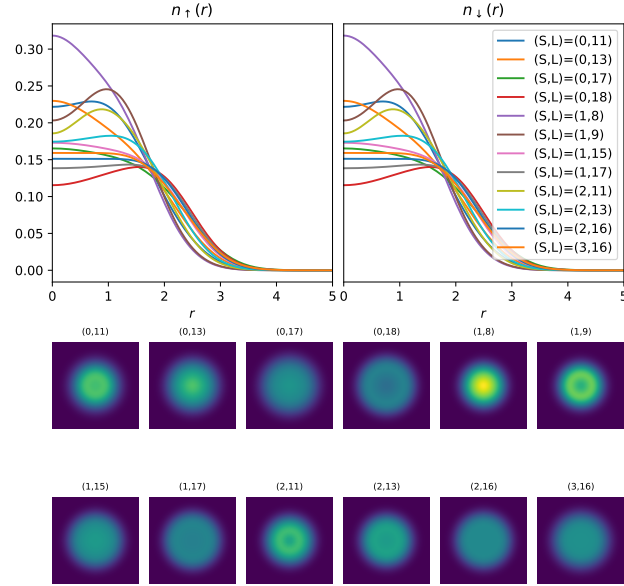


**Figure B.11:** Single particle density for  $N_{\uparrow} = N_{\downarrow} = 3$  as in Figure B.5. Additional interesting states distinct from the ground-states in Figure 3.15 that lie at cusps in the spectrum are depicted. They are denoted by total spin  $S$  and angular momentum  $L$ .

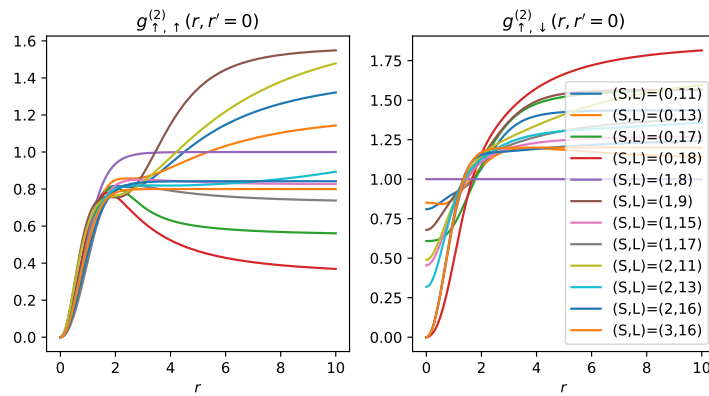


**Figure B.12:** Radial two-body correlation function for  $N_{\uparrow} = N_{\downarrow} = 3$  as in Figure 3.16. The same states as in Figure B.11 are shown.

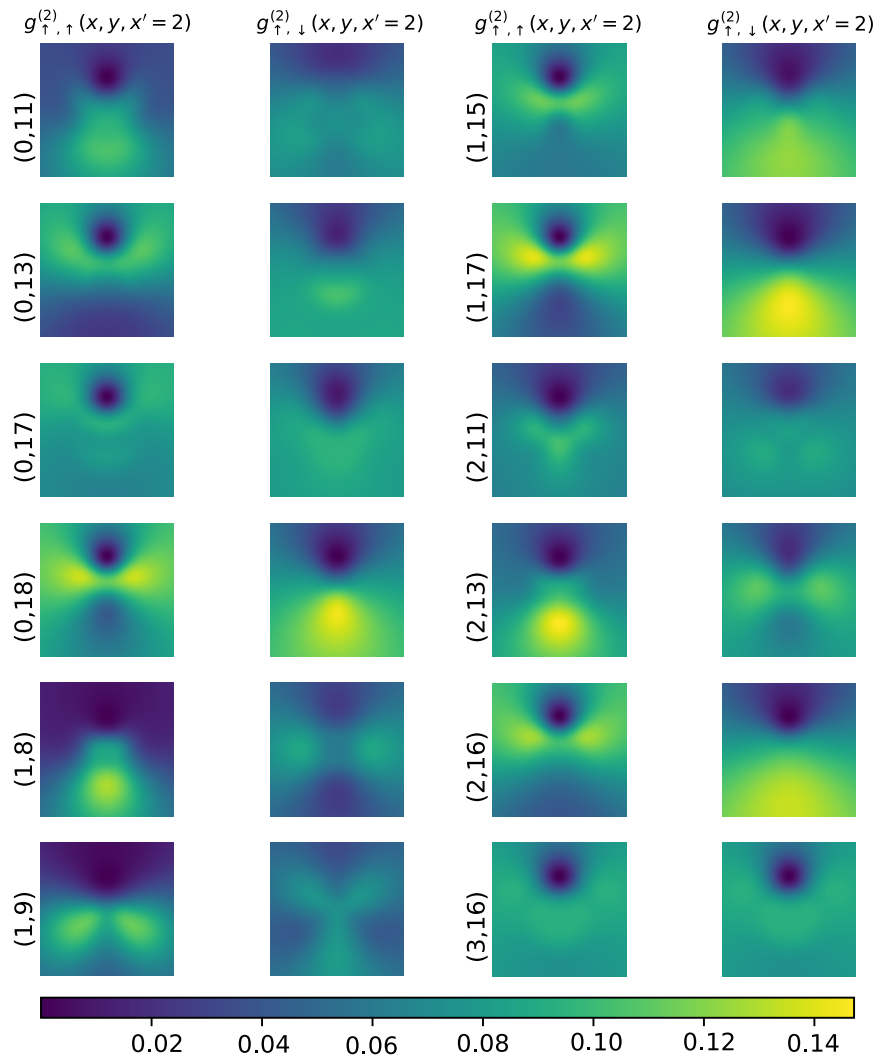


**Figure B.13:** Full two-body correlation function for  $N_{\uparrow} = N_{\downarrow} = 3$  as in Figure 3.17. The same states as in Figure B.11 are shown.

## Danksagung

An dieser Stelle möchte ich mich bei allen bedanken, die zum Gelingen dieser Arbeit beigetragen haben.

Zu aller erst gilt mein Dank Philipp, für die gute Betreuung während der gesamten Dauer meiner Masterarbeit und die vielen interessanten Diskussionen. Deine Kommentare haben meinen Blick immer wieder auf das Wesentliche gelenkt.

Außerdem danke ich Selim für die Aufnahme in deine Gruppe und die ansteckende Begeisterung für Physik.

Ich danke der gesamten ultracold Gruppe für die schöne Atmosphäre, insbesondere Ralf, Luca und Jan Hendrik für die zahlreichen Kaffeepausen. Vielen Dank auch an Marvin für die Hilfe mit all meinen LabView Fragen und an alle, die diese Arbeit Korrektur gelesen haben.

Bei Matthias Weidemüller bedanke ich mich für die Übernahme der Zweitkorrektur dieser Arbeit.

Nicht zu Letzt danke ich meiner Familie und meinen Freunden für all Ihre Unterstützung in den letzten Jahren.

## Declaration

Erklärung:

Ich versichere, dass ich diese Arbeit selbstständig verfasst habe und keine anderen als die angegebenen Quellen und Hilfsmittel benutzt habe.

Heidelberg, den 10 August 2018

.....